

ELECTRIC DIMENSIONAL TREATMENT OF MATERIALS

High-Speed Anodic Dissolution of Heat-Resistant Chrome–Nickel Alloys Containing Tungsten and Rhenium: II. Nitrate Solutions

A. I. Dikumar^{a, b}, I. A. Ivanenkov^c, B. P. Saushkin^c, S. A. Silkin^b, and S. P. Yushchenko^{a, b}

^a Institute of Applied Physics, Academy of Sciences of Moldova, ul. Akademiei 5, Chisinau, MD-2028 Republic of Moldova

^b Shevchenko Dniester State University, ul. 25 Oktyabrya 128, Tiraspol, 3300 Republic of Moldova

^c MATI-Russian State Technological University, Berezkhovskaya nab. 14, Moscow, 109240 Russia

Received October 26, 2006

Abstract—Anodic dissolution of two heat-resistant chrome–nickel alloys containing 12% (weight) tungsten and 8% tungsten with 6% rhenium in a 2 M NaNO₃ solution was investigated using the rotating disk electrode method at current densities up to 30 A/cm². It is shown that anodic dissolution of these alloys occurs in the transpassive region of potentials with transition of the components in solution to forms with the highest oxidation level. Various mechanisms of alloy dissolution determining the processing speed (together with electrochemical dissolution) are proposed, including disintegration of the hardening phase, chemical oxidation of low-valence intermediates by solution components, and electrochemical formation of surface oxide layers. The results of change in the chemical composition of surfaces depending on the processing regimes are presented. Some variants of control by regimes of electrochemical dimensional processing (ECDP) of details from these alloys to achieve the optimal parameters of ECDP are proposed.

DOI: 10.3103/S1068375507030015

INTRODUCTION

In [1], the results of high-speed anodic dissolution of heat-resistant chrome–nickel alloys containing tungsten and rhenium in chloride solutions are described. For processing of the above materials, electrochemical dimensional processing (ECDP) is widely used and nitrate solutions or their mixtures with chlorides are used as electrolytes [2–4].

Use of nitrate solutions may be expedient for a number of reasons. First, the cathode process in the conditions of ECDP in nitrates may proceed without gas release or with its considerable decrease since, in nitrates, the cathode reaction of gaseous hydrogen release may be replaced by the reaction of reconstruction of nitrate ions up to products that do not produce a gas phase, which is fundamentally important in the case of use of small interelectrode gaps and, therefore, for increasing the process localization [2–4]. Second, for a number of metals and alloys in nitrate solutions, an increasing dependence of current yield on current density is typical, which is also important for increasing process localization in the conditions of ECDP [2–4]. Moreover, on dissolution of heat-resistant chrome–nickel alloys containing the hardening γ phase in nitrate and chloride electrolytes, its decomposition is possible, which decreases the power intensity of an electrochemical treatment process [5].

A distinguishing feature of anodic dissolution of metals of the iron subgroup (including nickel) in nitrate

solutions is the destruction of surface oxides at high current densities and, as a result, transition from the reaction of oxygen release to the reaction of anodic dissolution on an increase in current density [2, 3]. A consequence of this effect is the increasing dependence of current yield on current density, which provides the conditions for increasing localization of the process of ECDP of these metals [2–4].

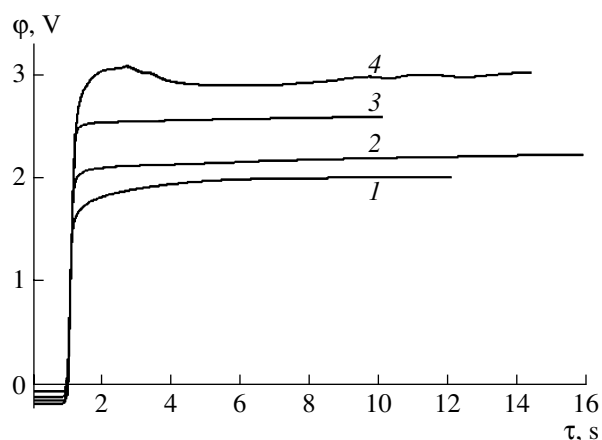


Fig. 1. Typical dependences of the dissolution potential on time for alloys I (1–3) and ZhS-6U (4) in 2 M NaNO₃ at current densities (A/cm²) 1.0 (1), 3.0 (2), 5.0 (3), and 10.0 (4) and RDE speeds (rpm) of 260 (1, 3) and 1260 (2, 4).

Table 1. Composition of surface layer after anodic dissolution of alloys at $i = 2 \text{ A/cm}^2$ in 2 M NaNO_3 (wt %)

Place in Fig. 3		Ni	Cr	W	Re	Co	Ti	Al	C	Si	O
	Alloy ZhS-6U										
	Initial composition	56.5 ± 0.8	9.1 ± 0.7	12.1 ± 2.0	–	9.5 ± 0.4	2.6 ± 0.5	5.5 ± 0.1	4.5 ± 0.6	–	–
(e)	Basic phase	53.1	8.7	14.2	–	9.1	1.8	4.4	4.5	–	3.5
(d)	Boundary phase	49.2	6.6	6.7	–	6.1	2.8	3.2	21.0	–	4.3
(f)	Phase enriched with Ni (γ')	66.0	3.3	5.5	–	6.9	4.8	6.4	4.4	–	2.8
Alloy I											
	Initial composition	62.1 ± 0.1	4.8 ± 0.1	7.8 ± 0.5	5.6 ± 0.7	10.1 ± 0.4	–	5.0 ± 0.3	3.7 ± 0.2	0.9 ± 0.1	–
(a)	Basic phase	59.4	4.5	9.3	5.2	9.0	–	5.8	3.5	1.0	2.2
(c)	Boundary phase	62.9	2.4	9.7	–	7.3	–	7.8	5.9	–	4.0
(b)	Oxidized phase	42.6	3.2	22.4	2.7	4.8	–	4.2	4.4	1.6	14.3

Table 2. Composition of surface layer after anodic dissolution of alloy I at $i = 5 \text{ A/cm}^2$ in 2 M NaNO_3 (wt %)

Place in Fig. 5		Ni	Cr	W	Re	Co	Al	C	Si	O
		Initial composition	62.1 ± 0.1	4.8 ± 0.1	7.8 ± 0.5	5.6 ± 0.7	10.1 ± 0.4	5.0 ± 0.3	3.7 ± 0.2	0.9 ± 0.1
(b)	Basic phase	68.8 ± 1.5	4.4 ± 0.5	9.8 ± 1	–	10.1 ± 0.6	7.0 ± 0.6	–	–	–
(a)	Oxidized phase	59.2 ± 5.7	2.4 ± 0.3	10.4 ± 2.0	–	7.2 ± 0.7	7.0 ± 1.3	6.2	1.7	6.3 ± 3.0
	Average	64	3.4	10.1	–	8.7	7.0	3.1	0.9	3.2

Table 3. Composition of surface layer after anodic dissolution of alloys I ($i = 29 \text{ A/cm}^2$) and ZhS-6U ($i = 24 \text{ A/cm}^2$) in 2 M NaNO_3 (wt %)

Place in Fig. 6		Ni	Cr	W	Re	Co	Al	Ti	O	Others
	Alloy I									
(c)	Basic phase	33.5 ± 8.0	7.9 ± 0.8	26.9 ± 7.0	4.6 ± 0.7	6.6 ± 1.3	2.1 ± 0.9	–	16.3 ± 1.1	~2.8
(d)	Oxidized phase	4.0 ± 0.4	5.3 ± 0.4	50.4 ± 3.8	~2.0	–	–	–	30.3 ± 1.9	~7.0
ZhS-6U										
(a)	Basic phase	55.1 ± 5.0	5.1 ± 0.9	11.7 ± 4.5	–	6.9 ± 0.5	5.6 ± 0.4	4.7 ± 1.7	9.2 ± 0.2	–
(b)	Oxidized phase	39.0	3.2	27.7	–	3.8	3.1	6.1	17.2	–

In the case of high-speed anodic dissolution of chrome–nickel alloys in nitrates, a similar effect is not observed [2–5]. Electrochemical dissolution of alloys of nickel with tungsten in nitrates depends to a greater extent on the concentration of tungsten in an alloy, and,

at a high concentration (i.e., with the formation of a solid solution of tungsten in nickel, ~20–30% W), the alloy behaves similarly to chrome–nickel alloys, i.e., it is dissolved with high speed, while, at low concentrations of tungsten, its electrochemical characteristics are

close to the electrochemical properties of pure nickel [6]. High-speed dissolution of chrome-nickel alloys with rhenium, as well as with tungsten in which tungsten is partly replaced by rhenium, in nitrate electrolytes was not investigated earlier. It is known, however, that, in contrast to tungsten, rhenium at high current densities is dissolved in nitrates with high speed, while for tungsten a deep passivity is typical due to the formation of insoluble oxide WO_3 [2, 3, 7]. Anodic dissolution of rhenium in nitrates at high current densities takes place with the formation of the ion ReO_4^- [7].

The main task of the present work (as in [1] with reference to the dissolution of these alloys in chlorides) was the investigation of the mechanism of formation of surface covering layers on anodic dissolution of the above-mentioned alloys in nitrate electrolytes in a wide area of current densities and their role in the achievement of specific values of material removal speeds during ECDP, as well as the influence of macroscopic inhomogeneity of alloys in the formation of composition and surface properties.

EXPERIMENTAL

Anodic dissolution of two chrome-nickel alloys is investigated, the composition of which is presented in Table 1. The method of investigation completely corresponded to the method described in [1], with the only difference that the maximum current densities achieved in the present paper were less than those described in [1] ($\sim 30 \text{ A/cm}^2$) and the dissolution occurred in 2 M NaNO_3 .

RESULTS AND DISCUSSION

Results of polarization measurements. It is seen from the results of galvanostatic polarization measurements presented in Figs. 1 and 2 that (i) dissolution at relatively low current densities takes place at potentials substantially exceeding the potentials of dissolution of the investigated alloys in chlorides, i.e., at potentials of so-called transpassive dissolution; (ii) hydrodynamics does not influence the dissolution speed up to the highest measured current densities; (iii) in the vicinity of the measurement error, the current density dependence on the potential follows the Tafel dependence with an incline of $\sim 100 \text{ mV/order}$ for alloy I (with rhenium) taking into account the correction of the ohmic voltage drop between the capillary end and the surface of dissolution performed by the method described in [8, p. 54]; and (iv) the Tafel incline for the alloy ZhS-6U, containing more tungsten, is higher, which is indirect evidence of the fact that partly a charge is lost on oxidation of a surface and for the alloy ZhS-6U this contribution is larger.

The data of EDX analysis (Table 1) demonstrate that, even in the conditions of dissolution at relatively low current densities (2 A/cm^2), the oxidation of a surface for both materials is observed. It should be stressed

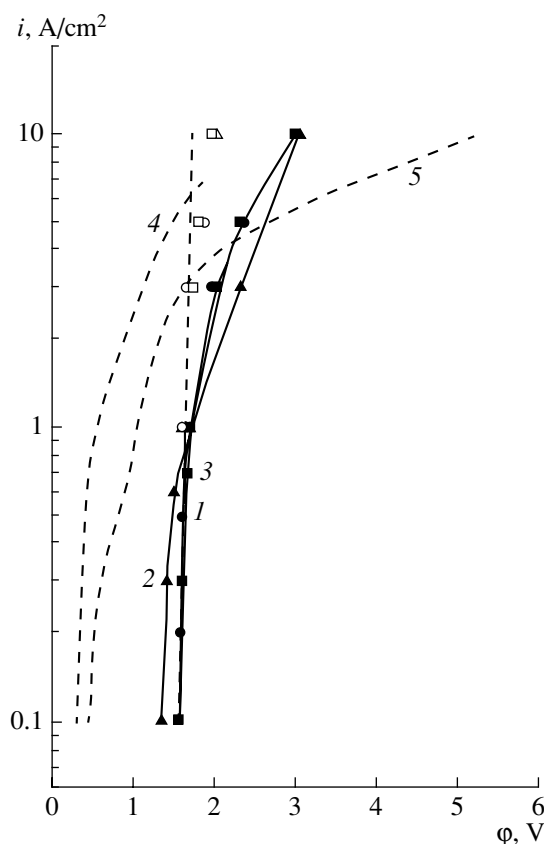


Fig. 2. Galvanostatic polarization curves in 2 M NaNO_3 for alloys I (1, 3) and ZhS-6U (2) at RDE speeds (rpm) of 260 (1) and 1260 (2, 3). The dotted curves correspond to the polarization curves for alloys I (4) and ZhS-6U (5) on processing of these alloys in 2 M NaCl [1]. The white symbols correspond to the potential values corrected taking into account the ohmic component.

that, due to macroscopic inhomogeneity of alloys, the oxidizability of a surface was different in different areas, as evidenced by the results of local EDX analysis (Fig. 3). The analyzed areas, corresponding to basic, oxide (oxygen-enriched), and boundary (nickel-enriched) phases, are shown by crosses in Fig. 3 (see also Table 1; here, the results of EDX analysis correspond to the points on the respective microphotographs in Fig. 3).

Influence of current density and composition of alloys on specific dissolution rate. Despite the fact that, in a nitrate electrolyte, dissolution takes place at potentials $\sim 1 \text{ V}$ more than in chloride, the specific dissolution rate ϵC (ϵ is the current yield, and C is the electrochemical equivalent) at $i < i_{cr}$ (i_{cr} is the critical current density, the nature of which will be discussed below) is higher than in a chloride solution for both investigated alloys (Fig. 4).

At $i > i_{cr}$ (also for the two alloys), the specific dissolution rate decreases with the current density, which is also typical for dissolution in chlorides. In [1], it was

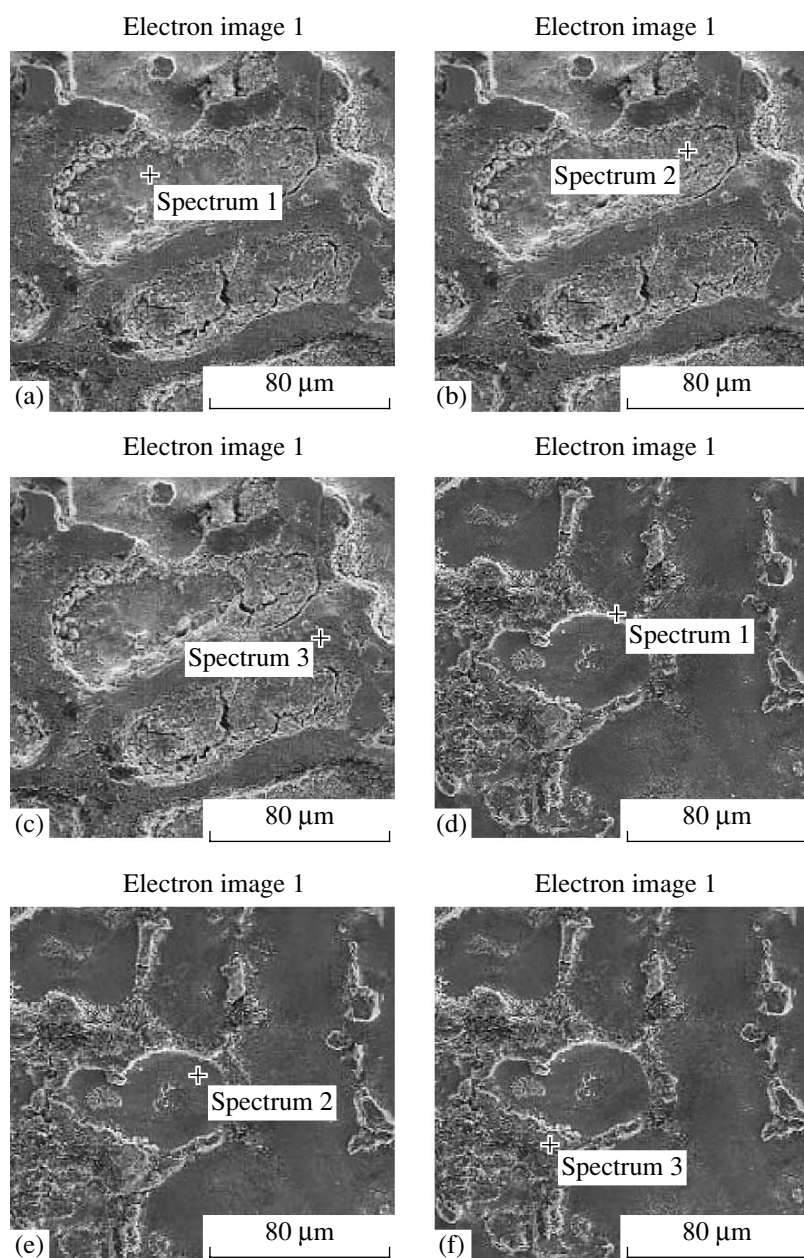


Fig. 3. SEM microimages of the surfaces of alloys I (a–c) and ZhS-6U (d–f) obtained after anodic dissolution (0.023 A h) in 2 M NaNO_3 at an RDE speed of 1260 rpm and a current density of 2 A/cm^2 .

shown that the reason for the effect observed is connected with intensive oxidation of a surface.

It seems obvious that the higher specific dissolution rate at $i < i_{cr}$ is connected with decomposition of the γ' phase in nitrate solutions, a fact that is quite well known for ECDP in these solutions [2–5]. And, despite the fact that this cannot be confirmed quantitatively in the given specific case since the concentration of the γ' phase in alloys was not determined, there is no reason to exclude such a mechanism of material removal during the processing of the investigated alloys.

The value $i = i_{cr}$ was estimated in a similar manner as in [1], but only with reference to nitrate solutions on the basis of the data of [9] (see also [8, pp. 86–90]). The estimation carried out showed that the attainment of the saturation concentration for dissolution products of a basic component—nickel in a nitrate solution—is observed at a concentration of 2 M and a rotation velocity of 1260 rpm for alloy I at a current density of $\sim 4 \text{ A}/\text{cm}^2$ (Fig. 4).

Comparison of the experimentally observed values of ϵC in the area close to i_{cr} (a similar value for the alloy ZhS-6U is observed at $i \approx 15 \text{ A}/\text{cm}^2$ (Fig. 4)) with the

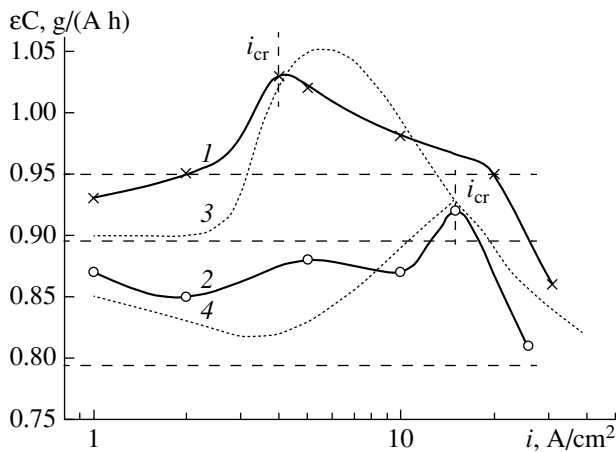


Fig. 4. Dependence of the specific dissolution rate of alloys I (1) and ZhS-6U (2) in 2 M NaNO₃ on the current density at a rotation speed of 1260 rpm. The dotted lines correspond to the analogous dependences for alloys I (3) and ZhS-6U (4) obtained on processing in 2 M NaCl.

values calculated taking into account only electrochemical dissolution (0.95 and 0.89 g/(A h) for alloy I and 0.89 and 0.79 g/(A h) for the alloy ZhS-6U under the assumption of dissolution of chrome of the type of Cr(III) and Cr(VI) accordingly, which is represented by horizontal dashed lines in Fig. 4) shows that, in the area of $i \approx i_{cr}$ in both cases, the dissolution speed is exceeded in accordance with the Faraday area.

Change in the composition of surface layers in the treatment process. It is seen from the results presented in Table 1 that, already at relatively low current densities, the oxidation of the surface layer takes place, while the presence of macroscopic inhomogeneity (a multiphase state) of an alloy leads to inhomogeneity of the dissolution speed distribution (Fig. 3). However, in the conditions of etching at $i \approx i_{cr}$ the dissolution speed of

different phases of an alloy is equalized, which follows both from data of scanning electron microscopy (SEM) (Fig. 5) and from the results of the surface analysis presented in Table 2 for alloy I. This is caused by the circumstance, following from the above evaluating calculations of the value of i_{cr} for the used speed of rotation of a disk electrode (RDE), that in these conditions the dissolution takes place through the salt surface film of the products of dissolution of alloy components, the existence of which provides for equalization of dissolution speeds of different phase components. However, the equalization effect is achieved due to the fact that part of the surface is dissolved in the regime of polishing (the area “spectrum 2” in Fig. 5b), which is presented in Table 2 as the “basic phase,” but a porous oxidized surface layer (the area “spectrum 1” in Fig. 5a, the “oxide phase” in Table 2) is formed on the other part of the surface. Actually, the dissolution at $i \approx i_{cr}$ takes place in the regime of an anodic limiting current caused by salt passivation, which as a rule leads to the polishing of a surface. Comparison of the results presented in Tables 1 and 2 shows that, even if insignificant oxidation of a surface takes place, it does not exceed the oxidation observed at lower current densities.

The value of i_{cr} is determined by the hydrodynamic conditions and should be displaced into the area of higher current densities with an increase in the speed of electrolyte flow.

At $i > i_{cr}$ significant oxidation of a surface is observed (Fig. 6, Table 3). It should be noted that, for alloy I, it is noticeably greater than for the alloy ZhS-6U. Special analysis of surface oxide formations (Fig. 6b; Table 3, the “oxide phase” of alloy I) shows that it is a practically pure oxide of tungsten WO₃ contaminated by oxides of nickel and some alloying components. From the results of analysis of the surface formations (Fig. 6b, analysis point “spectrum 2”), it follows that they contain ~75 at % oxygen, which corresponds to the oxide

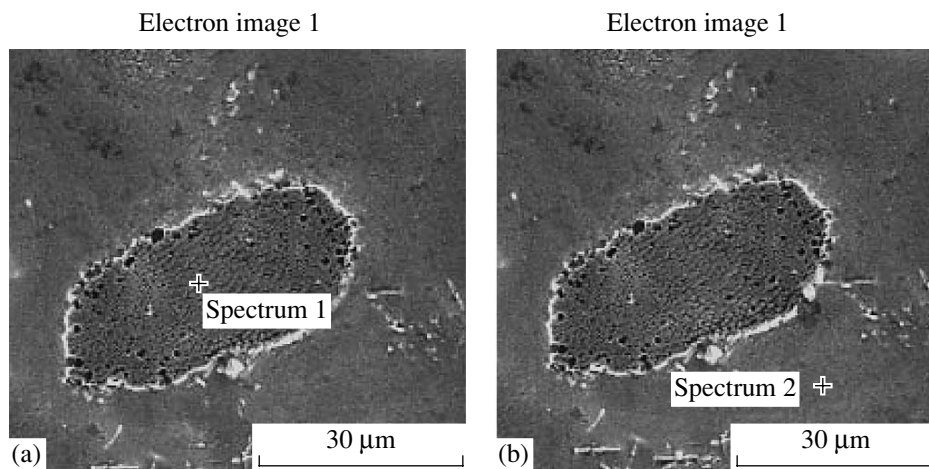


Fig. 5. SEM microimages of the surface of alloy I after processing in 2 M NaNO₃ (0.023 A h) at a current density of 5 A/cm² and a rotation speed of 1260 rpm. Explanations in the text.

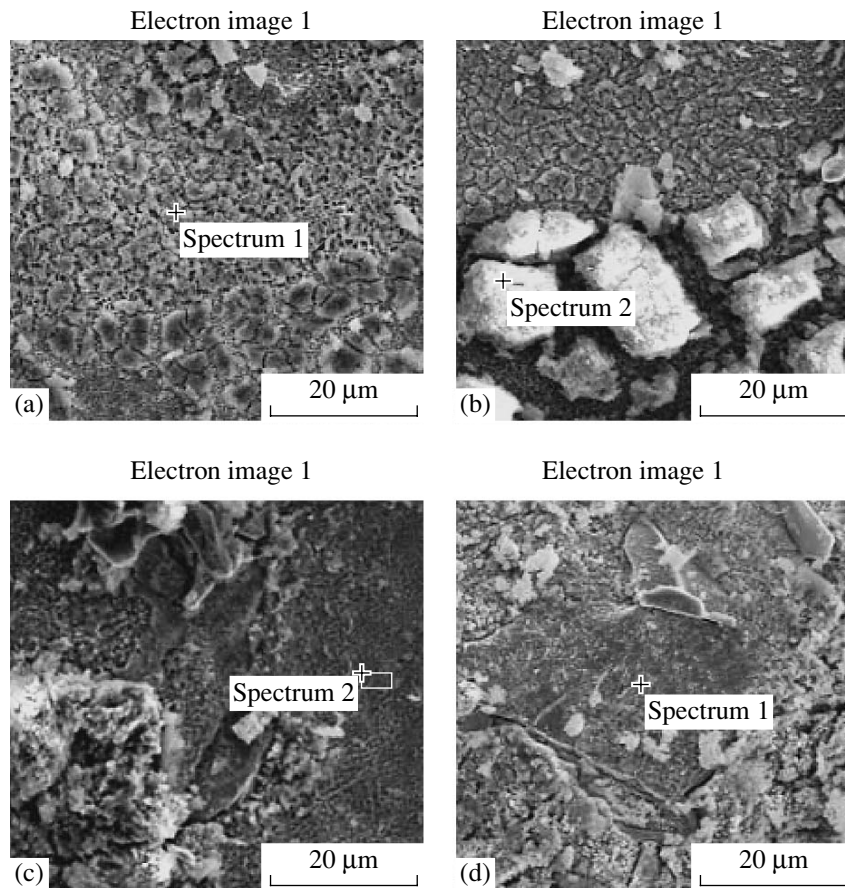


Fig. 6. SEM microimages of the surface of alloys I (a, b) and ZhS-6U (c, d) after processing in 2 M NaNO₃ (0.023 A h) at current densities (A/cm²) of 29 (a, b) and 24 (c, d).

WO₃. But the basic surface is also very oxidized (~50 at % oxygen, Fig. 5a).

An analogous picture is observed for the alloy ZhS-6U, with the only difference that the oxidation of a surface is less than for alloy I. There are at least two reasons for this. The first of them is that the data for this alloy are obtained at lower current densities, and the second follows from the fact that this current density slightly exceeds i_{cr} (i.e., the area of salt passivation) for this alloy (Fig. 4). In this case, a substantially smaller decrease in ϵC caused by the oxidation of a surface layer is observed.

Thus, even despite the fact that there is a significantly higher concentration of a basic passivating alloy element, tungsten, in the ZhS-6U alloys, negligible exceeding of the value of i_{cr} leads to substantially lower oxidation of the surface at the current density of electrochemical treatment used.

An important conclusion for the practice of ECDP follows from the presented results, implying that the electrical and hydrodynamic regimes of treatment are interrelated (for a given composition and concentration of electrolyte) and, evidently, the conditions corresponding to treatment at current densities close to i_{cr}

should be optimal. They provide for not only the maximum specific dissolution rate, but also a better surface quality, while the surface composition after the treatment practically does not differ from the initial composition (Table 2).

The data shown in the diagram in Fig. 7 in the form of the relation $K_s = \frac{C_s}{C_m}$ (C_s is the mean concentration of elements in a surface layer after treatment, and C_m is the mean concentration in the alloy before treatment) show how noticeably the concentration of alloying components may change, especially at high current densities. This is a consequence of the process of its oxidation at $i > i_{cr}$.

Processing rate. Role of different electrochemical and nonelectrochemical mechanisms determining it. The analysis conducted shows that, in the conditions of electrochemical processing at high current densities in nitrate electrolytes, there can be not one (electrochemical) but several mechanisms determining its speed.

1. Electrochemical dissolution of the components of the alloy, which is inhomogeneous due to the difference in the dissolution speeds of different components.

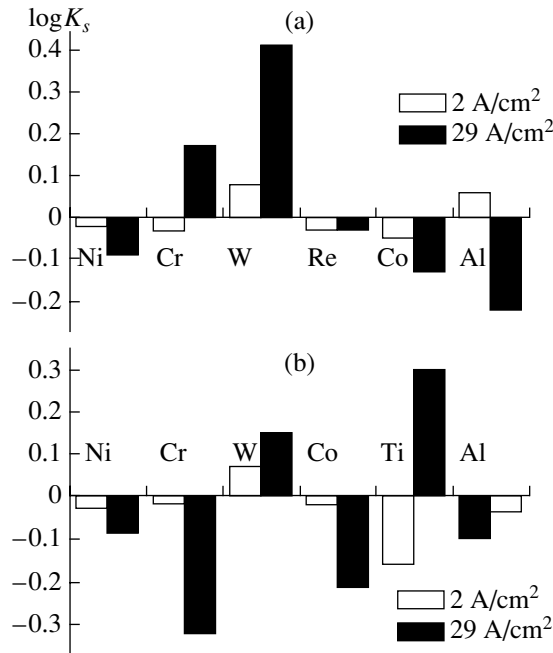


Fig. 7. Diagram of the change in concentration of components of alloys I (a) and ZhS-6U (b) in the surface layer after processing in 2 M NaNO₃ at different current densities.

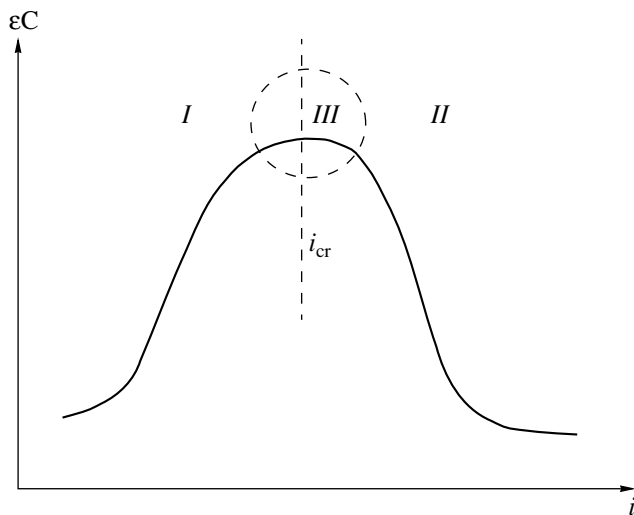


Fig. 8. Schematic dependence of specific dissolution rate (current yield) on current density on processing in a nitrate solution. Explanations in the text.

2. Partial decomposition of phases (most probable is the decomposition of the hardening γ' phase).

3. Chemical oxidation of intermediate low-valence particles (ILVPs) by an oxidant (or components of the electrolyte, which may play the role of oxidants), leading, as in the case of dissolution in chlorides (see [1]),

to an anomalously high dissolution rate in the conditions of salt passivation (Fig. 4).

4. Surface oxidation. It is observed to a greater extent the greater the current density of dissolution in comparison to the value of i_{cr} due to the achievement of salt passivation.

The critical current densities are determined by the hydrodynamic conditions of treatment, and the higher the intensity of an electrolyte flow (hydrodynamic depassivation), the higher the optimal current density of treatment can be.

CONCLUSIONS

Investigation of the electrochemical peculiarities of the high-speed anodic dissolution of heat-resistant chrome-nickel alloys containing tungsten and rhenium in a nitrate solution showed that the ionization of alloy components takes place in the transpassive area of potentials with the formation of dissolution products of the highest oxidation level. However, together with electrochemical dissolution, a whole series of other mechanisms determining the total speed of the process takes place: chemical oxidation of ILVPs, partial decomposition of the hardening γ' phase, and formation of insoluble oxides.

The maximum treatment speed is achieved in the area of formation of a salt film from the dissolution products (Fig. 8, area III). It is obvious that this area of current densities is optimal for ECDP of the investigated alloys in nitrates since (1) an increasing dependence of current yield on current density in area I is observed (Fig. 8), which increases the localizing capability of the electrolyte (see, for example, [8, 10]); (2) the composition of resulting surface layer is close to the initial composition; (3) the transition to area III is accompanied by a substantial change in the composition of the surface layer in comparison to the initial composition due to the oxidation of the surface.

An increase in current density and, therefore, treatment speed with optimal ECDP conditions being maintained should be achieved by intensification of the hydrodynamic regimes of electrochemical processing.

ACKNOWLEDGMENTS

The authors are grateful to E. Monaiko of the Center for Investigation and Testing of Materials of the Technical University of Moldova for conducting surface analysis.

REFERENCES

1. Dikusar, A.I., Ivanenkov, I.A., Saushkin, B.P., Silkin, S.A., and Yushchenko, S.P., High-Speed Anodic Dissolution of Heat-Resistant Chrome-Nickel Alloys Containing Tungsten and Rhenium: I. Chloride Solutions, *Electronic Treat. Mater.*, 2007, no. 1, pp. 4–15.

2. Dikusar, A.I., Engel'gardt, G.R., Petrenko, V.I., and Petrov, Yu.N., *Elektrodnye protsessy i protsessy pelenosa pri elektrokhimicheskoi razmernoj obrabotke metallov* (Electrode Processes and Transport Processes in Electrochemical Dimensional Processing of Metals), Chisinau: Shtiintsa, 1983.
3. Davydov, A.D. and Kozak, E., *Vysokoskorostnoe elektrokhimicheskoe formoobrazovanie* (High-Speed Electrochemical Shaping), Moscow: Nauka, 1990.
4. Eliseev, Yu.S., Krylov, V.V., Mitrofanov, A.A., Saushkin, B.P., Sychkov, G.A., and Troshin, A.N., *Fiziko-khimicheskie metody obrabotki v proizvodstve gazoturbinnnykh dvigatelei* (Physicochemical Methods of Treatment in Production of Gas Turbine Engines), Saushkin, B.P., Ed., Moscow: Drofa, 2002.
5. Petrenko, V.I., Dikusar, A.I., and Arzhintar', O.A., Influence of the Concentration of Hardening γ' Phase in Heat-Resistant Chrome–Nickel Alloys on the Speed of Their Electrochemical Processing in Solutions of Nitrates and Chromates, *Elektronnaya Obrab. Mater.*, 1976, no. 4, pp. 14–19.
6. Davydov, A.D., Kiriyak, E.N., Ryabova, A.N., Kashcheev, V.D., and Kabanov, B.N., Influence of Tungsten on High-Speed Anodic Dissolution of Alloys with a Nickel Base, *Elektronnaya Obrab. Mater.*, 1979, no. 5, pp. 19–24.
7. Dikusar, A.I., Michukova, N.Yu., Parshutin, V.V., and Petrov, Yu.N., Peculiarities of Anodic Dissolution of Rhenium in Neutral and Alkaline Solutions at High Current Densities, *Dokl. Akad. Nauk SSSR*, 1977, vol. 233, no. 5, pp. 900–902.
8. Dikusar, A.I., Engel'gardt, G.R., and Molin, A.N., *Termokineticheskie yavleniya pri vysokoskorostnykh elektrodnykh protsessakh* (Thermokinetic Phenomena in High-Speed Electrode Processes), Chisinau: Shtiintsa, 1989.
9. Dikusar, A.I., Engel'gardt, G.R., Molin, A.N., Davydov, A.D., and Vysokova, E.A., Mass Transfer in Intensive Anodic Dissolution of Nickel in a Nitrate Solution, *Elektronnaya Obrab. Mater.*, 1987, no. 1, pp. 53–58.
10. Petrenko, V.I. and Dikusar, A.I., *Faktory, opredelyayushchie rasseivayushchuyu sposobnost' elektrolitov pri elektrokhimicheskoi razmernoj obrabotke metallov* (Factors Determining Scattering Power of Electrolytes in Electrochemical Dimensional Processing of Metals), *Theory and Practice of Electrochemical Processing of Metals*, Chisinau: Shtiintsa, 1976, pp. 43–64.

ELECTRIC DIMENSIONAL TREATMENT OF MATERIALS

Corrosion Inhibition of Steels by Calcii Borogluconas in Electrolytes for Electrochemical Dimensional Processing

V. V. Parshutin and N. S. Sholtoyan

Institute of Applied Physics, Academy of Sciences of Moldova, ul. Akademiei 5, Chisinau, 2028 Republic of Moldova

Received December 7, 2006

Abstract—A new electrolyte has been developed to ensure corrosion resistance of steel workpieces that have been treated, and of the equipment employed in the process of electrochemical shaping and while in storage when not in use, as well as to improve working conditions. For this purpose, the additive calcii borogluconas is introduced into an electrolyte containing sodium chloride or sodium nitrate. As a result, full protection of operating equipment and manufactured pieces is achieved during electrochemical processing without loss of productivity, as well as during long storage of parts without additional washing or anticorrosive treatment.

DOI: 10.3103/S1068375507030027

INTRODUCTION

There are few papers on the heightening of corrosion resistance of materials and equipment during electrochemical shaping that uses aggressive solutions of sodium chloride or sodium nitrate as an electrolyte [1–5]. In a number of cases, potassium iodide or Rochelle salt serves as an inhibitory component of electrolyte [1]. A combined additive of 100 g/l NaNO₂ and 1 g/l sodium benzoate decreases the corrosion rate of low-carbon steel in a water solution of sodium chloride by approximately 80 times [2]. However, the concentration of the environmentally dangerous component NaNO₂ is very high. Addition of KNO₂ and NaNO₂ in 10% solution of sodium chloride decreases the corrosion rate of carbon and austenitic steels in electrochemical dimensional processing (ECDP), while NaOH, which decreases corrosion, substantially deteriorates the quality rating in ECDP of these steels [3]. Sodium gluconate or potassium gluconate, or oxalic acid or sodium oxalate hinder the formation of insoluble residue of Fe(OH)₃ on a treatment surface or an instrument during ECDP in NaCl, thus decreasing the possibility of local corrosion [4].

The electrolyte containing sodium nitrate, sodium nitrite, and kerosene is also known [5]. Its disadvantages

are a comparatively small increase in corrosion resistance of the metal of treated components and equipment at increased power inputs due to the introduction of kerosene into the electrolyte, as well as the presence of a great deal of toxic NaNO₂. Moreover, the presence of kerosene in an electrolyte and release of hydrogen in the treatment process create dangerous working conditions by an explosive gas mixture in the chambers of electrochemical machines.

For electrochemical marking of noncorrosive steels, the electrolyte on the basis of a water solution of NaNO₂, NaNO₃, triethanolamine, and ferricyanic potassium is used [6]. Its deficiency is the high content of NaNO₂, which complicates the use of equipment and deteriorates working conditions. As well, the electrolyte does not provide for complete protection of a treatment surface or equipment. Moreover, the electrolyte in [5] and the electrolyte in [6] do not permit protection of the treated parts during storage.

Owing to the introduction of a combined additive consisting of sodium nitrite and urotropine into the electrolyte on the basis of NaCl or NaNO₃, as a result of synergistic interaction of inhibitor components, it is possible to completely suppress the corrosion of treated components and equipment (both in the process of

Table 1. Chemical composition of treatment steels

Steel	Content of elements, weight %									
	C	Mn	Si	Cr	Ni	Mo	V	Zr	Nb	Fe
Ст. 10	0.07–0.14	0.35–0.65	0.17–0.37	≤0.15	≤0.25	–	–	–	–	basis
Ст. 45X	0.41–0.49	0.50–0.80	0.17–0.37	0.8–1.1	≤0.30	–	–	–	–	"
30XH2MΦA	0.27–0.34	0.30–0.60	0.17–0.37	0.60–0.90	2.00–2.40	0.20–0.30	0.10–0.18	–	–	"
3X3M3ΦБЦA	0.27–0.34	0.30–0.60	0.17–0.37	~3.0	–	~3.0	~1.0	~1.0	~1.0	"

Table 2. Influence of inhibitors on the area of corrosion (S, %) in a solution of 150 g/l NaCl ($\tau = 120$ h)

Composition of corrosion media, g/l	Steel 30XH2MΦA	Steel 3X3M3ΦБЦА
NaCl 150	88	77
NaNO ₃ 150 + kerosene 15 + NaNO ₂ 10	14	13
NaNO ₃ 10 + NaNO ₂ 50 + three-ethanolamine 6 + ferricyanic potassium 25	6	6
NaCl 150 + calcii borogluconas:		
1	10	8
2	7	6
5	5	3.5
10	1.5	1.0
15	c.a.*	c.a.
20	c.a.	c.a.
30	c.a.	c.a.
40	c.a.	c.a.
50	c.a.	c.a.

* Corrosion is absent.

ECDP and during storage) [7]. The efficiency of anodic treatment slightly decreases. However, the disadvantage of this composition is the presence of very toxic sodium nitrite in it.

The aim of the work is to find an environmentally safe inhibitor that decreases corrosion losses in ECDP and which changes the anodic dissolution rate of steels as little as possible.

METHOD

After preliminary experiments (as in the case of protection of carbon steels in natural water [8, 9]) calcii borogluconas was chosen as an additive in electrolyte. This is an environmentally safe substance, and its solubility in water electrolytes is substantially higher than gluconate calcium. In water of different salt contents, it protects the steel sufficiently well even at small concentrations during both natural and forced convection of a solution. Further, we carried out optimization of the composition of inhibition components.

The investigations were performed according a method close to [7]. Corrosion tests were carried out for total submersion of samples in a solution on equal depth with access to air. Samples of $50 \times 25 \times 3$ mm were fabricated from steels the chemical composition of which is presented in Table 1. The side surface of samples was isolated by lacquer. The initial roughness of a surface corresponded to treatment by polishing. Before the test, the samples were thoroughly degreased by Viennese lime, washed by distilled water, and drained by filter paper. After the tests, they were taken out, drained first in air and then in a desiccator above a layer of calcined CaCl₂. Removal of corrosion products from steel samples were carried out a 0.5 M solution of hydrochloric acid with the addition of 0.5% urotropine. The losses from corrosion were detected by gravimetric analysis. Time of testing was 120 h. The temperature was kept at $20 \pm 0.5^\circ\text{C}$. The effect of inhibitor action was estimated by the criterion of the level of protection determined by the formula $Z = (k - k_1)/k$, where k and k_1 are the corrosion rates of a metal with and without the use of an inhibitor. The level of protection characterizes the fullness of corrosion suppression. To estimate the efficiency of inhibitors we also used the brak-

Table 3. Influence of inhibitors on the corrosion process of steels in solution 150 g/l NaCl ($\tau = 120$ h)*

Composition of corrosion media, g/l	Corrosion rate k , g/(m ² day)	Protection level Z, %	Braking ratio γ
NaCl 150	3.77/3.5	–	–
NaNO ₃ 150 + NaNO ₂ 10 + kerosene 15	1.45/1.2	61.5/66.4	2.6/2.92
NaNO ₃ 10 + NaNO ₂ 50 + three-ethanolamine 6 + ferricyanic potassium 25	0.1/0.08	91.3/92.5	37.7/43.75
NaCl 150 + calcii borogluconas:			
1	0.5/0.45	85.0/86.2	7.54/7.77
2	0.4/0.36	88.1/89.3	9.43/9.72
5	0.15/0.12	91.5/93.0	25.13/29.17
10	0.03/0.01 0/0	98.0/99.0	125.7/350.0
15	0/0	100/100	–
20	0/0	100/100	–
30	0/0	100/100	–
40	0/0	100/100	–
50	0/0	100/100	–

* In the numerator, the values for 30XH2MΦA steel are shown, and in denominator, for 3X3M3ΦБЦА.

Table 4. Influence of inhibitors on the area of corrosion (S, %) of steels in a solution of 150 g/l NaNO₃ (τ = 120 h)

Composition of corrosion media, g/l	Ст. 10	Ст. 45X
NaNO ₃ 150	100	85
NaNO ₃ 150 + NaNO ₂ 10 + kerosene 15	20	16
NaNO ₃ 10 + NaNO ₂ 50 + three-ethanolamine 6 + ferricyanic potassium 25	18	15
NaCl 150 + calcium borogluconas:		
1	16	15
2	12	10
5	8	6
10	4	3
15	2	0.5
20	Absent	Absent
30	Absent	Absent
40	Absent	Absent
50	Absent	Absent

ing ratio $\gamma = k/k_1$, which shows how many times the corrosion rate decreases from the action of the inhibitor. The estimation of the results of corrosion tests were carried out on the area affected (%).

We determined the energetic parameters of the ECDP process on specially designed table equipment imitating broaching operations as in [7]. A cylindrical electrode instrument with an external diameter of the working end of 10 mm and a hole diameter (for electro-

lyte supply) of 5 mm was used. The interelectrode gap was set equal to 0.2 mm; consumption of electrolyte was up to 10 l/min. The side surface was isolated by lacquer.

RESULTS AND DISCUSSION

The influence of the concentration of electrolyte components, test conditions on the area of affected by corrosion, corrosion rate, braking ratio, level of corrosion protection, and parameters of ECDP are presented in Tables 2–6.

The positive effect of the introduction of calcium borogluconas in electrolyte for electrochemical shaping is seen from the data presented in the tables. Already at a concentration of the addition of 1.0 g/l in the most aggressive electrolyte containing 150 g/l of sodium chloride, the affected area of corrosion for 30XH2MΦA steel decreases from 88 to 10%, and for 3X3M3ΦБЦА steel, from 77 to 8% (Table 2). The braking ratio γ is 7.54 and 7.7, respectively, and the level of protection reaches values of 85 and 86.2%, respectively (Table 3), which is a little lower than when an optimal composition of multicomponent electrolytes is used [5, 6]. A decrease in the concentration of calcium borogluconas below 1.0 g/l is undesirable, since it hardly gives any positive effect, although in tap water, already at an inhibitor concentration of 0.3 g/l, corrosion losses decrease almost five times [8].

Though the electrolyte containing 150 g/l sodium nitrate is less aggressive than the electrolyte on the basis of sodium chloride, the area of low-carbon structural steel Ст. 10 affected corrosion by is 100% at a corrosion rate of 2.6 g/(m² day) (Tables 4 and 5). Doping by chrome (steel 45X) leads to a decrease of in the area

Table 5. Influence of inhibitors on the corrosion process of steels in a solution of 150 g/l NaNO₃ (τ = 120 h)*

Composition of corrosion media, g/l	Corrosion rate k , g/(m ² day)	Protection level Z, %	Braking ratio γ
NaNO ₃ 150	2.6/2.48	–	–
NaNO ₃ 150 + NaNO ₂ 10 + kerosene 15	0.42/0.45	83.8/81.8	6.19/5.51
NaNO ₃ 10 + NaNO ₂ 50 + three-ethanolamine 6 + ferricyanic potassium 25	0.33/0.35	87.3/85.9	7.88/7.09
NaNO ₃ 150 + calcium borogluconas:			
1	0.47/0.43	80.1/79.7	5.53/5.77
2	0.35/0.32	86.2/87.0	7.43/7.75
5	0.20/0.18	90.0/91.2	13.0/13.78
10	0.12/0.10	95.1/96.0	21.67/24.8
15	0.06/0.04	98.2/99.0	43.33/62.0
20	0/0	100/100	–
30	0/0	100/100	–
40	0/0	100/100	–
50	0/0	100/100	–

* In the numerator the values for Ст. 10 are shown, and in the denominator, for the steel 45X.

Table 6. Influence of the conditions of ECDP on the removal rate of steel 45X

Electrolyte composition, g/l	Current density i , A/cm ²	Voltage between electrodes, V	Removal rate, g/min
NaCl 150	30	5.8	0.201
	40	9.3	0.240
	50	14.5	0.342
	60	17.1	0.361
	80	19.2	0.480
NaNO ₃ 150	30	6.4	0.195
	40	10.0	0.231
	50	15.1	0.324
	60	18.0	0.385
	80	20.2	0.462
NaNO ₃ 150 + NaNO ₂ 10 + kerosene 15	30	11.6	0.160
	40	20.4	0.199
	50	29.2	0.250
	60	35.6	0.289
	80	40.0	0.361
NaNO ₃ 10 + NaNO ₂ 50 + three-ethanolamine 6 + ferricyanic potassium 25	30	10.2	0.171
	40	17.1	0.200
	50	20.0	0.268
	60	27.5	0.298
	80	32.0	0.370
NaNO ₃ 150 + calcii borogluconas 30	30	6.8	0.192
	40	10.3	0.221
	50	15.5	0.315
	60	18.4	0.322
	80	20.7	0.450
NaCl 150 + calcii borogluconas 30	30	6.2	0.196
	40	9.7	0.230
	50	14.9	0.338
	60	17.4	0.350
	80	19.8	0.467
NaCl 50	30	6.1	0.201
	40	9.6	0.239
	50	14.65	0.341
	60	17.20	0.362
	80	19.5	0.480
NaCl 50 + calcii borogluconas 1	30	6.15	0.200
	40	9.60	0.237
	50	14.7	0.339
	60	17.2	0.361
	80	19.6	0.478
NaCl 50 + calcii borogluconas 50	30	6.65	0.198
	40	9.8	0.237
	50	14.8	0.339
	60	17.5	0.359
	80	19.8	0.476
NaCl 150 + calcii borogluconas 1	30	5.9	0.199
	40	9.4	0.235
	50	14.65	0.340
	60	17.2	0.356
	80	19.3	0.475

Table 6. (Contd.)

Electrolyte composition, g/l	Current density i , A/cm ²	Voltage between electrodes, V	Removal rate, g/min
NaCl 150 + calcium borotrigluconates 50	30	6.4	0.194
	40	9.8	0.228
	50	15.0	0.335
	60	17.5	0.346
	80	19.9	0.463
NaCl 200	30	5.5	0.200
	40	9.0	0.241
	50	14.1	0.340
	60	16.7	0.361
	80	18.9	0.482
NaCl 200 + calcium borotrigluconates 1	30	5.6	0.195
	40	9.1	0.236
	50	14.2	0.336
	60	16.9	0.357
	80	19.1	0.473
NaNO ₃ 50	30	6.85	0.194
	40	10.3	0.232
	50	15.4	0.320
	60	18.3	0.336
	80	20.5	0.460
NaNO ₃ 50 + calcium borotrigluconates 1	30	6.95	0.193
	40	10.4	0.230
	50	15.5	0.317
	60	18.45	0.331
	80	20.6	0.458
NaNO ₃ 50 + calcium borotrigluconates 50	30	7.3	0.189
	40	10.6	0.226
	50	15.7	0.312
	60	18.6	0.324
	80	20.8	0.451
NaNO ₃ 150	30	6.45	0.195
	40	10.1	0.230
	50	15.2	0.323
	60	18.1	0.333
	80	20.3	0.460
NaNO ₃ 150 + calcium borotrigluconates 50	30	6.85	0.190
	40	10.4	0.219
	50	15.6	0.313
	60	18.5	0.320
	80	20.8	0.447
NaNO ₃ 300	30	5.8	0.192
	40	9.1	0.230
	50	14.1	0.320
	60	16.8	0.332
	80	19.1	0.460
NaNO ₃ 300 + calcium borotrigluconates 1	30	5.9	0.191
	50	14.2	0.316
	80	19.2	0.456
NaNO ₃ 300 + calcium borotrigluconates 50	30	6.1	0.187
	50	14.3	0.310
	80	19.4	0.448

of corrosion of up to 85%, and a decrease in the corrosion rate of up to 2.48 g/(m² day). With the addition of the inhibitor up to the concentration of 2–5 g/l in the electrolyte based on sodium chloride, the process of corrosion suppression is strengthened and the area of corrosion of alloyed steels decreases by 3.5–5.0%. The braking ratio is increased to 25–29%, and the level of protection is increased up to 91.5–93.0% (Tables 2 and 3). At a concentration of calcium borogluconates of 10 g/l, the corrosion losses are decreased 126–350 times and the level of protection reaches values of 98–99%. Finally, at a concentration of the additive of 15–50 g/l, the corrosion process on alloyed steels is completely stopped. It is not possible to increase the concentration of an additive above 50 g/l due to its insufficient solubility.

Introduction in electrolyte of only 1.0 g/l calcium borogluconates decreases the area of corrosion of steels to the values quite comparable with the results using multicomponent inhibitors [5, 6]. The corrosion losses decrease almost six times, and the level of protection reaches 80%. With the increase in the concentration of the additive of calcium borogluconates of 2–15 g/l, corrosion losses decrease 43–62 times, and the level of protection of steels increases up to 86–99%. At a concentration 20–50 g/l, the corrosion of steels is completely stopped.

The results of experiments show that the optimal concentration of calcium borogluconates depends both on the nature of anions (Cl⁻ and NO₃⁻) and on the level of alloying of steels used.

The introduction of the inhibitor in electrolytes for electrochemical shaping shifts the stationary potential of steels into the positive region the more, the higher the concentration of the additive. In addition, the potential changes very fast, which most likely indicates adsorption of an organic inhibitor on an active surface, which causes the braking of corrosion process. As with corrosion in tap water [9], the formation of complexes with the participation of an inhibitor and iron ions takes place. In the presence of several hydroxyl groups and variable valency of iron ions, there is the possibility of the formation of different intermediate complexes on the surface of corrodible metals that differ in composition, solubility, and character of the action of metal transfer into a solution. The film formed on the surface protects a metal against corrosion more efficiently and stabilizes the ionization process of a metal at a lower rate. Namely, the observed decrease in the anodic dissolution rate and the increase in energy consumption when the inhibitor is added into electrolyte can be explained by the presence of this film (Table 6).

The process of inhibition by calcium borogluconates is weakened by competitive participation of complexes of

salts dissolved in a medium. Therefore, for ECDP, the amount of the inhibitor should be introduced into the electrolyte in order to receive the same level of suppression of the corrosion process observed in water.

On the basis of investigations, the electrolyte [10] was developed, which ensures complete termination of the corrosion of treated materials and equipment (both in the process of electrochemical shaping and during storage). The efficiency decreases slightly, and the energy consumption increase by 2–7% (Table 6), which is satisfactorily compensated by the safety of parts and equipment.

It should be noted that calcium borogluconates is non-toxic, and its use allows toxic sodium nitrite to be completely removed from the electrolyte for ECDP at the same or even a higher level of protection.

REFERENCES

1. Pogodin-Alekseev, G.I., Gavrilov, V.M., and Danilina, G.A., USSR Inventor's Certificate no. 233820, *Byull. Izobret.*, 1969, no. 3.
2. Sukemitsu Ito and Hideo Yamamoto, Study on Electrolytic Machining Process. XII. Corrosion of Mild Steels in Sodium Chloride Solution, *J. Mech. Lab. Japan*, 1967, vol. 13, no. 1, pp. 15–24.
3. Sukemitsu Ito and Nobue Shikta, Effect of Inhibitors on Machining Characteristics of Sodium Chloride Solution in Electrochemical Machining, *Bull. Jap. Soc. Precis. Eng.*, 1968, vol. 2, no. 4, pp. 311–317.
4. Khideo Yamamoto, et al., Investigation of Corrosion at Electrochemical Dimensional Treatment. III. Behavior of Precipitation Inhibitors in Solutions of Sodium Chloride, *J. Mech. Lab.*, 1970, vol. 24, no. 5, pp. 224–230.
5. Miroshnikova, E.V. and Televnoi A.V., USSR Inventor's Certificate no. 1215902, *Byull. Izobret.*, 1986, no. 9.
6. Kovaleva, A.D. and Kovalev, L.M., USSR Inventor's Certificate no. 933357, *Byull. Izobret.*, 1982, no. 21.
7. Parshutin, V.V., Revenko, V.G., and Sholtoyan, N.S., Suppression of Corrosion of Steels at Electrochemical Dimensional Processing, *Elektron. Obrab. Mater.*, 2006, no. 3, pp. 138–147.
8. Parshutin, V.V., Sholtoyan, N.S., Sidel'nikova, S.P., and Volodina, G.F., Inhibition of Corrosion of Carbon Steel St.3 in Water by Calcium Borogluconates. I. Corrosion in the Conditions of Natural Airing and Forced Convection, *Elektron. Obrab. Mater.*, 1999, no. 5, pp. 42–56.
9. Parshutin, V.V., Sholtoyan, N.S., Sidel'nikova, S.P., and Volodina, G.F., Inhibition of Corrosion of Carbon Steel St.3 in Water by Calcium borogluconates. II. Dynamics of the Composition of Corrosion Medium Change, Anodic Behavior of Steel, *Elektron. Obrab. Mater.*, 1999, no. 6, pp. 40–47.
10. Parshutin, V.V. and Sholtoyan, N.S., Patent of Moldova no. 3122, *Byull. Izobret.*, 2006, no. 8.

**ELECTRICAL SURFACE
TREATMENT METHODS**

Influence of Load Due to Electric Discharge Channel in Water and Hydrodynamic Load on Stressed–Strained State of Joint Weld

G. A. Barbashova and L. A. Kamenskaya

*Institute of Pulse Processes and Technologies, National Academy of Sciences of Ukraine, Oktyabr'skii pr. 43-a,
Nikolaev-18, 54018 Ukraine*

Received November 24, 2006

Abstract—The load on the surface of a joint weld in electric discharge under water is determined by numerical methods, and the deflected mode of the joint weld under the impact of this load is studied. It is found that the load produced by the electric discharge channel influences the change in the joint weld deflected mode much more strongly than the hydrodynamic load.

DOI: 10.3103/S1068375507030039

INTRODUCTION

In some discharge pulse technologies, the electric discharge is performed directly on the object of treatment [1]—for example, for removal of residual stresses in joint welds [2]. In these cases, between the object under treatment and the electrode, there appears a cavity filled with plasma, i.e., the discharge channel. The pressure in the cavity significantly exceeds the pressure in the surrounding liquid. Hence, the discharge channel broadens intensely, generating compression waves in the liquid. Therefore, the object being treated is affected by both the load due to the discharge channel and the hydrodynamic load. In the present work, the effect of these loads on stressed–strained state of a joint weld is estimated.

Numerical methods were used in the investigation. First, the hydrodynamic problem of a plasma-filled cavity expanding in a liquid half-space restricted by an absolutely rigid surface was solved. The pressure on the surface obtained by its solution was used as a boundary condition for the solution of the problem of dynamic strain of a joint weld.

HYDRODYNAMICS OF UNDERWATER SPARK DISCHARGE

In solving the hydrodynamic part of the problem, we assume that the joint weld is an absolutely rigid unrestricted flat surface. At the initial moment of time, the discharge channel has the form of a straight circular cylinder, its height is equal to the distance between the electrode and the surface, and its radius is determined by the formulas of [3]. The discharge channel is filled with an ideal low-temperature plasma. The liquid surrounding it is an ideal compressible one.

The mathematical statement of the problem and its solution are given in [4].

DYNAMIC STRAIN OF JOINT WELD UNDER PULSE LOAD

The object of investigation is a joint weld of two rectangular plates having a length of 300 mm, width of 100 mm, and thickness of 6 mm each, being butt-welded with their long sides. The obtained welded sample material is steel St3 with a flow limit of 220 MPa. The initial characteristics of the stressed–strained state of the sample under study were determined according to the recommendations of [5, 6].

It was assumed that, before treatment, the object of study was at rest and it freely rested on the surface of a plate of the same material. From its opposite side, perpendicular to the joint weld surface, an electric discharge was produced creating a load on this surface. The other surfaces of the sample were considered load-free.

The dynamic processes are described by the equations of motion of a continuous medium [7]

$$\rho \dot{u}_x = \frac{\partial \sigma_{xx}}{\partial x} + \frac{\partial \sigma_{xy}}{\partial y} + \frac{\partial \sigma_{xz}}{\partial z},$$

$$\rho \dot{u}_y = \frac{\partial \sigma_{xy}}{\partial x} + \frac{\partial \sigma_{yy}}{\partial y} + \frac{\partial \sigma_{yz}}{\partial z},$$

$$\rho \dot{u}_z = \frac{\partial \sigma_{xz}}{\partial x} + \frac{\partial \sigma_{yz}}{\partial y} + \frac{\partial \sigma_{zz}}{\partial z},$$

where u_x , u_y , and u_z are the components of the velocity vector, and σ_{ij} are the components of the stress tensor ($i, j = x, y, z$), $\sigma_{ij} = \sigma_{ji}$.

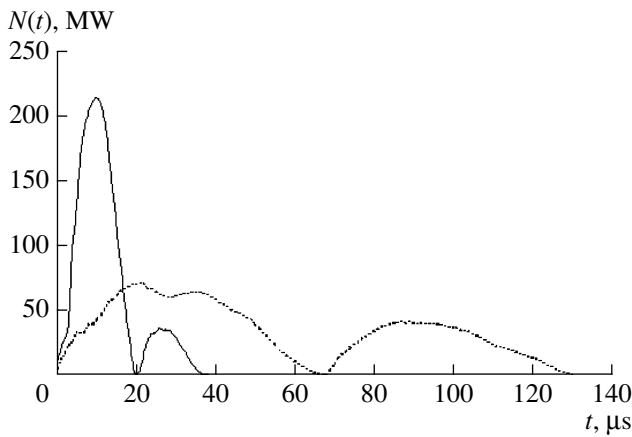


Fig. 1. Electric power supplied into the discharge channel.

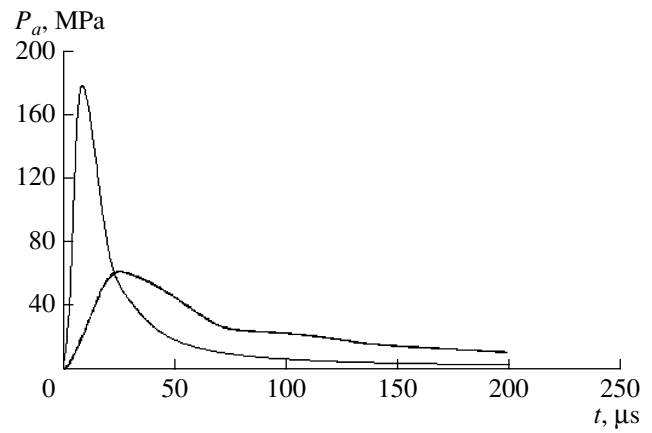


Fig. 2. Pressure in the discharge channel.

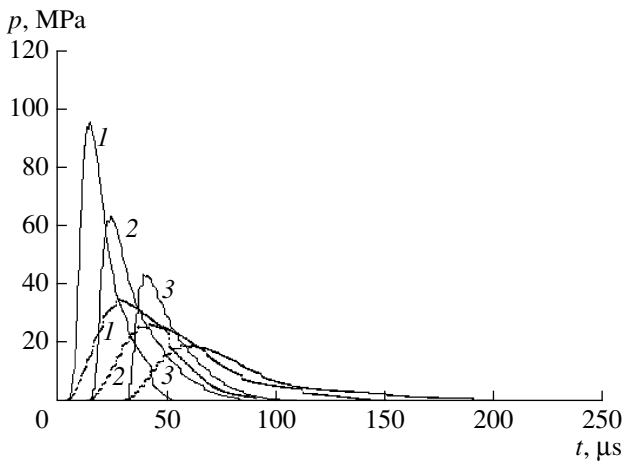


Fig. 3. Liquid pressure on the plate surface at a distance of 0.01 m (curves 1), 0.025 m (curves 2), and 0.05 m (curves 3) from the discharge channel symmetry axis.

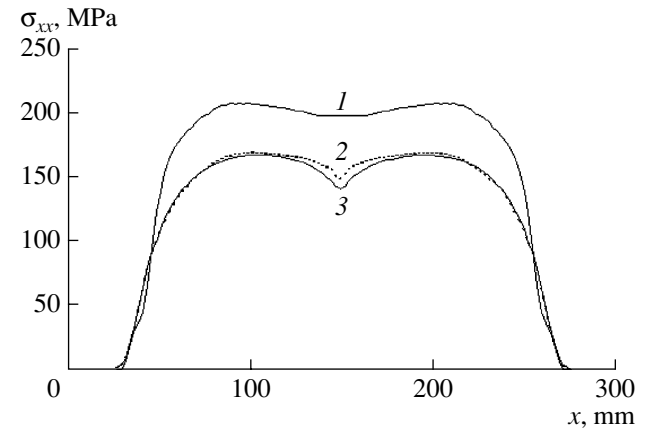


Fig. 4. Distribution of normal stresses along the joint weld (mode I).

The relation between strains and stresses is determined by the generalized Hooke's law [7]

$$\dot{S}_{ij} = 2G(\dot{\epsilon}_{ij} - 1/3\dot{\epsilon}\delta_{ij}); \quad \sigma_{ij} = S_{ij} - \sigma\delta_{ij},$$

and the relation between the mean stress σ and volume strain ϵ was found by the differential ratio $\dot{\sigma} = -K\dot{\epsilon}$ [7].

Here, S_{ij} is the stress deviator, G is the shear modulus, ϵ_{ij} are the strain tensor components, δ_{ij} is the Kroneker symbol, and K is the bulk modulus. Dots above the symbols denote the time differentiation operation.

On the boundary between the welded sample and the plate, the conditions on the free surface ($\sigma_{zz} = 0$) when the contact is absent or the condition of pulse preservation when it is present was given. On the sample surface under load, the corresponding normal stresses are equal to the pressure, and its distribution over the surface during the entire time of observation is taken from the hydrodynamic problem solution. On the

load-free surfaces, the corresponding normal stresses are equal to zero.

The characteristics of the initial stressed-strained state of the joint weld were considered initial conditions.

For solution of the given system of equations, the method of final volumes was applied [8].

Calculations were carried up to equilibrium in the sample.

EXAMPLE OF PROBLEM SOLUTION

Let us give results of numerical study of the stressed-strained state of the joint weld under two modes of its loading.

Figure 1 shows the electric power supplied into the discharge channel. Figures 2 and 3 show, respectively, time dependences of pressure in the discharge channel and liquid pressure on the rigid surface at a distance r

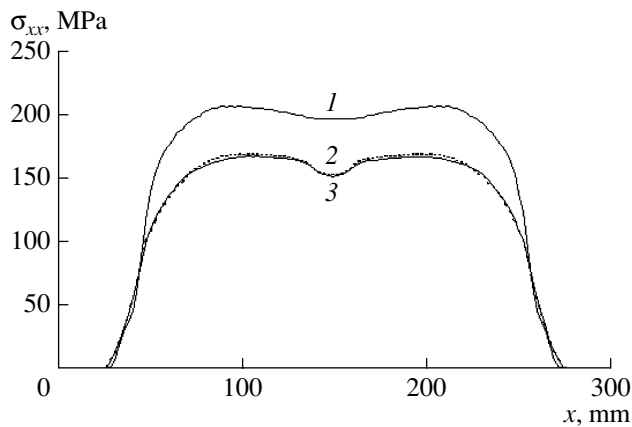


Fig. 5. Distribution of normal stresses along the joint weld (mode 2).

equal to 0.01 m (curves 1), 0.025 m (curves 2), and 0.05 m (curves 3) from the discharge channel symmetry axis. These dependences were obtained by solving the hydrodynamic part of the problem. In all the figures, the solid lines correspond to the first mode and the dotted lines correspond to the second mode.

Figures 4 and 5 show distribution of normal stressed along the joint weld before loading (curves 1) and in the moment of time when after the pulse load an equilibrium was achieved. Curves 2 in the figures were obtained taking into account the load due to the discharge channel only, curves 3 were obtained in the case of the hydrodynamic load. Figures 4 and 5 correspond to the first and the second mode of the electric power supply, respectively.

The given results show that the main contribution to the change in the joint weld stressed–strained state is made by the load created by the discharge channel. The effect of the hydrodynamic load is significantly less.

CONCLUSIONS

Studying numerically the stressed–strained state of joint welds described in the present work by a mathematical model, one may take into account only the load

on the surface due to the underwater spark discharge channel, because it renders a considerably stronger influence on the processes in the joint weld than the hydrodynamic load.

ACKNOWLEDGMENTS

We thank V.D. Polovinko and E.S. Yurchenko for providing experimental data for determination of laws of power supply into the discharge channel.

REFERENCES

1. Gulyi, G.A., *Nauchnye osnovy razryadno–impul'snykh tekhnologii* (Scientific Bases of Discharge–Pulse Technologies), Kiev: Naukova Dumka, 1990.
2. Vovchenko, A.I., Demidenko, L. Yu., and Yurchenko, E.S., Ways for Increasing Efficiency of Electro–Hydropulse Method for Decreasing Residual Stresses in Joint Welds, *Tyazh. Mashinostr.*, 2003, no. 2, pp. 34–36.
3. Vovchenko, A.I., Initial Conditions for Problem of Numerical Study of Underwater Spark Discharge Dynamics, *Pratsi IED NANU, Elektrodinamika: Zb. Nauk Pr.: K: IED NAN Ukraini*, 2001, pp. 117–120.
4. Barbashova, G.A., Polovinko, V.D., and Yurchenko, E.S., Influence of Pressure Pulse Parameters on Decreasing of Residual Stresses, *Elektron. Obrab. Mater.*, 2006, no. 4, pp. 60–64.
5. Opara, V.S., Kudinov, V.M., and Petushkov, V.G., Role of Bending Strain in Decreasing of Residual Welding Stresses by Electro–Hydropulse Method, *Avtomat. Svarka*, 1982, no. 3, pp. 20–23.
6. Vinokurov, V.A., *Svarochnye deformatsii i napryazheniya. Metody ikh ustraneniya* (Welding Strains and Stresses. Methods of Their Elimination), Moscow: Mashinostroyeniye, 1968.
7. Wilkins, M.L., *Calculation of Elastic–Plastic Flows, in Vychislitel'nye metody v gidrodinamike* (Computation Methods in Hydrodynamics), Moscow: Mir, 1967, pp. 212–263.
8. Fletcher, C.A.J., *Computational Techniques for Fluid Dynamics*, London: Springer-Verlag, 1988, vol. 1.

ELECTRICAL PROCESSES IN ENGINEERING AND CHEMISTRY

Kinetic Model of Electrochemical Nucleation

S. A. Baranov^a, Yu. D. Gamburg^b, and A. I. Dikumar^a

^a Institute of Applied Physics, Academy of Sciences of Moldova, ul. Akademiei 5, Chisinau, MD-2028, Republic of Moldova

^b Frumkin Institute of Physical Chemistry and Electrochemistry, Russian Academy of Sciences, Leninskii pr. 31, Moscow, 117071 Russia

Received October 26, 2006

Abstract—The kinetic model of electrochemical nucleation of micro- and nanoparticles is studied. The functional dependence of probability of the energy of the particle on the relative radius found earlier is used in nucleation in the statistical Heisenberg model. On the basis of the proposed theory, a simple ratio for calculation of probabilities of kinetic processes is obtained for the case of electrochemical nucleation.

DOI: 10.3103/S1068375507030040

INTRODUCTION

Formation of nanocrystalline structures most of all depends on the kinetics of nucleation, which includes the thermodynamics of the nucleation process only as an elementary step or event. Thus, the most probable dimensions of the particles in various physicochemical processes are also determined from simple thermodynamic relationships involving thermodynamic functions. For a specific statistical model, we managed to derive these functions in our previous research [1, 2]. The nucleation is usually treated as a chain of sequential processes; that is, the N -atom nucleus is formed by addition of one atom to an $(N - 1)$ -atom cluster or by a similar loss of atoms. Constructing a chain of Markov processes, one can obtain the Einstein–Fokker–Planck equation. Then it is worth noting that the kinetics of the nucleation process is simplified if the process of steady-state nucleation is examined [3]. Therefore, we shall further evaluate the possible dimensions of the particles and their correlation with the energy parameters using the simple ideas and thermodynamic functions obtained in our previous research.

The further analysis of the kinetic phenomena reduces to a semiquantitative Frenkel description where the velocity of the steady-state stream of formation of the most probable nuclei is defined as [3]

$$J \sim \exp\{-\Delta E_{cr}/kT\}, \quad (1)$$

where ΔE_{cr} is the activation energy of formation of the nucleus. In formula (1), the preexponential factor is omitted (see [3], p. 135 for more details).

The solution of the problem further reduces to calculation of the magnitude of the free energy.

Since an impression may be created that we have not analyzed other possible ways to solve the problem, let us discuss in detail why the proposed theoretical model was chosen.

CALCULATION OF THERMODYNAMIC FUNCTIONS

Earlier, we used a nonlinear equation to solve the formulated problem [1, 2]:

$$\theta'' + \theta'/\rho - a^2 \sin(\theta) \cos(\theta)/\rho^2 = 0, \quad (2)$$

where θ and ρ are the polar coordinates (ρ is a reduced quantity that varies from 0 to 1), and a^2 is defined as the ratio $(B + 1)/A$, where B is the energy of anisotropy and A is the constant of the exchange interaction.

The solution to Eq. (2) with the boundary conditions that we also discussed earlier [1, 2] has the form [1, 2, 4–7]:

$$\tan\{\theta_a/2\} = 1/\rho^a. \quad (3)$$

If $a = 1$, there is no anisotropy in the system, and if $a \gg 1$, the external anisotropy exceeds the exchange interaction in the system.

To compare the results for the two cases, we present the calculated variation of the angle θ from the coordinate origin (where $\rho = 0$) of the cylindrical particle to its surface (where $\rho = 1$). At the same time, let us limit our examination to the two extreme cases of the value of the parameter a :

(1) curve 1 corresponds to the case $a = 1$, which relates to the condition when microscopic anisotropy is absent;

(2) curve 2 corresponds to the case $a = 10$, which refers to the condition when microscopic anisotropy exists.

It is shown that, in the first case, it is difficult to isolate the volume of the cylinder that can be attributed to the surface energy, since the angle θ changes smoothly as a function of ρ . In the second case, when $a = 10$, a range can be chosen whose volume amounts to the surface energy of the cylindrical particle. In the framework of our qualitative examination, we may conventionally

assume, for example, that the surface layer is counted from the value $\rho = 0.8$. We make this choice using only the shape of curve 2, which sharply decreases for $\rho > 0.8$. The volume that defines the surface energy of the cylinder amounts to 36% of the cylinder's volume in this case. When a increases further (for example, by a factor of 2), this volume will amount to less than 10% of the cylinder's volume.

Then we shall investigate the physical nature of the examined anisotropy for the case of electrochemical nucleation. This anisotropy can be generated using the distribution of the electric field in the near-electrode layer, because the dimensions of the particles become comparable with the dimensions of the layer.

Let the surface energy change in the nucleation process according to the Lippman equation [8, 9]:

$$-d\sigma = qd\varphi, \quad (4)$$

where q and φ are the charge and potential on the surface. In the approximation of the constant capacity of the double layer C

$$q = C\varphi, \quad (5)$$

we obtain for the change in the surface energy $\Delta\sigma$

$$\Delta\sigma = C\Delta(\varphi^2)/2. \quad (6)$$

The change in the surface energy may be due to the anisotropy introduced above. Actually, if we assume that an asymptotic functional dependence occurs,

$$\Delta(\varphi^2) \sim 1/\rho^2, \quad (7)$$

then we finally obtain for the parameter a^2

$$a^2/r_c = C/2, \quad (8)$$

where r_c is the equilibrium value of the nanoparticle dimension (we evaluate the r_c value as $10^{-5} \text{ cm} > r_c > 10^{-7} \text{ cm}$).

For the evaluation, we take the capacity of a mercury electrode that is known to be on the order of [9]

$$C_{\text{Hg}}/2 \sim 10^7 \text{ pF/cm}^2 \sim 10^7 \text{ 1/cm (in CGS units)}. \quad (9)$$

If we confine ourselves to the upper limit of the r_c value, then we obtain for the evaluation of the dimensionless quantity a

$$a \sim 10.$$

This leads to the conclusion that, with the aim of creating equilibrium particles of nanoscale dimensions, one needs to increase the electric capacitance of the system where the particle is being formed.

Further, we assess how the free energy changes from the center of the particle to its surface. The layer-by-layer change of the free energy of the cylindrical particle is examined. The formula for the energy that was used to obtain the equation of motion has the form

$$E(\rho) = T + W, \quad (10)$$

where $T = A(\theta')^2/2$ is the exchange interaction energy (defined in [1, 2]) that represents the analog of the kinetic energy of a quasiparticle, and $W = B(\sin\theta)^2/2\rho^2$ is the anisotropy that in this case represents the potential energy (see [1, 2] for more details).

Substituting the solution to Eq. (6) in the form (7) into the expressions for T and W , we obtain

$$T = W \quad (11)$$

(the consequence of the virial theorem) and

$$T + W = 2A(a^2/\rho^2)[(\rho)^{2a}/(1 + \rho^{2a})^2]. \quad (12)$$

Let us analyze expression (12). In a particular case where there is no anisotropy, $a^2 = 1$, we obtain

$$T_1 + W_1 = 2A/(1 + \rho^2)^2, \quad (13)$$

and the energy on the cylinder's surface tends to A (at $\rho^2 = 1$). In the case where $B > 0$, the energy on the cylinder's surface tends to Aa^2 , and the change is more dramatic for greater B values. Hence, we may consider that precisely this parameter is the corresponding parameter to the thermodynamic surface energy that in this case plays the role of a peculiar activation barrier that phenomenologically enters formula (1). Note that, in our model, the case is realized where it is difficult to divide the total energy into the surface energy and the bulk energy, and below it will be determined as an effective surface energy.

The energy inside the particle tends to $2A$ in the case of (13), but in the same passage to the limit, it tends to zero in the case of (12). This specific step of the free energy is characteristic of a phase transition that occurs in the system when an infinitely small anisotropy arises. Similar phase transitions are known (see, for example, [7]), and here they are obtained as a result of the analysis of rather simple expressions.

To find the total energy of the particle (related to the unit length of the cylinder), we need to take the integral of $E(\rho)$ over the volume. For a particular case $a^2 = 1$, this integral is equal to A because there is no other kind of energy in the system. In the general case of sufficiently large a^2 , the total energy tends to the energy of anisotropy B . A more accurate expression for the energy has the form

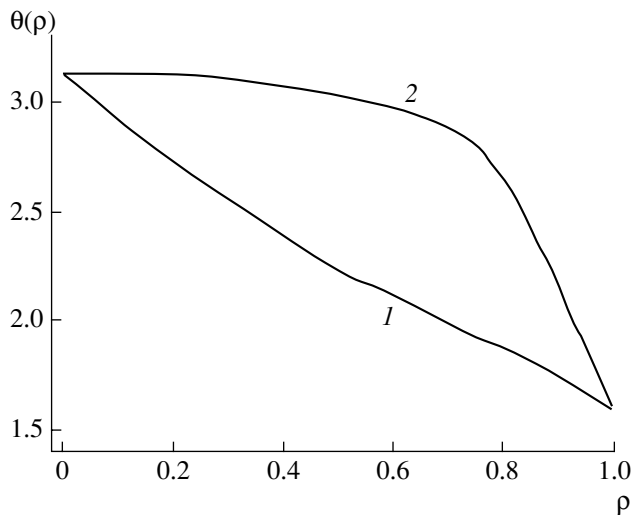
$$E = \int_0^1 E(\rho)\rho d\rho = 2Aa^2 D(a), \quad (14)$$

(hereafter the factor 2π is omitted),

where

$$D(a) = \int_0^1 \rho d\rho (\rho)^{2a}/[\rho^2(1 + \rho^{2a})^2]. \quad (15)$$

It is easy to demonstrate that $D(a)$ for $a = 1$ and $D(1) = 0.5$. In the general case, we may consider that



Variation of the slope angle relative to the cylinder axis $\theta(\rho)$ that characterizes the energy of the particle vs. the reduced radius ρ of its coordinate.

this formula will also qualitatively describe more complicated models, where integral D means the linear (radial) ratio of the fraction of the surface to the volume that corresponds to the figure shown above. Further, we shall present the generalization of the formula to the anisotropic models.

We can also show that, for our model,

$$E = (AB)^{1/2}. \quad (15a)$$

We shall consider this quantity to be the magnitude of the activation energy of the instanton E , and it is significantly less than the value of the surface energy.

CALCULATION OF THE KINETICS OF THE NUCLEATION PROCESS

In the framework of the case where formula (1) is applicable, we obtain the formula for the velocity of the steady-state stream of formation of the most probable nuclei in the form

$$J \sim \exp\{-(2Aa^2D(a)V)/kT\}, \quad (16)$$

where V is the volume of the particle.

We shall not discuss here the problem related to the preexponential factor (it is described in detail in [3], p. 135). Let us consider the physical meaning of formula (16). The factor

$$Aa^2 \sim B \quad (17)$$

represents the specific surface anisotropy having an electrochemical nature, and $D(a)$ is the fraction of the surface with the given energy. Thus, we come to formula (1), where ΔE_{cr} has the meaning of the surface energy of the nanoparticle (which dominates in the given case).

Let us discuss a possible variant of a high-temperature limit of the kinetic theory. With increasing temperature, the processes of growth of a stationary stream due to temperature transitions over the energy barrier of the instanton are possible. The energy height of the barrier (by analogy with micromagnetic problems) is defined in this case by the magnitude from (15a) (accurate to 2π):

$$E = (BA)^{1/2}/r_c. \quad (18)$$

For the potential energy of our topological model, we introduce instead of the usual time a complex time inversely proportional to the temperature [10]. Then we obtain for the evaluation of the potential barrier

$$W \sim B(1 - \exp\{-EV/kT\}). \quad (19)$$

This demonstrates that the aforementioned effects will be significant only for temperatures

$$kT_c \sim EV. \quad (20)$$

Note that, precisely for such temperatures, the conditions of steady-state kinetics are violated. In this case, nonactivation processes that we do not examine here will define the kinetics of the process. Therefore, we shall consider the following expression to be the applicability criterion of (16):

$$T < T_c. \quad (21)$$

It is clear from simple physical reasons that, when the temperature approaches the critical value T_c , the formed particles will begin to be destroyed owing to the effect of the temperature. To assess T_c , we assume that the volume of the particle is on the order of 10^{-24} m^3 , and to find E , we take the integral from 10^{-2} to 10^{-1} J m^{-3} . Then we obtain for T_c the range from 100 to 1000 K. Note that an increase in the energy of anisotropy also leads to an increase in the temperature limit at which the conditions of steady-state kinetics are not yet violated.

CONCLUSIONS

In our research, the following new qualitative results were obtained:

- the concept of the energy of anisotropy introduced in theory acquires the meaning of the electrostatic energy of a double electric layer. With the aim of creating equilibrium particles with nanodimensions, the electric capacitance of the system where such a particle is grown should be increased;
- for the velocity of the steady-state stream of formation of the most probable nuclei, we obtain a result that allows us to suggest that effective control is possible over the nucleation process by electrochemical methods.

ACKNOWLEDGMENTS

This work is supported by the Program RFFI—Moldova, grant no. 06.11CRF.

REFERENCES

1. Baranov, S.A., Statistical Model for Analyzing Nucleation in the Electrochemical Processes, *Elektron. Obrab. Mater.*, 2005, no. 4, pp. 4–6.
2. Baranov, S.A., Dikusar, A.I., and Gamburg, Yu.D., Abstracts of papers, *IV mezhdunarodnaya nauchnaya konferentsiya "Kinetika i mekhanizm kristallizatsii. Nanokristallizatsiya. Biokristallizatsiya"* (IV Int. Conf. "Kinetics and Mechanism of Crystallization. Nanocrystallization. Biocrystallization"), Ivanovo (Russia), 2006, p. 142.
3. Gamburg, Yu.D., *Elektrokhimicheskaya kristallizatsiya metallov i splavov* (Electrochemical Crystallization of Metals), Moscow: Yanus, K, 1997.
4. Baranov, S.A., The Theory of Nucleation, *Mold. J. Phys. Sciences*, 2006, vol. 5, no. 2, pp. 209–210.
5. Baranov, S.A., Laroze, D., Vargas, P., and Vazquez, M., On Micromagnetic Theory of Thin Cast Amorphous Microwires, *Physica B*, 2006, vol. 372, pp. 320–323.
6. Baranov, S.A., Vazques, M., and Usenko, V.P., Magnetization of a Thin Cast Amorphous Microwire in a Zero Magnetic Field, *Elektron. Obrab. Mater.*, 2005, no. 2, pp. 89–91.
7. Izyumov, Yu.A. and Skryabin, Yu.N., *Statisticheskaya mekhanika magnitouporyadochennykh sistem* (Statistical Mechanics of the Systems with Magnetic Ordering), Moscow: Nauka, 1987.
8. Frumkin, A.N., Petrii, O.A., and Damaskin, B.B., The Concept of the Charge of an Electron and the Lippman Equation, *Elektrokhimiya*, 1970, vol. 6, no. 4, pp. 614–630.
9. Antropov, L.I., *Teoreticheskaya elektrokhimiya* (Theoretical Electrochemistry), Moscow: Vysshaya Shkola, 1975.
10. Feynman, R.P. and Hibbs, A.R., *Quantum Mechanics and Path Integrals*, New York: McGraw-Hill, 1965.

**ELECTRICAL PROCESSES
IN ENGINEERING AND CHEMISTRY**

On Modeling of Processes of Moisture Circulation and Electric Charge Separation in the Atmosphere

F. P. Grosu^b, M. K. Bologa^a, A. A. Polikarpov^a, and O. V. Motorin^a

^a *Institute of Applied Physics, Academy of Sciences of Moldova, ul. Academiei 5, Chisinau, MD-2028, Republic of Moldova*

^b *Moldova State Agrarian University, ul. Mircesti, Chisinau, MD-2049, Republic of Moldova*

Received March 6, 2007

Abstract—The possibilities of obtaining water and electric energy from the atmosphere by means of simulation of the local atmospheric moisture cycle as well as electrical phenomena which accompany it in both natural and laboratory conditions are discussed. The basic possibility of achieving these goals according to the natural analogy is shown experimentally.

DOI: 10.3103/S1068375507030052

INTRODUCTION

One of the most widespread natural atmospheric cycles is moisture circulation, which comprises the following sequence of thermodynamic processes: water evaporation from the Earth's surface, its rise in vapor form to upper colder strata of the atmosphere, vapor condensation in these strata and formation of clouds, and water falling on the Earth in the form of precipitation [1]. The whole cycle is more or less obviously accompanied by electrical phenomena caused by separation of electric charges and concluding with discharges in the form of various types of lightning and glows.

Study of these processes and phenomena in aggregate is of current interest, at least, for the following purposes: forecast and control of weather, and obtaining water and electric energy from the atmosphere; this is possible both directly from the natural phenomena themselves and from physicomathematical (theoretical) and/or experimental phenomena in natural or laboratory conditions.

At present, atmospheric processes are studied on a global scale by virtue of artificial satellites orbiting the Earth using computer modeling of relevant mathematical equations and their solutions. The results of these investigations are widely applied, in particular, for achieving the aforementioned goals, as well as in aviation, navigation, agriculture, etc.

As to the processes of obtaining water and electric energy, they require a local modeling of the atmospheric moisture circulation and atmospheric electricity accompanying it. The present work is devoted to such a modeling; for obtaining water from the atmosphere and soil, it is necessary to model the water cycle only.

EXPERIMENTAL

Moisture Circulation Modeling in Natural Conditions

Obtaining water for practical needs directly, i.e., for drinking, irrigation, etc., requires carrying out natural modeling, not laboratory modeling. The solution of this problem is stated in [2, 3] (first parts).

The solution of the problem consists in the following. On the slope of a hill, a so-called solar vapor collector (SVC) is built. It is, in essence, a hothouse located along the slope (see the schematic diagram in Fig. 1) in such a way that one of its edges is at the bottom of the slope, in warmer strata of the atmosphere, and the other is at the top of the slope, in colder strata. For this purpose, the hothouse (SVC) must be sufficiently long, on the order of tens or even hundreds of meters. Then the pressure difference due to corresponding differences of heights and temperatures, which would lead to movement of moist air upwards inside the SVC, may be appreciable.

There are two main requirements to the slope: it must be situated on the sunny side and be sufficiently moist; that is, the locality should be chosen near reservoirs, water springs, marshes, etc. Both of these requirements satisfy the condition for obtaining a sufficient amount of moist air in the hothouse. The moisture itself is formed in the result of its evaporation from soil at the base of the SVC (Fig. 1). As was already mentioned, a pressure difference appears at the ends; therefore, in the upper and lower parts of the SVC, adjustable windows for air going in and out are made. Thus, moisture can come to the collector from both the soil and the surrounding atmosphere.

Evaporation of moisture and its rise in vapor form are modeled in the SVC. The condensation process is realized in a vapor condenser (VC) specially built at the top of the SVC, where vapor condensation in clouds is modeled. The condenser is cooled from the outside

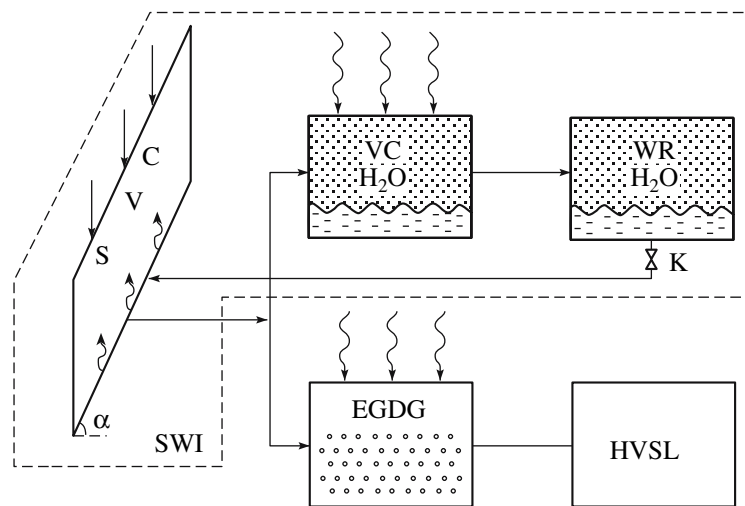


Fig. 1. Solar–wind energy complex. SVC is the solar vapor collector; VC is the vapor condenser; WR is the water reservoir; EGDG is the electrogasdynamic generator; HVSL is the high-voltage supply line; K is the faucet; ↓ is solar rays; ↷ is wind; ↑ is vapor.

owing to wind; therefore, the solar collector combined with the condenser is called a solar–wind installation (SWI). Reverse motion of condensate from the VC to the collector through the faucet *K* would artificially simulate the natural cycle; however, for practical purposes, the condensate goes into a special water reservoir (WR). This completes the process of moisture circulation and its use in the solar–wind installation (Fig. 1).

Obtaining Electric Energy

For solution of the second problem, an electrogasdynamic generator (EGDG) is designed [2–4], a simplified calculation of which is given in [5].

The principle of operation of the EGDG is the following. There is a system of electrodes of the “needle–ring” type supplied with high dc voltage ($U \geq 2\text{--}3$ kV). As is known, in such a system, there appears a corona discharge [6] and, in turn, a unipolar space charge of sign of the corona electrode, the needle in our case. If wind blows on the corona system, the space charge is blown off to the side of the third counterelectrode–collector usually in the form of a metal net. Thus, the charge from the corona electrode is “pumped” to the counterelectrode, creating a potential difference preventing “pumping” of charges by wind. This difference is the emf of the EGDG.

However, in pure air, the effect of emf generation is weak owing to low windage, high mobility of air ions [7]; hence, it was proposed to use, as a working medium in the EGDG, a water aerosol [2, 3, 4, 7] obtained by mixing warm moist air from the SVC and cold surrounding wind (Fig. 1) supplied to the EGDG through a special branch pipe [2, 3]. In this case, the EGD effect increases significantly.

It seems to us that something of the kind takes place in atmospheric conditions; therefore, hypothetically,

some aspects of the process of charge separation in clouds are modeled in the EGDG.

The solar–wind installation, shown inside the dotted line, and the EGDG form the solar–wind energy complex (SWEC). Practical realization of the given complex obviously requires additional experimental research under laboratory conditions.

Laboratory Modeling of Atmospheric Processes of Moisture Circulation and Charge Separation

Design features of the experimental complex and the physical processes taking place in it are described below; the basic results obtained are discussed as well.

Solar Vapor Collector

An experimental model of the SWI is presented in Fig. 2 showing a collector in the form of a gutter of length $l = 1.4$ m, width $b = 0.25$ m, and controllable height of moist air strata $0.02 \text{ m} \leq h \leq 0.15$ m. More than half of the gutter is filled with soil, mainly a mixture of sand and aglite, of thickness $H = 0.2$ m. In the middle of soil layer l , in the longitudinal direction, drainpipes 3 are installed for forwarding the obtained condensate back into the soil and simulation of a moisture circulation cycle. The gutter is covered with polyethylene film 2 .

An electric floodlight S simulated the Sun. The temperature on the surface of the soil and inside it was measured by means of thermocouple 7 . Window 9 served for regulation of external air forwarded to the SVC. In addition to height h , the angle of inclination to the horizon α was an adjustable parameter that could be varied within the range of $0^\circ \leq \alpha \leq 45^\circ$. The soil was moistened with water. The soil was heated by the floodlight; however, it appeared that such heating quickly, in about 30 min, led to drying of the soil surface and to a sharp

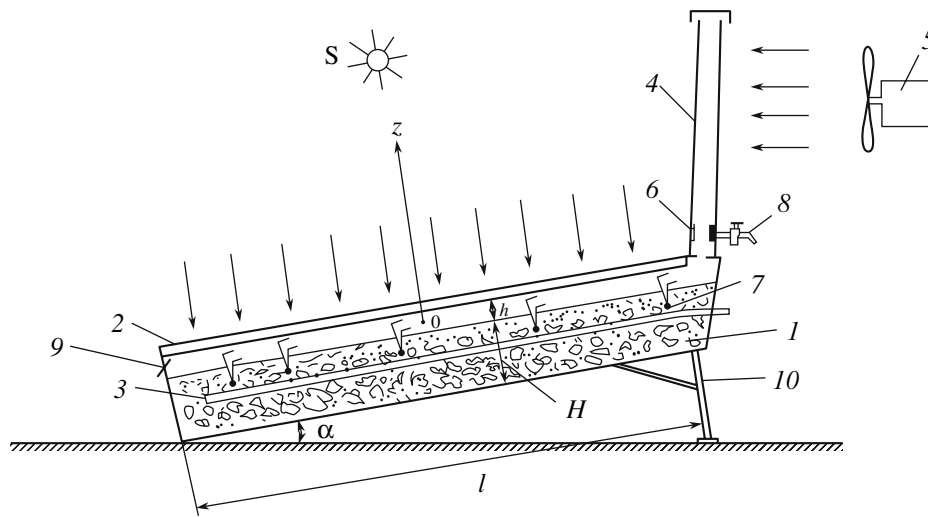


Fig. 2. Solar vapor collector: (1) soil; (2) film; (3) drainpipe; (4) condenser; (5) ventilator; (6) condensate; (7) thermocouple; (8) faucet; (9) window; (10) support.

decrease in vapor formation in the collector. Theoretical estimations have shown that, in natural conditions, the drying time is much greater ($\tau \sim 10$ h); therefore, heating by the floodlight did not simulate the natural process; we had to mount a wire heater in ceramic electrical insulation $\sim 2\text{--}3$ cm deep in the soil.

The problem of transport of moist air in the SVC in the laminar mode is solved in [8], where discharge of water in vapor form through the cross section of the SVC channel is expressed by the formula

$$G_v = \gamma b \left(\frac{s_0}{b} G + \frac{A h^3 r_s}{120} \right), \quad (1)$$

where γ is the moist air density; s_0 is the average relative humidity of the air at the level $z = 0$ (Fig. 2); and G is its volume discharge, m^3/s , determined by the formula

$$G = b \int_{-h/2}^{h/2} v(z) dz = -\frac{\Delta P b h^3}{l 12 \eta}, \quad (2)$$

where $\Delta P/l$ is the pressure drop along the channel of length l , and η is the dynamic coefficient of air viscosity. The parameter A characterizes the natural convection (NC) of combined origin (thermal $\beta\theta_s$ and moisture $\beta_s r_s$) and it is equal to

$$A \equiv \frac{g(\beta\theta_s + \beta_s r_s) \sin \alpha}{6\nu}, \quad (3)$$

where $\beta = -\frac{1}{\gamma_0} \left(\frac{\partial \gamma}{\partial T} \right)_0$; $\beta_s = -\frac{1}{\gamma_0} \left(\frac{\partial \gamma}{\partial s} \right)_0$; $\nu \equiv \eta/\gamma$;

and the differences of temperature θ_s and moisture r_s on the lower and upper bases of the stratum are given by the formulas

$$\theta_s \equiv T_2 - T_1 = T \left(-\frac{h}{2} \right) - T \left(\frac{h}{2} \right); \quad (4)$$

$$r_s \equiv S_2 - S_1 = S \left(-\frac{h}{2} \right) - S \left(\frac{h}{2} \right).$$

Formulas (1) and (2)–(4) give a complete physical picture of what must be done to increase the efficiency of the SVC.

Dwelling briefly on the physical aspects of formula (1), we should note that the first term describes the vapor flow caused by the unbalanced gradient of pressure $\Delta P/l$, for example, wind head; and if the channel is closed at the ends, then $G = 0$, and according to formula (1), the vapor mass transport is realized exclusively through NC,

$$G_v = \frac{\gamma g(\beta\theta_s + \beta_s r_s) b h^3 r_s \sin \alpha}{720\nu}, \quad (5)$$

and precisely the moisture factor ($r_s \neq 0$) leads to moisture transport ($G_v \neq 0$). The rate profile is cubic, $v \sim z^3$. In the case of an open channel, the cubic profile is superimposed by a parabolic quadratic one caused precisely by the pressure differential; however, under laboratory conditions with small l , the differential is low and we will neglect it at first, confining ourselves for calculations to formula (5). The convective moisture transport, in contrast to the hydrodynamic one ($\Delta P \neq 0$), is one of the peculiarities of the solar collector functioning under laboratory conditions.

Let us note that one-dimensional convective flow is unstable at the Grashof numbers

$$Gr \equiv \frac{g(\beta\theta_s + \beta_s r_s) h^3}{\nu^2}, \quad (6)$$

being close to the critical ones $Gr^* \leq 10^4$ and at $\alpha \sim 30^\circ$ [9]. Assuming in (6) $\beta\theta_s + \beta_s r_s \sim 10^{-3}$ and $\nu \sim 10^{-4} \text{ m}^2/\text{s}$ [10], we find the critical height $h_* \sim 20 \text{ cm}$, above which the flow is reconstructed into a cellular one, that is, cells of the Benar type [10] rolling up and down in the longitudinal direction; upon a further increase in the Gr number, the flow becomes turbulent [9]. The critical values of h do not exceed tens of centimeters according to more accurate estimates. However, at first, as was already mentioned, we will confine ourselves to formula (5), which is justified under two conditions:

$$h < h_* \equiv \left(\frac{\nu^2 Gr^*}{g(\beta\theta_s + \beta_s r_s)} \right)^{1/3}, \quad (7)$$

$$h \ll b. \quad (8)$$

The second one is not connected with stability of motion, but is a condition of the plane-parallel flow. It goes without saying that, between two values of h satisfying jointly conditions (7) and (8), one should choose the smaller one.

Vapor Condenser

The flow of moist air from the collector comes to vapor condenser 4 (Fig. 2), which is a thin-walled metal cylinder having height $h_c = 880 \text{ mm}$ and diameter $d_c = 70 \text{ mm}$. From the outside, air was blown on the condenser from a typical room ventilator, which not only simulated wind, but in fact cooled the condenser. It should be noted that cooling also occurred by natural convection.

The condensate discharge on the basis of [11] was determined by the generalized formula

$$\frac{G_c}{G_{CO}} = 5.88 \times 10^{-3} \Pi (GrPr)^{0.25} Re^{0.6}, \quad (9)$$

where G_{CO} is the vapor mass discharge at the condenser

inlet; $\Pi \equiv \frac{\lambda\theta_0 S}{rdG_{co}}$; $Re \equiv \frac{\nu d}{\nu}$; $Pr \equiv \nu/a$; S is the lateral

area of the condenser; d is the diameter; ν is the ventilator blow rate; and θ_0 is the difference of the temperatures of the condenser surface and the surrounding air.

Electrohydrodynamic Generator

The EGD generator designed for a natural energy system where aerosol was formed as a result of vapor mixing with cold air at the EGDG inlet was in a general outline described above. The first experiments with this method of obtaining aerosol showed insufficient efficiency of the EGDG operation; therefore, another variant was used where the corona electrode, in the form of a pinned spherical surface, was sprayed with water and simultaneously subjected to airflow. As a result, water dispersion took place owing to both electrostatic forces

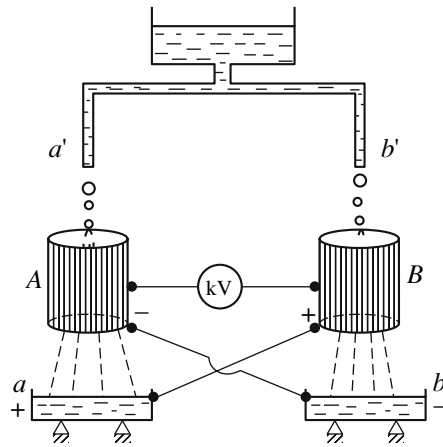


Fig. 3. Kelvin generator: a' and b' are the capillaries; A and B are the cylinder electrodes; a and b are the vessels for collection of charged water.

of repulsion and hydrodynamic factors. This is another peculiarity of the EGDG laboratory model.

This method of obtaining a coarse dispersion working medium for the EGDG appeared to be more efficient, but it requires an autonomous source of high voltage for maintaining the corona discharge, which is absent or converted in natural conditions. Such a solution of the problem is necessary when electricity "just" appears; under laboratory conditions, it may be ingeniously solved by means of a Kelvin generator (KG), a schematic diagram of which is shown in Fig. 3.

The principle of its operation is the following. Let the first drop, e.g., the one which has fallen from the capillary a' , have a random positive charge. This charge, flowing into the metal vessel a isolated from the ground, will charge it and the cylindrical electrode B electrically connected to it (Fig. 3). Then the next drop falling from the capillary b' will be charged by the negative charge induced from the electrode B , and this charge will be transferred to the vessel b and the electrode A . The next drops from the capillary a' will intensify their positive charge and the ones from the capillary b' their negative charge.

Thus, between the vessels a and b or the electrodes A and B , there appears a potential difference, which may be directly measured by an electrostatic kilovoltmeter, and in this case it will in fact be the KG emf. If the cylinders A and B are closed with a high-ohmic resistor, being a load resistance, current will flow in it.

The system of the vessels and electrodes (a, B) and (b, A) is a condenser, and the charge accumulated by it will be determined by the formula

$$Q = C\varepsilon, \quad (10)$$

where C is the electrical capacitance and ε is the KG emf.

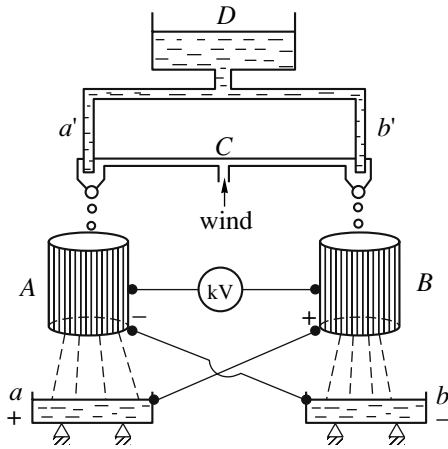


Fig. 4. Combined EGD generator.

Hence, the condenser charging current is equal to

$$I = \frac{dQ}{dt} = C \frac{d\varepsilon}{dt}. \quad (11)$$

Let us note that, as the dimensions of drops increase, their merging occurs and the jet mode of KG operation takes place when the generated potential difference increases significantly. The simplest KG with dimensions of the vessels a and b and the cylinders A and B of about 10×10 cm can give an emf ε up to 10–15 kV for several minutes. In the jet mode, charging is realized in a matter of seconds.

A combined EGD generator is more effective. In it, drops from the capillaries a' and b' are additionally blown off by airflow by virtue of a special construction in the form of the pipe C put on the droppers a' and b' according to Fig. 4.

We do not dwell on details of the operation of the Kelvin generator in thunderclouds. It is probable that moist air jets in the combined variant in Fig. 4 will give some explanations.

Connection of the foregoing components of the system with the EHD generator is realized directly through the condenser flow into the vessel D feeding the EHD generator; a schematic diagram of the whole energy system is shown in Fig. 5. The presence of the Kelvin generator instead of an electrogasdynamic one is one more difference of the initial variant of the system from the considered laboratory one.

The system operates according to the following scheme. Owing to solar heating, water evaporates from the soil, forming moist air in the collector. Under favorable conditions, moist air penetration from the outside of the SVC is admissible. The moist air owing to natural convection flows into the vapor condenser, from where it goes, in the form of a condensate, to the EHD generator or KG, or to a generator of combined type. If necessary, the condensate may flow into the water reservoir (WR) through the faucet K . From the EHDG, the

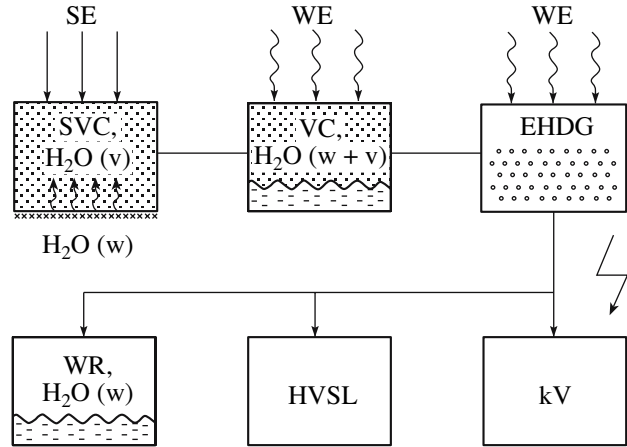


Fig. 5. Block diagram of wind energy complex with electrohydrodynamic generator. SVC is the solar vapor collector; VC is the vapor condenser; EHDG is the electrohydrodynamic generator; WR is the water reservoir; HVSL is the high-voltage supply line; SE is the solar energy; WE is the wind energy; $\downarrow\downarrow$ is the solar radiation; \downarrow is wind; \uparrow is vapor.

process water goes to the WR, from where in organization of a cycle it can again flow to the collector through the drainpipes. The generated emf after relevant transformations is fed to the high-voltage supply line for consumers of electric energy.

In the laminar mode at $h = 0.07$ m and $\alpha = 27^\circ$, on average $G_C \sim 10^{-4}$ kg/s and emf of ~ 15 kV at $I \sim 1 \mu\text{A}$ were obtained. In natural conditions, these effects are shown to be tens of times stronger.

CONCLUSIONS

The possibilities of obtaining of water and electric energy from the atmosphere and soil are considered, and ways to realize them are discussed.

Physical considerations and formulas are given, according to which an experimental installation simulating natural atmospheric processes of moisture circulation and separation of electric charges is designed.

The basic possibility of physical modeling of the aforementioned processes under laboratory conditions and their practical application is shown.

Along the complicated track of studying atmospheric phenomena, including electrical phenomena, for both scientific and applied purposes, only the first steps have been done, which indicate that reserves exist for improvement of the solar energy electrohydrodynamic system.

REFERENCES

1. Khrgian, A.Kh., *Fizika atmosfery* (Physics of Atmosphere), Leningrad: Gidrometeoizdat, vol. 2, 1978.

2. Cojuhari, I. and Bologa, M., *Instalatie eoliana electrohidrodinamica. Brevet de inventie*, MD-2199, (13) B1, 2003.
3. Bologa, M., Cojuhari, I., and Leu, V., *Instalatie eoliana electrohidrodinamica. Brevet de inventie*, MD-2028, BOPI, 2005.
4. Rubashov, I.B. and Bortnikov, Yu.S., *Elektrogazodinamika* (Electric Gas Dynamics), Moscow: Atomizdat, 1971.
5. Bologa, M.K., Grosu, F.P., and Kozhukhar', I.A., To Calculation of Wind Electric Gas Dynamic Generator, *Elektron. Obrab. Mater.*, 2003, no. 4, p. 37.
6. Kaptsov, N.A., *Elektricheskie yavleniya v gazakh i vakuume* (Electric Phenomena in Gases and Vacuum), Moscow: Gostekhizdat, 1950.
7. *Vetro-energetika* (Wind Energetics), de Renzo, D., Ed., Moscow: Energoatomizdat, 1982.
8. Grosu, F.P., Natural Convection of Charged Moist Air in Inclined Plane Condenser, *Elektron. Obrab. Mater.*, 2005, no.3, p.50.
9. Gershuni, G.Z. and Zhukhovitskii, E.M., *Konvektivnaya ustoychivost' neszhimaemoi zhidkosti* (Convective Stability of Uncompressible Liquid), Moscow: Nauka, 1972.
10. Landau, L.D. and Lifshits, E.M., *Gidrodinamika* (Hydrodynamics), vol. 6, Moscow: Nauka, 1986.
11. Isachenko, V.P., Osipov, V.A., and Sukomel, A.S., *Teploperedacha* (Heat Transfer), Moscow: Energiya, 1975.

ELECTRICAL PROCESSES
IN ENGINEERING AND CHEMISTRY

Modeling of Nonstationary EHD Flows in a Wire-Plane Electrode System

V. L. Dernovskii, Yu. K. Stishkov, and A. A. Statuya

St. Petersburg State University, ul. Ul'yanovskaya 3, St. Petersburg, Petrodvorets, 198504 Russia

Received January 16, 2007

Abstract—The object of this work is nonstationary EHD flow modeling in a wire-plane electrode system for researching processes of space-charge formation and evolution, and the features of its movement in the interelectrode gap are investigated. The set of equations describing the modeling process is appreciably nonlinear. The final-element modeling package ANSYS was used for solving this problem. A special algorithm was developed. It was realized as a package of programs based on the approximation that the charge is “frozen” in the liquid. Results of calculations are represented as velocity vector plot evolution, pressure distributions, and EHD flow traces. A typical feature of EHD flow is the formation of a charged thin stream that crosses the interelectrode gap.

DOI: 10.3103/S1068375507030064

A lot of works [1, 2] are dedicated to EHD flow properties and the methods of their modeling. In recent years, an EHD [3] flow computer processing procedure has been developed that permits reestablishing the distribution of velocities and accelerations in the interelectrode gap.

The goal of this work is to model the EHD flow establishment process in an asymmetrical system of electrodes of wire-plane type (Fig. 1) in order to study the features of buildup, development, and movement of the space charge in the interelectrode.

There are a number of investigations on modeling of EHD flows in the given electrode system concerning the stationary case [4, 5]. Work [4] is concerned with the computer modeling of structural features of electrohydrodynamic flows in asymmetrical electrode system of wire (blade)-over-plane type.

In [5] it is shown that at significant interelectrode distances, the pressure along the majority of the gap is constant. There are only local regions of underpressure (near the active electrode) and overpressure at the flat electrode and it is described the effect of these zones on flow structure. The bands of acceleration and deceleration being overlapped it is observed the decay of EHD flow efficiency.

It is known as well that EHD flows appear with some delay relative to the moment of voltage switch-on. It is explained by the forming of a certain charged layer near the electrode surface before the EHD flow begins to build up [6].

The problem of space-charge distribution at the first step of loading requires special discussion. It would appear reasonable that at the initial moment the charge is distributed in the layer, having the form of a circle. However, as numerical experiments show [7], at such a

distribution the electric forces are symmetrical about the cylindrical electrode and generated flows have no certain direction. At the same time, under unipolar injection, the developing distribution of the space charge is nonsymmetrical relative to the cylindrical electrode surface, but is elongated towards the flat electrode (Fig. 2).

Hence, it is logical to define the charged region initial shape as slightly shifted towards the counterelectrode. From the stationary charged layer under the effect of Coulomb forces, a stationary EHD flow arises, shifting the electric charge along the streamlines. As a result, the charged region assumes the form of narrow strip extending from the wire electrode to the flat one. Electric charge density distribution in the new region is assumed uniform as well. Such assumptions are justified if the ions forming the space-charge region are considered frozen into liquid; that is, the electric Reynolds number is well over 10.

The set of equations governing the modeled process is essentially nonlinear. One reason for nonlinearity is, for example, the dependence of electric field on the

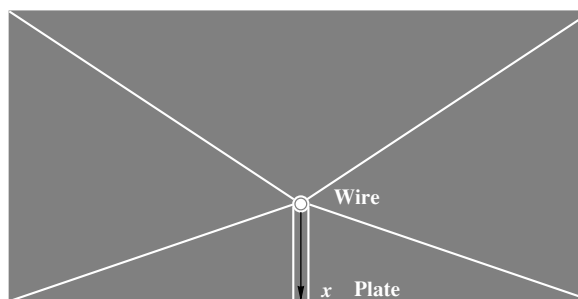


Fig. 1. The problem geometry.

magnitude of the space charge. The method of finite elements is the most effective for solving such mathematical problems. Applied packages implementing this method with the aim of solving different problems have been widely used recently.

In order to solve this challenge, the modeling was performed with the help of the finite-element package ANSYS using electrostatic, thermal, and hydrodynamic types of analysis, for which purpose the algorithm, given below and realized in the form of a program, has been elaborated. In spite of the rich potential of the ANSYS/Multiphysics package, the solution of the EHD problem with the aid of a standard program is considered impossible. The basis for the algorithm is the idea proposed in [7].

The electrostatic problem with the uniform distribution of space charge, designated in the limits of the ring, and with a specific potential difference (25 kV) on the electrodes is solved as the first step. From this solution, the distribution of the Coulomb forces in the charged region is found. The electric force field is calculated as the product of space-charge density by electric intensity in every net node. Then the computed force density is carried into the hydrodynamic part of the analysis. The principle distinction of the algorithm from similar ones is that it allows one to model the flow development under dynamic conditions, not only it is possible to keep an eye on the movement of the charge deep into the interelectrode gap, but on the variation of the thickness of the charged area.

The problem is solved in the approximation that the charge is frozen into liquid [2]; then under the laminar flow conditions it is considered to have been transferred only along the liquid flow lines. Migration of the charge in its own and external fields is not taken into account, which is why the configuration of the charged region's shape is determined with the help of construction of the liquid flow line performed after the hydrodynamic part of the problem has been computed. The velocity vector

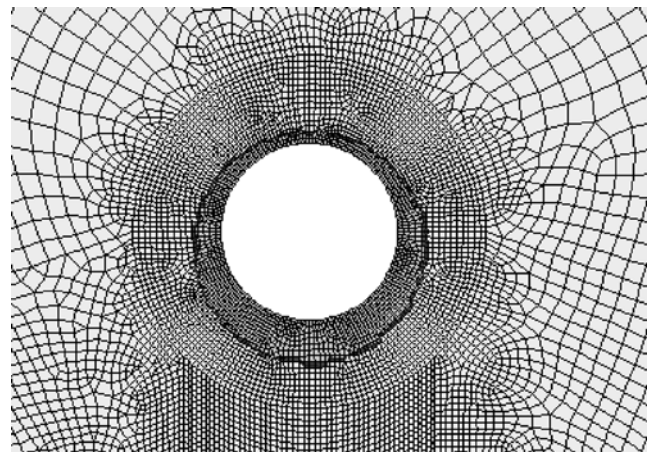
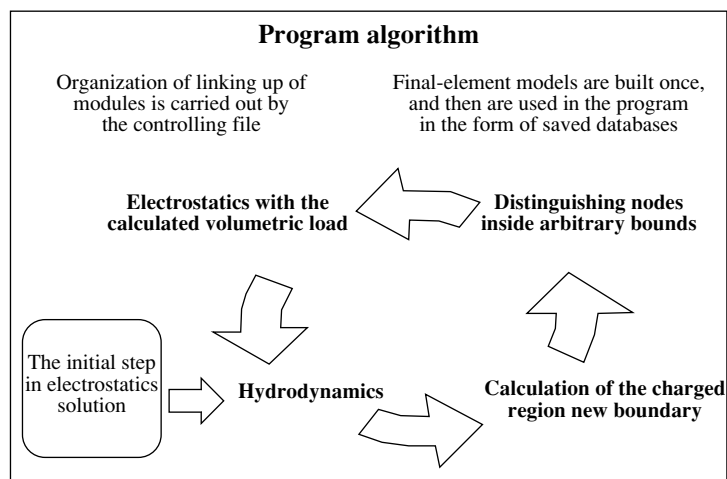


Fig. 2.

field, pressure distribution, and flow lines proper are the results of calculations of the hydrodynamic part of the problem. The shift of the charged area and the shape of the region occupied by space charge are computed at the following step with the aid of a special procedure set written in ANSYS interpreter language.

The forefront of the charged area is defined at the first iteration. The front is a set of points, a curve. An important feature is its width, a dynamic quantity, and possible variations of its form are not limited by anything, making it possible to select a sufficient number of points at the first iteration. The forward boundary movement is calculated as the product of the velocity and iteration time at every point of the forefront. The flow boundary lines could be determined from the following circumstances: the shape of the forefront is known and it is considered that the initial form of the charged ring located round the active electrode remains unchanged.



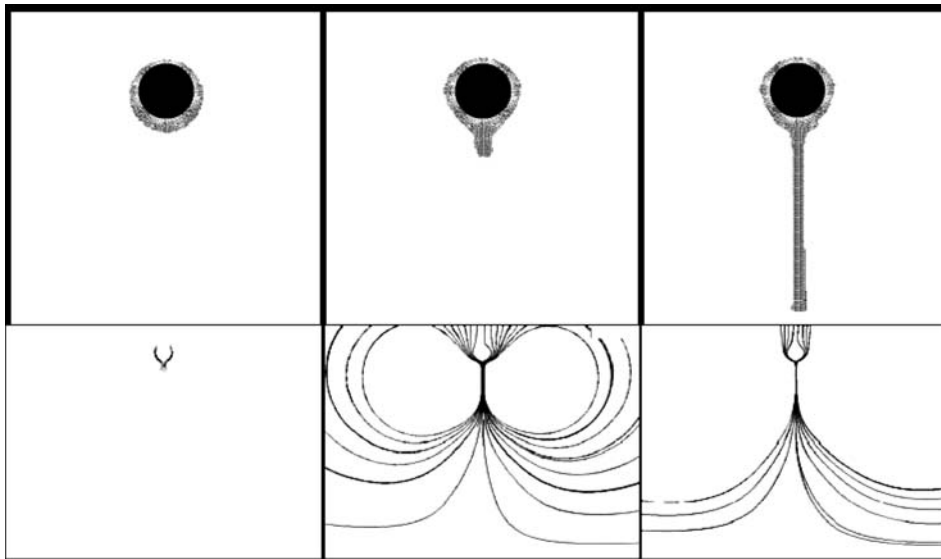


Fig. 3.

At the second iteration, the new distribution of the space charge is carried into the electrostatic problem, and the new electrostatic force density and electric force distribution are calculated at the second iteration, according to which the hydrodynamic problem is solved. Thus, the iterative process is organized. Between the iterations of the problem, the geometry of the external boundary of the charged region is transferred. Such an algorithm allows one to obtain a comparatively high rate of program operation.

The elaborated program permits one to perform numerical study for various initial distributions and qualities of the space charge and voltage. After receiving all input data, it operates automatically during the whole computation time. On completion of every step, there is an automatic recording of the space charge distribution patterns and liquid velocities, permitting control of the solution process.

The universality of the proposed algorithm and its module structure make it possible to modify it without any difficulties in order to calculate other configurations of the electrodes.

The voltage at the electrodes, the amount of density of the space charge, and its initial distribution (the shifted ring geometry around the active electrode and the ring size) are the input data for automatic computation in the program. In the region of interest—the space-charge distribution region—the network is considerably truncated.

RESULTS OF CALCULATION

The calculation initial data are the electrode wire above the plane, two-dimensional case, cell width of 0.09 m, cell height of 0.03 m, wire radius of 0.00035 m, and an interelectrode gap length of 0.01 m. The space

charge initial density is 0.01 C/m, the initial charged area radius is $1.3 \cdot r^*$ (r is the electrode radius), and the applied voltage is 25 kV. Successive stages of the charged streamline forming at time moments of 0.005, 0.055, and 0.090 s after voltage switch-on are presented in Fig. 3. The time lag necessary for the charged ring to form around the active electrode is not taken into account. The flow lines inside the charged thin stream are shown in the lower part of the figure.

The flow is of laminar parallel-jet nature. A significant thickening of the flow lines under the electrode is observed, leading to the propagation of a rather thin charged stream.

At the first step, the liquid flow lines only slightly penetrate into the depths of the interelectrode gap, forming a strong narrowing (reminiscent of a funnel) in the near-electrode region, permitting the charged thin stream to start translative motion. As the charged thin stream moves, the flow lines straighten, forming a section with a parallel-jet flow. The time interval is chosen so small that it is possible to trace in detail the variation of flow lines as the charge moves. As the figure shows, at the final stages, the region of the parallel-jet uniform flow occupies the largest part of the interelectrode gap, the charged thin stream thickness being only a fraction of the charged ring thickness.

Diagrams of pressure distribution along the interelectrode gap are presented in Fig. 4 (on the left of the figure, at the initial time moment; on the right, the change dynamics during subsequent time moments). Under the electrode, a local zone of underpressure forms, followed by a zone of overpressure. This zone is connected to the onset of flow development. It is seen from the right part of the figure that as the charged thin stream moves to the counterelectrode, the overpressure zone shifts to it too. The peak of excess pressure corre-

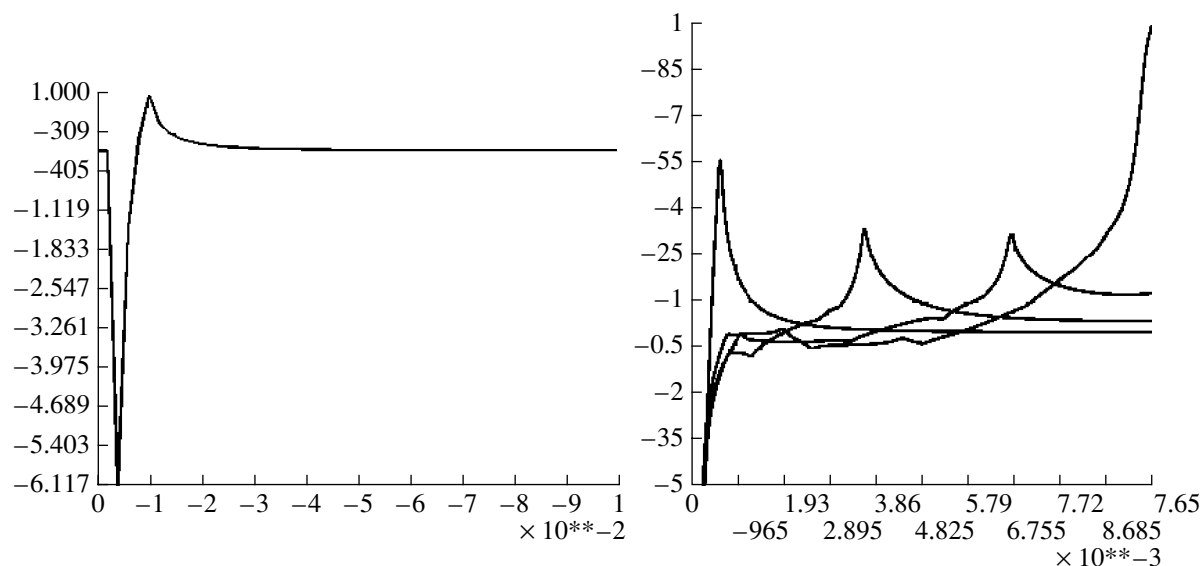


Fig. 4. Pressure distribution near an active electrode (on the left) and propagation dynamics of the overpressure zone (on the right). Pressure magnitude is normalized to the maximum, which occurs at the counterelectrode that charged thin stream approaches. Pressure distributions are presented for the following time moments from the onset of movement: 0.06, 0.085, 0.185, and 0.285 s.

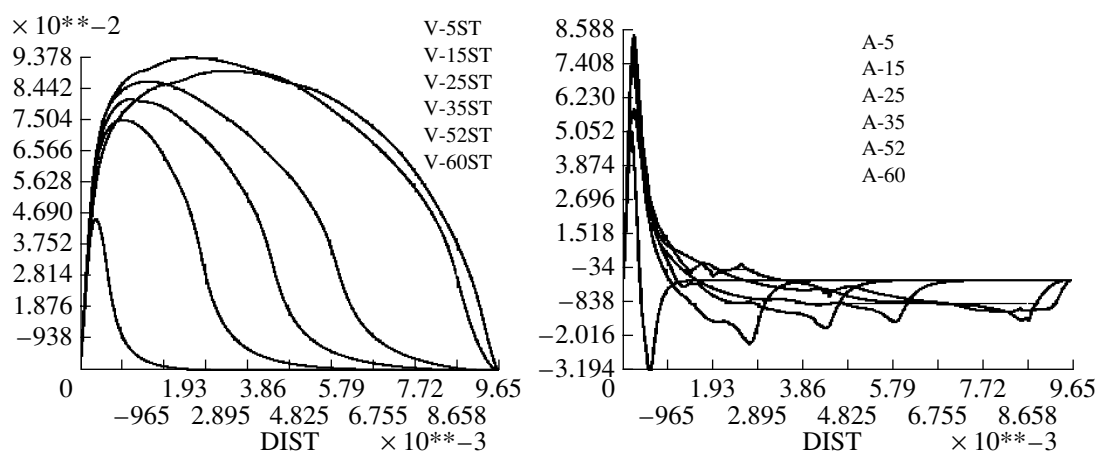


Fig. 5. Distributions of velocities and accelerations along the interelectrode gap at different moments of time.

sponds to the external boundary of the charged thin stream. Under the active electrode, the charged region is funnel-shaped; its front moves deeply into the interelectrode gap and near-electrode structure of flow lines, and the underpressure region remains invariable. The presence of a region of reduced pressure is the cause of thickening of the flow line under the active electrode. The reduced pressure under the active electrode is a kind of “flow pump” and is characteristic for any moment of flow development.

Figure 5 presents the distributions of velocities and accelerations along the interelectrode gap at the center of the charged thin stream for the following time moments from the onset of movement: 0.06, 0.11, 0.16, 0.245, and 0.285 s.

It is seen from the velocity diagram that in the immediate vicinity of the active and passive electrodes, there are thin adhering layers of immobile liquid.

Three flow regions are clearly evident in the diagram of acceleration and velocity. It is possible to identify the intensive acceleration zone, corresponding to the funnel-shaped part of the flow (Fig. 3); a smoothly varied flow zone, corresponding to the charged thin stream parallel-jet part; and a deceleration zone.

At any flow development stage the acceleration zone for the most part retains its structure and is situated in the immediate vicinity of the active electrode in the region of underpressure zone. The deceleration zone, corresponding to the overpressure region (Fig. 4), propagates deep into the interelectrode gap to the counter-

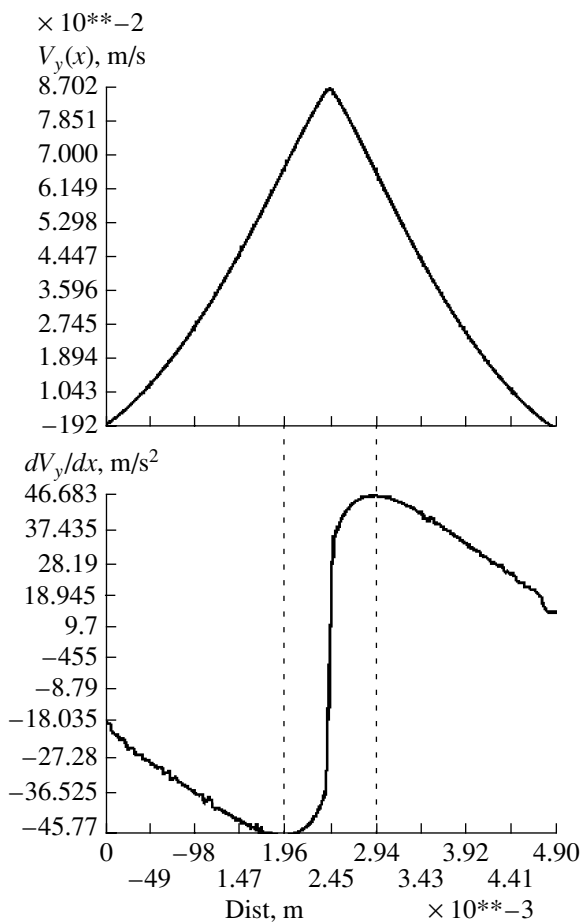


Fig. 6. Velocity longitudinal component and its derivative of the cross coordinate.

electrode and corresponds to the external bound of the charged thin stream. As soon as the charged thin stream reaches the counterelectrode, the flow structure ceases to change. The charged thin stream doubles and propagates along the counterelectrode surface, some distance from it. Here there occurs the charge recombination, arrived from the active electrode with the countercharge, supplied from the plate electrode. So the charged thin stream dimensions in the cross direction are limited. In the calculations they comprise not more than 10% of the interelectrode gap length.

The diagram shows the velocity longitudinal component and its derivative of the cross coordinate. The origin of the coordinates is situated in the middle of the interelectrode gap, some distance to the left of the central jet; the point of transition across zero is in the middle. It is evident that this magnitude exhibits a sharp bend at the boundaries of the charged region. Inside the force effect area, the derivative grows from the center towards the boundary, and outside the charged zone it falls, which corresponds to the transition to the passive part of the central jet, where the flow forms under the action of viscous forces.

CONCLUSIONS

We performed numerical modeling of the establishment of the EHD flow process in the approximation of the state of a frozen-in charge, based on the supposition that at the initial stage of the process a charged ring-type structure forms, from which at later stages there stretches a charged liquid thin stream; and we determined the structure and properties of the EHD flow. The modeling algorithm accounts for the width and form of the charged ring. The velocity contour and vector fields, pressure distributions, flow lines at different stages of flow evolution are obtained as the result of numerical modeling.

The formation of structure EHD flow zone, which was observed many times during the experiments, is described and analyzed.

Under the wire electrode, there is a reduced pressure region, and in front of the charged stream there is a region of increased pressure, which causes the presence of a liquid deceleration zone.

REFERENCES

1. Stishkov, Yu.K., Buyanov, A.V., and Lazarev, A.S., Modeling of EHD flow structure in the asymmetrical system of electrodes, *Sbornik докладov VI Mezhdunarodnoi nauchnoi konferentsii po sovremennym problemam elektrofiziki i gidrodinamike zhidkosti* (Proc. VI Int. Sci. Conf. Modern Problems of Electrophysics and Electrodynamics of Liquids), 2003, p. 259–262.
2. Stishkov, Yu.K. and Ostapenko, A.A., *Elektrohidrodinamicheskie techeniya v zhidkikh dielektrikakh* (Electrohydrodynamic Flows in Liquid Dielectrics), Izd. Lenin. Universiteta, 1989, p. 174.
3. Ostapenko, A.A., Pavlyeno, M.A., and Stishkov, Yu.K., Velocity and Power Fields Electrohydrodynamics Flows, *Annual 1999 Conf. on Electrical Insulation and Dielectric Phenomena*, Austin (USA), 1999, pp. 246–250.
4. Buyanov, A.V., Lazarev, A.S., and Stishkov, Yu.K., EHD Flow Structure Modeling in Wire-Plane Electrode System, *Proc. 5th Int. EHD Workshop*, France, 2004.
5. Buyanov, A.V., Dernovsky, V.L., and Stishkov, Yu.K., Interelectrode Gap Size Influence on EHD Flow Kinematics, *Int. Symp. Electric Insulating Materials, Japan*, 2005.
6. Stishkov, Yu.K., Zhmaev, N.A., and Yarunichev, A.V., Transitional Processes Attendant on Appearance of Electrohydrodynamic Flows in Liquid Dielectrics, *Magn. Gidrodinam.*, 1989, no. 2.
7. Shaposhnikov, A.M., Stishkov, Yu.K., and Pavlenko, M.A., Modeling of Corona Discharge in FEM-LAB, *Sbornik Dokladov VI Mezhdunaradnoi nauchnoi konferentsii po sovremennym problemam elektrofiziki i gidrodinamike zhidkosti* (Proc. VI Int. Scientific Conf. on the Modern Problems of Electrophysics and Electrodynamics of Liquids), 2003, pp. 293–296.

ELECTRICAL PROCESSES
IN ENGINEERING AND CHEMISTRY

Electrophysical Principles of Electrogasdynamic Conversion of Electrical Signals into Pneumatic Ones by Turbulization of Gas Jets by Unipolar Ion Flows

V. S. Nagornyi and I. V. Nagornyi

St. Petersburg State Polytechnical University, St. Petersburg, Russia

Received December 19, 2006

Abstract—Based on modeling and numerical calculations, the electrophysical principles for development of innovative electrogasdynamic electropneumatic converters using turbulization of gas jets by a unipolar ion flow induced in the external area of a corona discharge within narrow interelectrode gaps and with different electrode configurations are formulated.

DOI: 10.3103/S1068375507030076

The overwhelming majority of technical systems of control and information acquisition are physically inhomogeneous, i.e., consist of subsystems and objects having different physical natures (electrical, hydraulic, pneumatic, mechanical). Connection of these subsystems with each other takes place by means of converters of the energy type of signals, as a rule, at present with the use of movable mechanical and electromechanical elements. The presence of movable mechanical and electromechanical elements shifting with friction substantially decreases the operating speed of converters (interface devices) and causes hysteresis, dead belt, and dry friction, which makes the control ambiguous and decreases the reliability of the system.

For qualitative improvement of the characteristics of converters of the energy type of signals, it is necessary first of all to remove the movable mechanical and electromechanical elements from the process of signal conversion [1].

In this paper, we examine the electrophysical principles of the development of fundamentally new methods of direct (without the use of movable mechanics) electrogasdynamic (EGD) conversion of electrical signals into pneumatic signals in electropneumatic systems of control on the basis of hydrodynamic instability and turbulization of jets of working gases by correspondingly organized EGD influences—creation of unipolar flows of ions of one sign or another in sharply inhomogeneous electric fields.

In electropneumatic converters with turbulization of jets by ion flow (EPC TJs), the conversion of an electrical signal into a pneumatic one is realized by an EGD change in the regime of a gas flow—turbulization of a laminar gas jet by a directed flow of ions between electrodes in a sharply inhomogeneous electric field transverse to the jet. Serving as an input electrical signal is the voltage or current between the electrodes, and as an

output pneumatic signal, the change in pressure (expenditure) of a gas in the pickup nozzle of the EPC TJ, which begins to decrease rapidly (at constant supply pressure) with an increase in the voltage on the electrodes due to the decrease in the average kinetic energy of a flow falling into the pickup nozzle on turbulization of a jet by an ion flow.

We estimate qualitatively the order of magnitude of the electrical parameters necessary for realization of EGD control on the assumption that the densities of the electrical and gasdynamic energies should be commensurable:

$$\rho_{e0}E_0l_0 = \rho v_0^2/2. \quad (1)$$

Here l_0 is the characteristic linear dimension (for example, the distance between electrodes); v_0 is the velocity of the gas jet; ρ is the gas density; ρ_{e0} is the volume density of electrical charge in the ion flow; and E_0 is the highest possible value of the electric field at which the spark breakdown of the interelectrode gap does not yet occur (spark breakdown is a nonworking regime of converters).

From (1) we find the necessary value of the volume density of electrical charge that must be introduced into the ion flow for effective EGD control:

$$\rho_{e0} = \rho v_0^2/(2E_0l_0). \quad (2)$$

We choose the value of l_0 taking into account the requirements for minimization of the sizes of EGD devices and the limitation on the value of the voltage on electrodes of converters. Let $l_0 = 10^{-3}$ m, $v_0 = 1$ m/s, and the density of a working gas $\rho \sim 1$ kg/m³. Then it follows from (2) that the necessary volume density of electrical charges in a gas at $E_0 = 10^6$ V/m will be $\rho_{e0} = 5 \times 10^{-4}$ C/m³. In this case, the quantity of ions per 1 m³ of gas is equal to $\rho_{e0}/e = 3 \times 10^{15}$. Here $e = 1.6 \times 10^{-19}$ C

is the charge of an electron. Since approximately 10^{25} molecules are contained in 1 m^3 of a gas under normal conditions, the ratio of charged to neutral molecules (the degree of ionization) is on the order of $10^{-8}\%$. Therefore, for the realization of EGD control, a small degree of ionization of a flow is sufficient.

Such values (of the degree of ionization) can be achieved using x-rays, ultraviolet irradiation, radioactive materials, the nonequilibrium ionization found in a flame, electrokinetic phenomena, or the external area of a corona discharge in gases and its analogue in liquids. It is desirable that the chosen ionization source can provide (if necessary) a uniform distribution of ions in a jet or flow, their sufficiently long lifetime, the possibility of accurate control of available ionization, and work safety for operating staff. This is achieved with the help of a corona discharge in gases [1–4]. An interesting property of a corona discharge is that the processes of formation of electrons and ions as a result of collision ionization of a gas take place only in a narrow corona layer in immediate proximity to the electrode with a large curvature radius, while a unipolar flow of ions of the sign of the corona electrode potential directed to the other electrode is observed in the so-called external area beyond the corona layer of the corona discharge.

Note that, using a corona discharge, the volume densities of charge necessary for EGD control may be created during the development of an EPC TJ. Let the equipment for imparting charge to flows of working medium be presented in the form of concentric metallic spheres of radii r_0, r_1 ($r_0 \ll r_1$) to which the voltage is applied. In this case, Poisson's equation is written in the form

$$2E_r/r + dE_r/dr = \rho_e/(\varepsilon_0\varepsilon), \quad (3)$$

where $\varepsilon_0\varepsilon$ is the absolute dielectric constant of the working medium, ε_0 is the dielectric constant, E_r is the electric field intensity in the space between the spheres, and r is the current radius.

Let us estimate qualitatively the order of the maximum achievable charge density on the external boundary of the corona layer, for which, in the first approximation within the limits of the internal area of the corona, we take $E_r = E_{\max} = \text{const}$. Then we obtain from Eq. (3)

$$\rho_{e\max} = 2\varepsilon_0\varepsilon E_{\max}/r. \quad (4)$$

The maximum value of the electric field intensity will be at the electrode with the minimum radius of curvature, i.e., at the corona electrode in the interior of the corona, where bipolar conductivity takes place. However, we are interested in the flow of unipolar ions in the external area of the corona; hence, in (4), E_{\max} is the intensity on the boundary of the internal zone of the corona. Assuming $r = r_c$, where r_c is the external radius of the corona layer in which collision ionization takes

place, we obtain the expression for the maximum density of unipolar charge

$$\rho_{e\max} = 2\varepsilon_0\varepsilon E_{\max}/r_c. \quad (5)$$

For air, $\varepsilon_0\varepsilon \sim 10^{-11} \text{ F/m}$ and $E_{\max} \sim 10^6 \text{ V/m}$. At $r_c = 10^{-4} - 10^{-3} \text{ m}$, which occurs as a rule in EGD converters, we obtain from (5) that $\rho_{e\max} \sim 10^{-1} - 10^{-2} \text{ C/m}^3$, at which the realization of EGD control by gas flows is possible.

In a number of cases, the thickness of the corona layer may be neglected and it can be assumed in expression (5) in the first approximation that $r_c \approx r_0$. Then

$$\rho_{e\max} \approx 2\varepsilon_0\varepsilon E_{\max}/r_0. \quad (6)$$

Thus, to increase the efficiency of EGD converters with the use of a corona discharge taking into account expression (6), it is necessary to choose the smallest possible bending radius of a corona electrode.

The charge densities obtained in this way correspond to ρ_{e0} found from condition (1) for the commensurability of gasdynamic and electrical forces, and these densities are sufficient for control by EGD converters.

The values of both the force created under EGD control and the output gasdynamic power of an EPC TJ are limited and depend on the nondimensional parameter of the EGD interaction N introduced into the consideration on the basis of (1), which is the ratio of the volume densities of the electrical and gasdynamic energies:

$$N = \frac{\rho_{e0}E_0l_0}{\rho v_0^2}. \quad (6a)$$

In mathematical models of EGD converters, with a change in the regimes of flow of fluxes, this parameter enters the right part of an equation of the type of the Navier–Stokes equation. The range of change in the EGD interaction parameter (6a) for specific types of converters depends on the electrophysical parameters of working media (the dielectric constant, mobility of ions of one or the other sign, and diffusion coefficient of ions), the chosen characteristic linear dimension l_0 , and the working range of electric field intensities E_0 between the electrodes in dependence on their configuration.

The application of sharply inhomogeneous strong electric fields (of the corona discharge) in the realization of an EPC TJ allows the processes of imparting a unipolar charge ρ_e to the gas and creating a controlling volume force $F = \rho_e E$ to be combined in time; this simplifies the construction and electrical scheme of an electropneumatic converter. Here E is the average electric field intensity applied to the flow of working medium (the field in the external area of the corona).

Let us estimate the limiting values of pressure and temperature of the environment at which the capacity for work of an EPC TJ with a controlling unipolar ion

flow created with the help of a corona discharge in air is retained.

Within the framework of the Townsend–Rogovskii theory, accepted at present, the number of collisions carried out by electrons in a corona layer per unit path along the electric field force lines is characterized by the coefficient of collision ionization by electrons α_e , determined by the product of the mean number of collisions per unit length and the probability of ionization by electron impact on collision. In this case, the condition $w_e > w_i$ should be fulfilled, where w_i is the ionization energy of working gases and w_e is the energy of electrons.

In electronegative gases and their mixtures, such as an air, atoms and molecules may attach an excess electron, forming a stable negative ion. Therefore,

$$\alpha_{ef} = \alpha_e - \alpha_a, \quad (7)$$

where α_{ef} is the effective coefficient of collision ionization by electrons, determining the process of multiplication of electrons on collision ionization, and α_a is the coefficient characterizing the process of electron attachment. At $\alpha_{ef} > 0$, collision ionization begins. In this case, in an EPC TJ, the normal regime of functioning, connected with the fulfillment of the condition of collision ionization and the obtaining of a stable flow of ions in the external area of the corona, is determined by the relationship

$$E/p \geq c, \quad (8)$$

where c is a constant value for the chosen working gas. For air, $c = 23.8\text{--}26.3$ V/(m Pa) [2].

At bending radii of needle-shaped electrodes of the order of 10^{-5} m, the electric field intensity in the corona layer is $(3\text{--}5) \times 10^7$ V/m. Hence, it follows from (8) that the ranges of pressures of the environment in which an EPC TJ can work are relatively large and provide for normal functioning of converters at not only atmospheric but also increased pressures of the environment.

Let us determine the conditions providing for the applicability of the EGD method and control by gas flows on a change in its temperature. Effective coefficient of collision ionization (7) is a function of the electric field intensity E in the corona layer and the pressure p of the environment. For the majority of gases near the threshold value, in the first approximation, we can write [2, 3]

$$\alpha_{ef} = \frac{aT_0}{\rho_0 p_0 T} \left(E - c \frac{\rho_0 p_0 T}{T_0} \right)^2, \quad (9)$$

where the coefficient a together with the power index determines the rate of increase in α_{ef}/p with an increase in E/p after the threshold value and ρ_0 is the relative density of the gas.

For the collision ionization by electrons to begin, it is necessary that the coefficient of collision ionization become more than zero. Assuming $\alpha_{ef} \approx 0$, taking into

account that $aT_0/(r_0 p_0 T) \neq 0$, we obtain from (9) the condition of application of EGD control on a change in temperature of the environment:

$$ET_0/(\rho_0 p_0 T) \geq c. \quad (10)$$

It follows from (8) and (10) that the method of EGD conversion of the type of energy of signals used for construction of an EPC TJ is applicable to a wide range of pressure and temperature of the environment. For example, for converters working on air, at $E \approx 10^7$ V/m, $T_0 = 293$ K, $\rho_0 = 1$ kg/m³, $p_0 = 101.3$ kPa, and $c = 23.8$ V/(m Pa), from (10) it can be concluded that the temperature of air may change by up to several thousand degrees Kelvin. In this case, it is necessary to take into account the thermoautoelectronic emission [2]. However, EGD converters, like traditional ones, require known methods of compensation of an adverse influence of the temperature of the environment on their characteristics to be applied.

To obtain not only impulse but also potential signals at the output of an EPC TJ without their complication, first of all, the flow of unipolar ions over the period of existence of electrical signals at the input of the converter should be provided. This is realized on fulfillment of the condition of independence of the corona discharge, under which no additional external ionizer is required for its maintenance. This condition is written analytically in the form [2, 3]

$$\int_0^{l_c} \alpha_{ef} dx = K \equiv \text{const}, \quad (11)$$

where l_c is the length of a force line of the field within the bounds of the corona layer and x is the path of the electron avalanche (from the cathode in the case of a negative corona and from the external boundary of the corona to the anode in the case of a positive corona). In this case, the values of K in (11) for different signs of a corona electrode may differ by two to three times [2]: for a positive potential (a positive corona), $K \approx 18\text{--}20$, while, for a negative corona, $K = \ln[(1 + \gamma)/\gamma] = 8\text{--}9.2$. Here γ is the generalized coefficient of secondary ionization, characterizing the number of electrons formed on average in a corona layer either in the process of ionization by secondary electrons (secondary ionization) released from the cathode on impact on the surface of positive ions of the initial avalanche, or due to photoionization on the cathode surface by radiation from the initial avalanche, or due to photoionization in the volume of the gas by shortwave radiation of the avalanche.

When condition (11) is fulfilled in an EPC TJ, a stable flow of ions in the external area of the corona discharge arises, to which the determined values of the electric field intensity near the needle-shaped electrode and the voltage on electrodes correspond, which are referred to as the initial electric field intensity E_c and initial voltage U_c of corona initiation.

Synthesis of EPC TJs presumes first of all knowledge of the working range of changes in voltages on converter electrodes and its dependence on the construction parameters and the parameters of the working medium. This follows from the physical peculiarities of the work of EGD converters, the characteristic feature of which is the restriction of the voltage U on electrodes on the upper level by the voltage of spark breakdown U_{br} of the interelectrode gap. The lower, nonzero level of U_c determines the origin of EGD phenomena (the creation of a stable unipolar flow of ions on fulfillment of (11)), placed at the basis of EPC TJ construction. Therefore, U_c influences the static and dynamic characteristics determining the moment of the beginning of a change in the output signal. In turn, knowing the range of change in the voltage on the electrodes, one can with justification formulate the requirements for the design of high-voltage amplifiers constituent in the structure of an EPC TJ.

Thus, the working range of the voltage U on the electrodes of an EPC TJ changes within the bounds

$$U_c \leq U < U_{br} \quad (12)$$

where U_c is the initial voltage of the corona discharge in a working gas and U_{br} is the voltage of spark breakdown of the interelectrode gap.

To soften the requirements on the electrical part of an EPC TJ, it is desirable to choose the maximum possible voltage range (12). Optimal is such an EPC TJ in which construction and other parameters provide for a minimum value of the voltage U_c of corona initiation and a maximum voltage for the spark breakdown U_{br} .

The possible range of change in voltages on the electrodes of the EPC TJ may be expanded first of all due to design solutions with the corresponding choice of polarity of a corona electrode.

The substantial difference in the values of the right part of expression (11) for positive and negative coronas influences insignificantly the value of E_c [2]. For a negative corona, this value is less than for a positive one [2]. Correspondingly, the value of U_c for a negative corona will be less than for a positive one.

Since, at a positive potential of a needle-shaped electrode, the bandwidth of high voltages is larger [2] than at a negative potential, with an increase in the voltage on electrodes of EGD converters, the development of streamers at a negative potential of a needle will take place to a smaller length of the interelectrode gap. This leads to the fact that, in the case of a positive corona, the spark breakdown arises at a lower voltage U_{br} on the electrodes than in the case of a negative corona. In view of the fact that the voltages U_c of initiation of positive and negative coronas in the first approximation are the same, a conclusion about the narrower working range (12) of the voltage of a positive corona can be drawn.

By the choice of construction parameters of EGD converters (first of all, the bending radius r_0 of a needle-

shaped electrode), the working range of voltages can be substantially changed.

The value of U_{br} decreases faster than U_c with a decrease in the distance h between the electrodes, which leads to a decrease in working range (12). Hence, with a further decrease in h , beginning from some critical distance h_0 between the electrodes, a corona does not appear, but a spark breakdown takes place immediately; i.e., the working range of voltages U equals zero. Therefore, in EGD converters, the ratio h/r_0 should be greater than the determined value $h/r_0 > h_0/r_0$. For example, for coaxial electrodes, the relationship of radii at which a corona discharge in air is formed should satisfy the condition [6] $R/r_0 = (h + r_0)/r_0 > 2.718$.

With an increase in the pressure p of the environment, operating voltage range (12) on electrodes of the EPC TJ at the defined geometrical sizes of the interelectrode gap increases. This is explained by the fact that the value U_{br} increases faster than U_c with an increase in p .

The dynamics of the initiation of a corona discharge in an EPC TJ, as in the other known cases (high-voltage devices [3]), is determined by the statistical discharge delay time t_s on reaching U_c (characterizing the moment of appearance of a free electron capable of beginning collision ionization) and the time t_f of formation of a corona discharge. Since, in an EPC TJ, there are small distances between electrodes, then $t_f \ll t_s$ and the time of corona discharge initiation $t_d = t_s + t_f \approx t_s$. In this case, t_d does not exceed several microseconds. Hence, it can be neglected in an analysis of the dynamics of an EPC TJ.

In the case of control by turbulization of a submerged gas jet, in a number of cases, the free passage through the other electrode of a gas flow caused by the motion of ions from the needle electrode should be considered. Physically this is realized by the choice of the other electrode in the form of a metallic plane with a hole that is fixed in a dielectric frame in such a way that the distance from the needle end to the metallic plane is substantially (five to seven times) less than that to the dielectric walls of the frame. To eliminate the influence of surface charges adsorbing on the dielectric during the work of such an EGD converter, the dielectric walls in electropneumatic converters should stand relatively far from the needle-shaped electrode.

In the other case, to eliminate the adsorption of a charge on the walls of the frame and decrease the dimensions, it is expedient to fabricate the internal walls of the frame together with the metallic nozzle. Thus, the side walls have the ground potential. To eliminate the initiation of a corona discharge from the needle to the side walls, it is necessary that the frame radius also be larger than the distance from the needle to the nozzle, but already not by 5–7 times, as in the variant with dielectric walls, but by not more than 1.5–2 times. In this case, the maximum output pressure in a nozzle of such an elementary step amounts to 60–70 Pa. This is two times less than in the case of “open” electrodes;

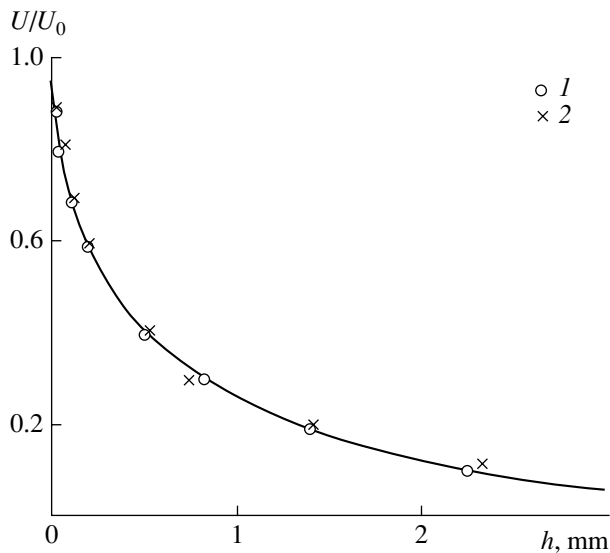


Fig. 1. Influence of the hole diameter in a plane electrode on the distribution of a potential in the needle-plane with hole interelectrode gap in volumes of gas bounded by dielectric solid walls at $r_0 = 0.05$ mm: d_0 , mm: (1) 1; (2) 4.

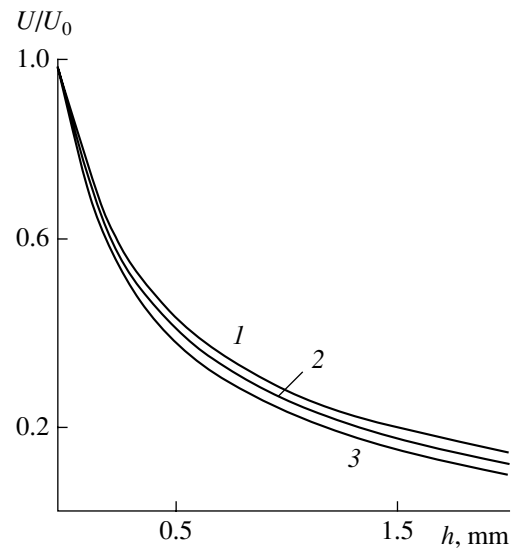


Fig. 2. Results of modeling in an electrolytic bath of the influence of an end hole in a metallic frame on the potential distribution in the vicinity of a needle in electrode systems of EGD converters: d_n , mm: (1) 8; (2) 1.4; (3) 0.8.

however, in comparison to the previous variant, this device is considerably more compact and differs by a high stability of characteristics, owing to the fact that the influence of the field of surface charges on the walls of the frame is completely eliminated in it.

First of all, we analyze the influence of the hole in a plane electrode on the distribution of a field in the vicinity of a needle-shaped electrode. For this, the approach of analogue modeling of electrostatic fields of real electrode systems in an electrolytic bath developed by Demirchyan [5] is used, which allows modeling of any complex boundary contour of an area (including a hole) on the basis of the expression for the Laplace operator and is simple in realization. This method completely excludes the idealization of a real electrode system, ensuring the geometrical similarity of the needle and plane electrodes and boundary conditions, as well as a high accuracy (several tens of percent), in the case of careful implementation of the model and good experience. Figure 1 presents, as an example, the typical dependence obtained in such a way of U/U_0 , characterizing the field distribution along the symmetry axis, on the hole diameter d_0 in the plane electrode, where U_0 is the potential in the vicinity of the needle electrode and U is the current potential.

Therefore, for calculation of the initial voltage U_c of initiation of a corona discharge in a system of electrodes with dielectric solid walls relatively far from the needle electrode, the general calculation model typical for electrodes of the needle-plane (without a hole) type may be applied.

The results of analogue modeling in an electrolytic bath of fields of real electrode systems of an EPC TJ in a metallic frame also showed that the presence of an end hole in the metallic frame located on the axis of a needle electrode practically does not influence the distribution of potential and electric field intensity in the vicinity of the needle end. In Fig. 2, typical dependences of the field distribution on the diameter of a nozzle hole d_n in the end of a metallic frame are presented. Hence, for calculation of U_c on the electrodes of an EPC TJ in the case of such an organization of unipolar ion flux motion, it is possible, as in the case of the location of electrodes of the needle-plane type in a dielectric frame, to aim at a unified calculation model without taking into account the hole coaxial to the needle in the end of the metallic frame.

To refine the electric field distribution for small interelectrode distances (up to 5–6 mm) and changes in the bending radius of a needle electrode r_0 from 0.5×10^{-2} to 9.0×10^{-2} mm (which occurs in EPC TJs), calculations of the electric fields between electrodes of the needle-plane type were performed up to the moment of corona discharge initiation by numerical solution of Laplace's equation using the method of nonuniform meshes and equivalent charges [4]. The conducted investigations showed [6], that, in this case, practically over the entire interelectrode gap, there is a nonuniform electric field with a sharp strengthening in the vicinity of the electrode with a small radius of curvature r_0 .

Moreover, the interior of the corona discharge x_c (where the effective ionization coefficient $\alpha_{ef} > 0$; see expressions (7), (11)) becomes comparable with the distance between the electrodes. This confirms the

expressions obtained in the first approximation for the thickness x_c of the internal area of a corona found from the condition of equality to zero of effective ionization coefficient (11) on the external boundary of the corona layer using the Lamé method for different approximations of real electrode systems of EPC TJs by coaxial hyperboloids of revolution (in the case of placement of electrodes in a dielectric frame) and coaxial ellipsoids of revolution (for placement of electrodes in a metallic frame).

In the case of approximation of the electrode system of an EPC TJ by coaxial hyperboloids of revolution analogously to [7] we have

$$x_c = \left[(h_0^2 - r_0 h_0) + \frac{2U \sqrt{h_0^2 - r_0 h_0}}{c' \rho_0 \ln \frac{(h_0 + \sqrt{h_0^2 - r_0 h_0})(h_2 - \sqrt{h_0^2 - r_0 h_0})}{(h_0 - \sqrt{h_0^2 - r_0 h_0})(h_2 + \sqrt{h_0^2 - r_0 h_0})}} \right]^{0.5} - h_0, \quad (14)$$

where $h = h_2 - h_0$ is the distance between the electrodes, h_0 is the coordinate of the end of a needle electrode with bending radius r_0 , and h_2 is the coordinate of an electrode of the type of a plane.

In this case, the second semiaxis of the internal ellipsoid approximating the thickness of the needle is found through the radius of curvature r_0 of a vertex of the ellipsoid in such a way that it corresponds to the radius of curvature of the needle electrode $b_1 = \sqrt{r_0 h_0}$, while the origin of coordinates up to the focus of the ellipsoid is determined as $a_1 = \sqrt{h_0^2 - r_0 h_0}$.

Equations (13) and (14) are fulfilled at a voltage on the electrodes equal to the initial voltage of corona discharge initiation in the interelectrode gap.

Calculations according to (13) and (14) for the above-indicated ranges of change in r_0 and h show that the thickness of the internal area of the corona becomes comparable with the distance between the electrodes of the EPC TJ.

Thus, the typical electrophysical specific feature of functioning of electropneumatic converters with turbulization of a jet by a unipolar ion flow in the external area of a corona discharge is the commensurability of the external and internal areas of a corona at small distances between the electrodes of an EPC TJ. In this case, the electric field is nonuniform over the entire interelectrode gap of the EPC TJ.

Hence, for determination of the initial voltage U_c on the electrodes of an EPC TJ in expression (12) according to the initial electric field intensities of a corona E_c , the known expressions for E_c (the formulas of Peak, Townsend, Lesch, Aleksandrov, Engel' and Shtenbek, etc. [2–4]) are unacceptable since they do not take into

$$x_c = h - \left[(h^2 + r_0 h) - \frac{2U \sqrt{h^2 + r_0 h}}{c' \rho_0 \ln \frac{\sqrt{h^2 + r_0 h} + h}{\sqrt{h^2 + r_0 h} - h}} \right]^{0.5}, \quad (13)$$

where h is the distance between the electrodes and $c' = c\rho_0$. Under normal atmospheric conditions for air [3] $c' = 24.11 \times 10^3$ V/cm.

In the case where the calculation model of the electrode system is presented in the form of coaxial ellipsoids of revolution, it is easy to obtain [6]

account these factors and give large deviations from the results of experiments [6]. To determine the working range of the change in voltage on the electrodes (12) and calculate the static and dynamic characteristics of the EPC TJ, a more exact formula for E_c [6, 7] is used that takes into account the dependence of E_c on the distance h between electrodes at small interelectrode gaps:

$$E_c = A\rho_0 + B\sqrt{h\rho_0/r_0}, \quad (15)$$

where $A = cp_0 T/T_0$; $B = \sqrt{Kp_0 T/(adT_0)}$; the coefficients a and c are found from (9) near the threshold value $(E/p)_a$; K is determined from condition (11) of independence of the corona discharge in the working gas; and d is the empirical coefficient characterizing the distance from the electrode with a small radius of curvature r_0 within the bounds of which up to the moment of initiation of a corona discharge the electric field near the threshold value E/p has pronounced inhomogeneity along the length of the interelectrode gap (maximum gain constant).

Thus, as a result of the studies performed:

(1) the electrophysical principles of development of new methods of EGD conversion of electrical signals into pneumatic ones for physically nonuniform systems of control on the basis of hydrodynamic instability and turbulization of gas jets by creation of a unipolar flow of ions in the external zone of a corona discharge in the case of small interelectrode gaps and different characteristic configurations of electrodes have been formulated;

(2) the electrophysical mechanisms of interconnection of the work of EPC TJs in static and dynamic regimes and their influence on the working range of

voltage change on the electrodes of an EPC TJ have been generalized;

(3) the results of modeling and numerical calculation of distributions of sharply nonuniform electric fields in electrode systems of the needle–plane type bounded by solid walls (both dielectric and metallic) at small interelectrode gaps occurring in EPC TJs have been presented;

(4) on the basis of these results, a new formula for determining the initial electric field intensity of corona initiation has been proposed that takes into account more completely the electrophysical mechanisms of obtaining unipolar ion flows in small interelectrode gaps; calculations according to the proposed formula are in good agreement with experimental data [6];

(5) the conditions of obtaining a stable flow of unipolar ions in working gases (air) in a sharply nonuniform electric field for small interelectrode gaps of different configuration occurring in electropneumatic converters with turbulization of jet by a flow of unipolar ions have been formulated.

ACKNOWLEDGMENTS

This work was supported by the Russian Foundation for Basic Research, project no. 06-08-01234-a.

REFERENCES

1. Nagornyi, V.S. and Denisov, A.A., *Ustroistva avtomatiki gidro- i pnevmosistem* (Automatic Devices of Hydro- and Pneumosystems), Moscow: Vysshaya Shkola, 1991.
2. Raizer, Yu.P., *Fizika gazovogo razryada* (Physics of Gas Discharge), Moscow: Nauka, 1992.
3. *Tekhnika vysokikh napryazhenii* (High-Voltage Technique) Razevig, D.V., Ed., Moscow: Energiya, 1976.
4. Vereshchagin, I.P., Levitov, V.I., Mirzabekyan, G.Z., and Pashin, M.M., *Osnovy elektrogazodinamiki dispersnykh sistem* (Basics of Electric Gas Dynamics of Disperse Systems), Moscow: Energiya, 1974.
5. Demirchyan, K.S., *Modelirovanie magnitnykh polei* (Simulation of Magnetic Fields), Leningrad: Energiya, 1974.
6. Nagornyi, V.S., Initial Electric Field Intensity of Corona Discharge Initiation at Small Interelectrode Distances, *Elektrichestvo*, 2004, no. 12, pp. 8–11.
7. Nagornyi, V.S., Studies of Processes of Transfer of an Electrical Charge to Drops of Dielectric Liquids in a Sharply Inhomogeneous Electric Field of a Corona Discharge, *Elektron. Obrab. Mater.*, 2006, no. 2, pp. 13–19.

**ELECTRICAL PROCESSES
IN ENGINEERING AND CHEMISTRY**

Oxide Films on Iron Surface and Their Physicochemical Characteristics

A. I. Kostrzhitskii, T. V. Cheban, and R. A. Podolyan

Odessa National Academy of Food Technologies, ul. Kanatnaya 112, Odessa, 65039 Ukraine

Received November 8, 2006

Abstract—The regularities of electrochemical corrosion behavior of oxides of iron ionic plasma coatings on steel in neutral media are considered. Quantitative data on the influence on the kinetics of electrode potentials and potentiodynamics of polarization curves are given. Recommendations on the possibility of using ionic plasma coatings for protection of dilute steels from corrosion are proposed.

DOI: 10.3103/S1068375507030088

The passive state of iron and alloys based on it is due to formation of oxide layers, as a rule. Electrochemical corrosion characteristics of oxidized samples are determined by a number of factors; some of them are directly related to structure, thickness, and phase composition of oxides. In review [11], the results of theoretical and experimental investigations of domestic and foreign authors regarding various aspects of the passive state of ferrous systems are generalized. In the overwhelming majority of cases, the iron state is related to the presence on the surface of oxide modification of the α - Fe_2O_3 type; its shielding properties do not depend on the mode of formation (natural oxidation of iron in air, thermal method of oxide growth, chemical method, etc.). From the viewpoint of passive state stability, one can mention its dependence on the composition of an aggressive medium, especially on the presence of chlorine ions. Thus, experimental data on the influence of chlorine ions, temperature of the solution, its concentration, and flow velocity on the passive state of low-alloy steels are related to the multilayer structure of oxides, the oxide inner layer directly adjoining the base metal surface being responsible for the passive state. In the inner layer, significant electric fields are produced, the intensity in them achieving 10^6 V/cm; they are the cause of the passive state of oxidized iron.

Thus, layers of oxides naturally or artificially formed on the surface of iron and low-alloy steels possess good shielding properties; they are characterized by the passive state in some aggressive media; the best shielding properties are shown by oxides having a thickness of about 20–30 nm, according to the data of foreign researchers.

In development of the basic propositions of [1] on formation and properties of protective films on an iron surface, a new, rather effective method for formation of surface oxide layers on an iron surface was applied, i.e., treatment of the surface in a glow discharge in an atmosphere of residual gases under pressures of about 0.1–

0.4 Pa. For the first time, a similar method was used by the authors of monograph [2] as a mode of steel surface preparation before vacuum coating deposition. Later investigations [7, 9, 10] showed the possibility of applying a glow discharge as a method for surface oxide layer formation for improvement of adhesion of condensation coatings obtained by methods of vacuum technology.

In our investigations, an abnormal glow discharge was used in a residual atmosphere of air under pressures most often used for vacuum metallization [2–4]. A significant distinctive property of the abnormal glow discharge is an increase in the cathode potential fall with increasing applied external voltage. The cathode potential fall determines the energy of ions coming to the cathode and, therefore, it influences the intensity of the cathode surface bombardment. It is precisely the ion bombardment intensity on which the mode of passive layer formation on a low-alloy steel surface depends. According to the data of preliminary investigations, the basic parameters of a glow discharge determining the character of passive layer formation may be considered the following: current type (direct or alternating), voltage value, discharge current density, pressure in vacuum chamber, form and material of electrodes and surface under treatment, composition of residual atmosphere, and treatment time. In our investigations, three basic parameters were variable: voltage on electrodes U , discharge current density j , and treatment time τ . The other parameters were maintained constant. As was mentioned in [2, 4], precisely these parameters of preliminary preparation of the surface of metallized products are governing for obtaining qualitative adhesion of coatings and substrates.

Brief Characteristic of Each Studied Parameter

In the abnormal glow discharge region, the increase in voltage on electrodes leads to an increase in energy

of the ions bombarding the surface. It should be expected that the surface treatment efficiency would depend on the value of the applied external voltage. However, as was noted by the authors of [2], the influence of accelerating voltage on the character of the processes taking place on the surface must be studied in combination with some other parameters, in particular, the discharge current density. Thus, at high current densities, the voltage change weakly influences the efficiency of surface purification. At low densities, the voltage increase leads to the purification effect increasing. The authors of [2] also note a fairly wide range of values of the accelerating voltage applied in engineering processes of substrate surface purification before deposition of condensation coatings. Choice of the accelerating voltage value is not substantiated, as a rule. This gap is to some extent eliminated in [4, 5], however, only for the processes of ion treatment of the surface. As to the influence of the accelerating voltage value on the character of oxide layer formation, it is still an open question.

Analogous considerations are justified for the discharge current density too. For practical use, one needs to know only critical values of j at which destruction of the surface of the sample under treatment occurs [4].

Choice of the surface treatment time is determined, as a rule, by the goals of researchers, degree of substrate contamination, values of accelerating voltage and current density, etc. It is obvious that the maximum possible reduction of the surface treatment duration with achievement of a desirable effect is positive from the viewpoint of economic indices of the process. Moreover, prolonged treatment may result in repeated contamination caused by sputtering of the glow discharge electrodes. An unfounded increase in accelerating voltage and current density leads to the same effect. In this connection, one of the goals of the present study was a choice of optimal ratios of U , j , and τ at which the expected effect, i.e., the best shielding properties of oxide layers, will be maximal.

EXPERIMENTAL

Investigations on artificial growth of oxide layers were carried out in a laboratory vacuum installation assembled on the basis of a VN-2MG[Russian] mechanical pump. The high-voltage source was an HOM-10 high-voltage transformer; the voltage on the electrodes was varied in the range of 0.4–2.0 kV. A needle leak valve provided a stable admission of air in the processes of surface treatment and oxide layer growth. The vacuum in the chamber was measured and controlled by a VIT[Russian]-3 vacuum gage. In the process of discharge combustion in the chamber, the voltage on the electrodes and the current in the secondary winding were recorded. According to the known area of the sample, the discharge current density was calculated. The discharge electrodes were made of alumi-

num, providing a lower rate of sputtering in comparison with the materials under study.

Special attention was paid to the relative position of the electrodes and the sample under treatment. It is well known [4, 5] that nonconducting materials (glass, ceramics, plastics, etc.) are placed in the cathode dark space of the glow discharge, and metal samples are placed on the electrodes, as a rule. This gives technological and structural advantages: electrode form is simplified, and application of additional sample holders is not necessary. The second electrode was placed symmetrically to the surface under treatment to obtain the maximum possible uniformity of the electric field. For selection of optimal modes of oxide layer growth, the methods of planning the experiment and statistical treatment of observational data were applied that had been used earlier for studying regularities of formation of multicomponent vacuum coatings [4]. In our case, the experiments were carried out according to the matrix of a three-factor experiment with variation of factors on two levels; the planning matrix is given in Table 1, which also contains basic data on regularities of oxide film formation on the surface of ST3 steel samples.

RESULTS AND DISCUSSION

Depending on the goals of the experiment, the lower level of factor variation corresponded to the following values: 600, 800, and 1000 V for U ; 1.7 and 2.5–2.7 mA/cm² for j ; 5 and 10 min for τ . The upper level of variation corresponded to the following values: 1000 and 1500 V for U ; 3.8–4.0 and 6.2 mA/cm² for j ; 15 and 20 min for τ . The pressure in the chamber was maintained constant at a level of 0.2–0.4 Pa of the order of 5×10^{-2} mm Hg. After the process was completed, the samples were kept in the chamber for 1.0–1.5 h to prevent them from additional oxidation in air after the chamber was opened.

The phase composition and thickness of the oxide layers were studied by the method of electron diffraction for reflection geometry (layers of about 50 nm were probed); the survey was carried out at accelerating voltages of 100 kV. The film thickness (its change in the growth process) was determined by the ellipsometry method at two incidence angles $\varphi = 60^\circ$ and 70° of polarized light, $\lambda = 546.1$ nm. Calculation of the ellipsometric data was performed by computer.

It is known that an oxide of the γ -Fe₂O₃ type has a structure similar to Fe₃O₄ magnetite; it appears, as a rule, in late stages of iron oxidation at room temperature, when the oxide growth rate is high, and during Fe₃O₄ oxidation in conditions free of water at a temperature of 187–370°C. The optical constants of the steel surfaces after impact of the glow discharge corresponded to the detected phase oxide, achieving a thickness of 20 nm. As the film grew further, the indices of refraction n and absorption k changed and corre-

Table 1. Matrix of three-factor experiment with factor variation on two levels

Experiment no.	Modes of treatment in discharge			Change in oxide film thickness ΔL , nm	Total thickness of oxide after treatment, nm	
	Accelerating voltage U , V	Discharge current density j , mA/cm ²	Treatment time τ , min		Total thickness of oxide after treatment, nm	Composition of 50-nm-thick layer
1	600	1.7	10	6.0	11.0	α -Fe + γ -Fe ₂ O ₃
2	600	1.7	20	8.0	13.0	γ -Fe ₂ O ₃
3	600	2.5	10	4.0	12.0	γ -Fe ₂ O ₃
4	600	2.5	20	15.5	22.0	γ -Fe ₂ O ₃
5	1000	1.7	10	11.4	16.6	γ -Fe ₂ O ₃
6	1000	1.7	20	9.6	16.8	γ -Fe ₂ O ₃
7	1000	2.5	10	15.5	20.0	γ -Fe ₂ O ₃
8	1000	2.5	20	115.0	120.0	γ -Fe ₂ O ₃

sponded to an oxide with higher absorption than magnetite. It is apparent that, in our case, the oxide film is two-layer and it contains hematite in its inner layer, and γ -Fe₂O₃ prevails in its external layers. Such a structure of the oxide film differs from the known thermodynamically more probable layer position under thermal oxidation of steel [6, 7], when a magnetite layer must be located under a hematite layer. This peculiarity in formation of the oxide layer structure in our experiments is apparently connected with the peculiarities of steel oxidation under ion bombardment. These conditions are far from equilibrium and are characterized by low pressure of oxygen and facilitation of diffusion processes, in particular, diffusion of iron ions in a growing film.

Thus, using the data of ellipsometric studies and phase analysis, one can state that the main component of oxide films of a thickness up to 50 nm formed in the plasma of an alternating current glow discharge is a compound of the γ -Fe₂O₃ type.

Table 2. Electrode potentials of steel samples treated in discharge

Experiment no.	Values of electrode potentials of steel samples measured in mV by chlorine–silver reference electrode after			
	0 min	30 min	60 min	96 h
1	–70	–120	–150	–200
2	+50	–95	–100	–245
3	–115	–190	–155	–210
4	+30	–100	–120	–270
5	–85	+90	+65	+120
6	+30	–210	–270	–280
7	+180	–85	–125	–130
8	+130	–55	–95	–270

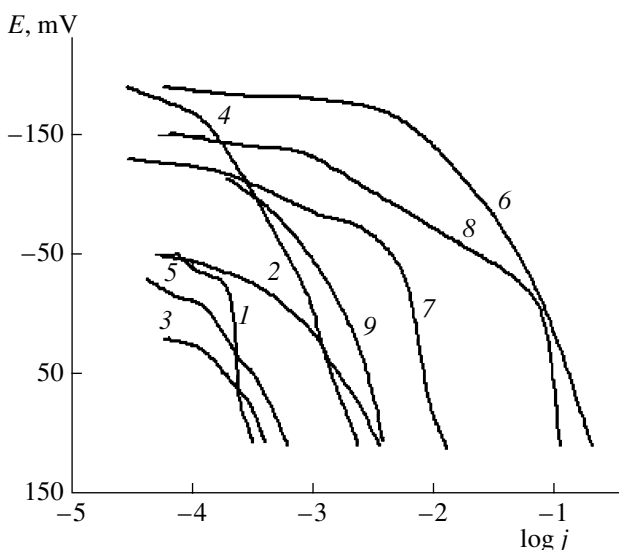
Studies of kinetics of electrode potentials and potentiodynamic polarization curves allow the following generalizations (Table 2). Values of the electrode potentials at the moment of immersion do not allow us to draw even a preliminary conclusion on the passive state of the steel surface. More positive values of the electrode potentials are fixed in the samples treated at higher accelerating voltages (the experiment numbers in Tables 1 and 2 are identical). However, upon further holding of the samples in the medium, the influence of U on values of the electrode potentials of the samples is weakly expressed. According to the kinetic curves, it was found that, at the initial moments of time (10–20 min), a shift of the values of the potentials to the negative region is observed in all the samples, and upon further holding, a shift of the potentials to the negative region is found in samples 3 and 5. This fact is related to a possible formation of surface films. An analogous shift of the potentials to the positive region in the samples treated by mode 2 is difficult to explain, since in 240 h of testing its appearance testifies to the occurrence of intense corrosion processes. Corrosion destruction on the surface of the samples of mode 2 is more sharply expressed than in the samples of modes 3 and 5.

The data of Table 2 show that the most favorable mode of steel surface treatment is mode 5. Mode 3 is close to it in the character of corrosion destruction; however, mode 3 has a sufficient number of negative potentials after prolonged holding of the samples in the medium. The samples obtained by mode 5 have minimal changes of the surface appearance under long tests, up to 240 h, and they have positive values of the electrode potentials, about +120 mV. This is a quantitative index of high stability of the surface films formed. It follows from the analysis of the polarization curves (see figure) that the samples treated in modes 1–5 have higher corrosion stability in comparison with modes 6–8: the currents of corrosion elements are lower than on untreated steel at similar potentials of polarization (see

figure). The discharge influence on the character of corrosion processes is the strongest in the samples treated by modes 1, 3, and 5, sample 1 showing the passive state. Despite some differences in polarization curves of samples 1, 3, and 5, the absolute values of currents are very low, fractions of $\mu\text{A}/\text{cm}^2$. Therefore, the differences observed in the courses of the curves for these samples are considered insignificant.

Hard modes of steel surface treatment (curves 6–8) worsen the corrosion stability of steel: the combination of high accelerating voltages and long treatment determines an increase in the steel corrosion rate by almost two orders of magnitude. A decrease in the treatment time at high specific discharge power also leads to worsening of stability of the material under study. The observed regularities are explained as follows. At high values of the glow discharge specific power, corresponding to high ion energies, on the surface there are formed porous films, which are an effective cathode with respect to the steel base in this medium. Efficiency of the formed oxide film as a cathode in the electrochemical corrosion process is determined, apparently, by its thickness, phase composition, and porosity. In modes 6–8, the surface film thickness is larger than in modes 1–5. One can judge this by both color scale (annealing colors) and data of gravimetric analysis and ellipsometric studies (Table 1). The generally known character of porosity dependence on thickness, i.e., porosity decrease with thickness increase [2–4], is violated in our experiments. The samples possessing thicker films treated by modes 6–8 have a much higher number of corrosion pits than the samples with thin oxide films. It is apparent that development of corrosion processes in the case of thick films is determined by considerable inner tensions in the films leading both to enlargement of corrosion pits and, probably, to change from the electrochemical mechanism of corrosion to the mechanochemical one [4, 8].

A certain influence on the character of polarization processes is exerted by preliminary holding of samples in the medium before the start of polarization. A series of tests on studying the influence of long sample holding on the character of the electrode processes has shown that, before the start of polarization, surface films are formed that increase the stability of materials in the given aggressive medium. A sharp decrease in corrosion element currents is found; in the samples treated by modes 5, 6, and 8, the presence of the passive region is fixed. However, despite a significant decrease in the corrosion currents, corrosion pits can be seen on the surface of the samples of modes 6–8. Therefore, connecting the corrosion rate decrease with formation of passive layers, one should not forget about possible pore blocking by corrosion products and, as a result, inhibition of anode dissolution of steel in the surface film pores. In the aspect of corrosion, these modes may be considered satisfactory, if there are no increased requirements to the product's outward appearance and to the surface color.



Figure

Analysis of the cathode polarization curves has shown that, irrespective of the treatment mode, corrosion currents are sufficiently low and one can talk about the occurrence of the electrochemical corrosion process with cathode control. Since in the cathode polarization process the surface films are reduced, the identity of cathode potentiodynamic polarization curves is qualitative proof of similarity of the chemical and phase compositions of the surface films and is in agreement with the data of ellipsometric studies and phase analysis (Table 1).

On the whole, according to the data of electrochemical investigations, the following conclusions may be drawn:

(1) treatment of the surface of steel in an alternating current glow discharge is accompanied by formation of oxide films favoring a decrease in the base corrosion rate in neutral liquid media;

(2) the highest quality films with respect to corrosion are formed at accelerating voltages of 900–1000 V on a substrate, at a discharge current density of 1.7–2.0 mA/cm^2 , and for a treatment time of 8–10 min.

Certain experimental modes of oxide surface film growth may be used for development of industrial processes of preliminary protection of metal products in conditions of product warehousing and mild modes of operation.

REFERENCES

1. Naumova, E.N., Kalinkov, A.Yu., and Kostrzhitskii, A.I., *Passive Films on Surface of Construction Materials and Their Protecting Properties*, *Kholodil'na Tekhnika Tekhnologiya*, 2001, no. 5 (74), pp. 46–51.
2. Roikh, I.L. and Koltunova, L.N., *Zashchitnye vakuurnye pokrytiya na stali* (Protecting Vacuum Coatings on Steel), Moscow: Mashinostroenie, 1971.

3. Roikh, I.L., Koltunova, L.N., and Fedosov, S.N., *Nanesenie zashchitnykh pokrytii v vakuume* (Deposition of Protecting Coatings in Vacuum), Moscow: Mashinostroenie, 1976.
4. Kostrzhitskii, A.I. and Lebedinskii, O.V., *Mnogokomponentnye vakuurnye pokrytiya* (Multicomponent Vacuum Coatings), Moscow: Mashinostroenie, 1987.
5. Kostrzhitskii, A.I., Karpov, V.F., Kabanchenko, M.P., and Solov'eva, O.N., *Spravochnik operatora ustanovok po naneseniyu pokrytii v vakuume* (Handbook of Operator of Installations for Coating Deposition in Vacuum), Moscow: Mashinostroenie, 1991.
6. Kubashevskii, O. and Hopkins, B., *Okislenie metallov i splavov* (Oxidation of Metals and Alloys), Moscow: Metallurgiya, 1965.
7. Fainshtein, A.I. and Litovchenko, N.A., Change of Properties of Oxide Film on Iron in Growth Process, *Zh. Fiz. Khim.*, 1980, vol. 51, no. 3, pp. 801–803.
8. Kostrzhitskiy, A.I. and Kalinkov, A.Yu., The New Mechanism of Corrosion in Pore of Cathode Coatings on Steel. Theoretical and Experimental Studies of Interfacial Phenomena and Their Technological Application, *Proc. VI Ukrainian–Polish Symposium*, Odessa, 2001, pp. 109–113i.
9. Fainshtein, A.I., Roikh, I.L., and Litovchenko, I.A., On Chemical Interaction of Films Obtained by Method of Metal Evaporation in Vacuum, with Oxide on Substrate, *Zh. Fiz. Khim.*, 1979, vol. 53, no. 5, pp. 1079–1082.
10. Fainshtein, A.I. and Kabanchenko, M.P., Oxidation–Reduction Processes on Steel Surface under Heating in Vacuum, *Izv. Akad. Nauk SSSR, Ser. Metally*, 1977, no. 4, pp. 183–188.

**ELECTRICAL PROCESSES
IN ENGINEERING AND CHEMISTRY**

Interaction of Electrolyte Cathode Properties and Electric Characteristics of Atmospheric Pressure Glow Discharge

I. N. Subbotkina, A. V. Khlyustova, and A. I. Maksimov

*Ivanovo State Chemicotechnical University, pr. Engel'sa 7, Ivanovo, 153000 Russia Institute of Chemistry of Solutions,
Russian Academy of Sciences, ul. Akademicheskaya 1, Ivanovo, 153045 Russia*

Received November 24, 2006

Abstract—The dependences of electrolyte cathode influence on electrical properties of glow discharge, namely, the drop in cathode potential and electric field intensity in the positive column were obtained for alkali metal chloride solutions. The drop in cathode potential and electric field intensity displayed an antibatic behavior when the electrolyte cathode acidity was varied. A pronounced character of this behavior was found for KCl solution. A mechanism for this behavior was suggested based on taking into account the contribution from ionization of alkali metal atoms.

DOI: 10.3103/S106837550703009X

INTRODUCTION

In glow discharge physics, the main role is played by the interphase boundary and the processes of charged and neutral-particle transport through this solution–plasma interphase. There exist literature data on the measurement of the drop in cathode potential under various conditions, such as the range of pressures, currents [1], the nature of the plasma-forming gas [2, 3], and solution acidity [4] when diluted electrolyte solutions are used as cathodes. In the present work, we studied the influence of the initial acidity in solutions of alkali metal chlorides on the drop in cathode potential and the field intensity in the positive column in the range of average concentrations of dissolved salts.

EXPERIMENTAL

A double cell with a solution working volume of 250 ml was used in experiments. The cell form allows us to avoid the interelectrode distance due to solution evaporation. The scheme of the cell is shown in [5]. The cell terminals are connected by a hose placed into a peristaltic pump providing circulation of the solution at a rate 60 ml/min.

The potential distribution in the positive column was measured by the shifting-anode method. This method assumes plasma properties independent of the length of the positive column. The length of the discharge gap varied from 0.5 to 1.5 mm; at a step of 0.1, the shifts were controlled by a B 670 cathetometer.

The drop in voltage in the discharge gap was measured by an F-30 digital ampere voltmeter. Solutions of LiCl, NaCl, and KCl in the concentration range 0.05–1 mol/l served as liquid cathodes. The initial acidity of the solutions varied in the range 1.5–12; the solu-

tions were acidified by addition of HCl and alkalified by adding of a corresponding hydroxide solution.

Extrapolation of the potential dependence on the length of the plasma zone in the discharge column to a zero interelectrode distance made it possible to find the drop in cathode potential, and the field intensity in the positive discharge column was determined as the first derivative of the voltage distribution $E = \frac{dU}{dX}$.

RESULTS AND DISCUSSION

Typical potential distributions at various initial values of the solution acidity are shown in Fig. 1. The experimental data on the dependences on the initial acidity of the electrolyte solution have shown that an obvious dependence is not observed in the case of salts LiCl and NaCl (Fig. 2), whereas the data for KCl presented in Figs. 3 and 4 show an antibatic behavior of the drop in cathode potential and electric field intensity in the positive column. In the region of acidic solutions, pH increase is accompanied by a significant decrease in the drop in cathode potential. The electric field intensity in the positive column in this region increases. At pH ~ 4 both values change at in a jumpwise manner in the direction opposite to the initial one; thereupon their smooth change in the initial direction is renewed. Thus, the increase in the cathode step in potential accompanies the decrease in the electric field intensity in the column, and vice versa. It is known from the literature data [6, 7] that, in comparison with water molecules, potassium atoms have an ionization energy less by a factor of 3 and an ionization section being larger by a factor of 4. This should lead to a constant of the potassium atom ionization rate exceeding the constant of water mole-

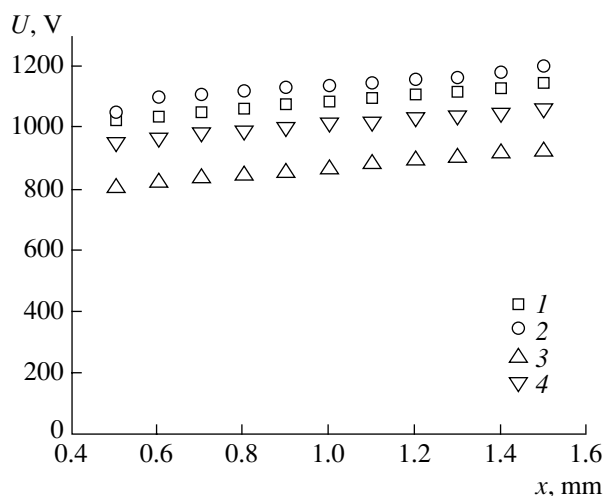


Fig. 1. Potential distribution in the positive discharge column with various initial pH values of NaCl solution with a concentration of 0.5 mol/l and a discharge current of 30 mA: (1) 1.54; (2) 3.43; (3) 4.13; (4) 12.34.

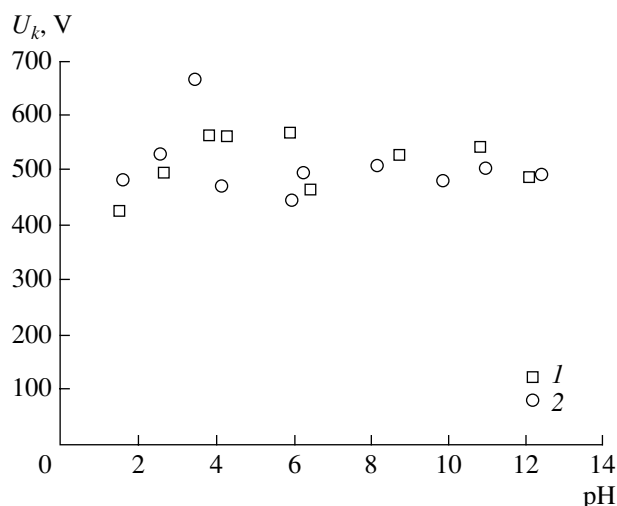


Fig. 2. Dependence of the drop in cathode potential on initial acidity of LiCl (1) and NaCl (2) solutions with a concentration of 0.5 mol/l and a discharge current of 30 mA.

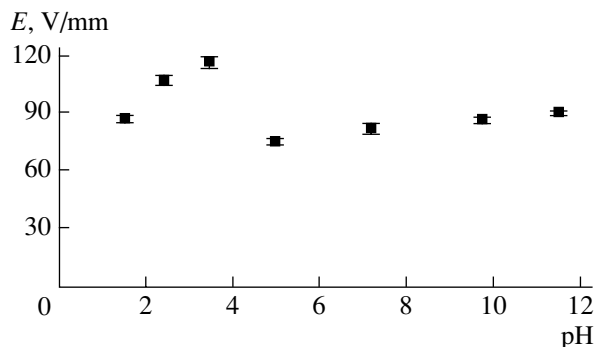


Fig. 3. Influence of initial acidity of potassium chloride solution on the field intensity in the positive column of the glow discharge with an electrolyte cathode. The salt concentration is 0.5 mol/l, and the discharge current is 30 mA.

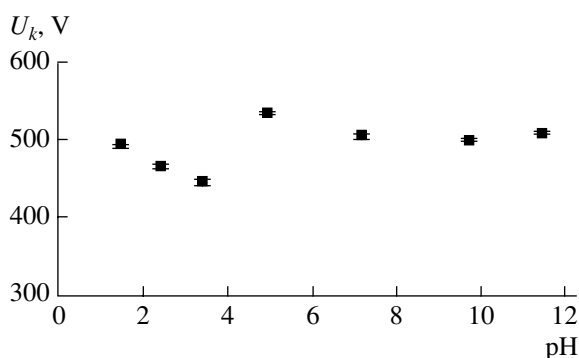


Fig. 4. The drop in cathode potential as a function of initial acidity of KCl solution with a concentration of 0.5 mol/l and a discharge current of 30 mA.

cule ionization rate by orders of magnitude. It is obvious that this mechanism is most clearly seen in the case of a potassium salt solution, in contrast to sodium and lithium, and it there should be even more contrast when solutions of rubidium- and cesium salts are used.

From analysis, we can draw the conclusion that with increasing concentration of metal atoms of a dissolved substance in the plasma zone, there is a tendency to antibatic behavior of the drop in cathode potential and the field intensity in the positive discharge column, shown in Figs. 3 and 4.

The field intensity dependence passes through a minimum. On the one hand, the decrease in field intensity occurs due to an increase in ionized metal atoms and due to facilitated discharge burning; on the other hand, with the increase of concentration of alkali metal atoms of a dissolved substance, the rate of the charge destruction increases due to recombination outside the

discharge, since the constant of recombination of ionized atoms with electrons is higher than in $H^+ H_2O^+$ ions, etc.

The behavior of the drop in cathode potential is mainly determined by two characteristics: the coefficient of ionization and coefficient of electron emission from the electrolyte solution. The decrease in the drop in cathode potential is explained by monotonic growth of the ionization coefficient. Independent data on the electron emission coefficient allowing accurate description of the abovementioned behavior are still lacking. We can only draw the conclusion that the change in solution composition influences the emission coefficient, and this dependence has the opposite sign.

The theory of discharge with electrolyte electrodes differs as follows from the existing classical theory of low-pressure glow discharge with metal electrodes. The chemical composition of the plasma zone is determined

Energy and section of ionization in the maximum for water molecules and alkali metal atoms of

	H ₂ O	Li	Na	K	Rb	Cs
E_i , eV	12.6	5.39	5.14	4.34	4.18	3.89
Q_i , 10^{-16} cm ²	2	4.2	4.2	8.7	14	12

by processes of solution-component transport and, thus, it is formed by the discharge itself.

Discharge occurs when a voltage sufficient for breakdown of the gas-discharge gap is applied between the electrolyte solution and a metal anode that is in the gas phase; its gas phase initial composition contains air or another plasma-forming gas with water vapor, the pressure determined by the system's initial temperature. In the initial period, the drop in cathode potential and field intensity in the column will set in. These are determined by the coefficient of electron emission from solution under bombardment of ions formed in the plasma of the initial chemical composition, and by ionization by impact of electrons of basic components in the initial gas phase. The discharge initiates when the solution component transport into the gas phase begins. This changes the gas phase chemical composition and, therefore, the conditions of the discharge balance in the plasma and its properties. Since discharge burning is also accompanied by a change in the solution's chemical composition, the coefficient of electron emission from solution may change in the burning process.

Analogously, interrelated changes in the plasma-solution interphase properties and the plasma properties should be observed when the composition and properties of the solution are changed in a specific manner.

As is seen from the data in the table, alkali metal atoms in comparison with water molecules have an ionization energy less by a factor of 3 and an ionization section larger by a factor of several. This should lead to a constant of the alkali metal atom ionization rate that

exceeds the constant of the water molecule ionization rate by orders of magnitude. This means that the contribution of alkali metal ionization to the total ionization rate may be great even at relatively mild conditions of discharge, i.e., diluted solutions and low currents.

REFERENCES

1. Hickling, A. and Ingram, M.D., Contact Glow Discharge Electrolysis, *Trans. Faraday. Soc.*, 1964, vol. 60, part 4, pp. 783–793.
2. Hickling, A. and Linacre, J.K., Glow Discharge Electrolysis. Part 2. The Anodic Oxidation of Ferrous Sulfate, *J. Chem. Soc.*, 1954, pp. 711–720.
3. Gaisin, F.M., Gizatullina, F.A., and Kamalov, R.R., Energy Characteristics of Discharges in Atmosphere between Electrolyte and Copper Anode, *Fiz. Khim. Obrab. Mater.*, 1985, no. 4, pp. 58–64.
4. Cserfalvi, T. and Mezei, P., Operating Mechanism of the Electrolyte Cathode Atmospheric Glow Discharge, *J. Anal. Chem.*, 1996, vol. 355, pp. 813–819.
5. Khlyustova, A.V., Maksimov, A.I., and Safiullina, E.M., Resonance Emission of Cathodic Layer of Glow Discharge with Electrolyte Cathodes, *Elekt. Obrab. Mater.*, 2004, no. 4, pp. 79–82.
6. Radtsig, A.A. and Smirnov, B.M., *Parametry atomov i atomnykh ionov. Spravochnik* (Parameters of Atoms and Atomic Ions. Handbook), Moscow: Energoatomizdat, 1986.
7. Kieffer, L.J., Low-Energy Electron-Collision Cross-Section Data. Part I: Ionization, Dissociation, Vibrational Excitation Atomic Data, *J. Devoted to Complications of Exp. Theor. Results in Atomic Phys.*, 1969, vol. 1, no. 1, pp. 18–89.

**ELECTRICAL PROCESSES
IN ENGINEERING AND CHEMISTRY**

Properties of Radiothermoluminescence of Polyethylene–Fibroin Composite

R. S. Ismayilova and M. M. Kuliev

*Institute of Radiation Problems, National Academy of Sciences of Azerbaijan,
pr. G. Dzhevaida 31a, Baku, AZ1143 Republic of Azerbaijan*

Received November 24, 2006

Abstract—In the given work, results of research of radiothermoluminescence (RTL) and electret properties of HDPE and composites on its basis containing a polar organic additive distributed in the volume of natural silk fibroin up to 50% are presented. It is established that changes in the molecular structure of HDPE by introduction of natural silk fibroin into it and radiation modification are shown in changes in RTL spectra. Complex research of RTL and electret properties of HDPE + fibroin composites has shown that, by studying RTL spectra of composites, it is possible to predict formation of high electret states in them.

DOI: 10.3103/S1068375507030106

INTRODUCTION

The creation of active polymer composite materials with improved piezoelectric, pyroelectric, and electret properties is stimulating experimental works on studying the degree of polymer interaction with fillers and relations between molecular mobility of macromolecules at the interphase with fillers and properties of polarization processes in them.

Recently, for analysis of the dynamic structure of polymers and composite materials on their basis, alongside such traditional methods as mechanical spectrometry, NMR, EPR, dielectric tests, electret–thermal analysis (ETA), etc., the method of radiothermoluminescence (RTL) has successfully been applied [1–4]. The dynamic structure is considered in terms of molecular mobility of structural elements playing the role of kinetic units in relaxation processes.

As previous works have shown [5–6], one of the effective methods for modification of structure and properties of polymers is introduction of fillers of organic nature. It is known that treatment of composite materials with ionizing radiation opens new possibilities in this direction [4]. On the other hand, stability of the aforementioned electroactive properties of polymer composites is determined by relaxation processes taking place upon heating of a sample and being connected with the molecular mobility, including motion of separate large and small kinetic units of polymers. In this respect, from both theoretical and practical viewpoints, it is interesting and important to study the effect of a polar organic additive on the relaxation processes and electroactive properties of composites. It is known that characteristics important for polymers are formed during synthesis [7, 8], so investigations should start from the initial polymer.

On the basis the foregoing, ETA was employed for investigation, because it is extremely sensitive to any changes in the sample and allows information to be obtained on intensity of the relaxation processes in composite multiphase systems. The polymer RTL curve is a row of luminescence peaks appearing owing to recombination of discharges stabilized in the process of radiation at low temperature. The luminescence peaks appear as the discharge recombination rate increases in the range of relaxation or phase transitions in the polymer. Therefore, the position of the luminescence peaks is closely related to the state of amorphous regions in the polymer, in particular, to the position of the relaxation and phase transitions [1–4].

In the present work, results are given of investigation of radiothermoluminescence and electret properties of HDPE and composites on its basis containing a volume-distributed polar organic additive of natural silk fibroin (up to 50 vol %) with the chemical formula $C_{15}H_{23}N_5O_6$.

EXPERIMENTAL

The samples in the form of a disk of thickness 100–150 μm were obtained from a homogeneous mixture of polymer–fibroin powders. The polymer phase was HDPE. The samples were placed on the bottom of a stainless steel cup with a diameter of 8 mm and covered with a stainless steel net for letting light out. Before radiation, the samples in the cups were evacuated in a glass ampule under a pressure of 1.33×10^{-3} Pa, and then the ampule was soldered and cooled down to 77 K by immersion into a Dewar vessel with liquid nitrogen. The evacuation time t required for removal of gases dis-

solved in the samples was determined as a function of film thickness by the formula

$$t = h^2/4K,$$

where h is the film thickness, and K is the diffusion coefficient in polymer, $\approx 10^{-3} \text{ m}^2/\text{s}$ [4].

Irradiation was performed by γ radiation from ^{60}Co on the installation K-25 at liquid nitrogen temperature. The dose rate was $3.3 \times 10^3 \text{ Gy/h}$. The RTL was measured by a TLG-69M device [1] at a heating rate of 12 deg/min in the temperature range from 77 to 273 K. Reproducibility of the positions of RTL maxima was $2^\circ\text{--}3^\circ$, as a rule. The sample illumination was recorded in the range of 300–820 nm by an FEU-51 photomultiplier tube, and then it was transformed into an electric signal and recorded on an electronic chart recorder. The sample temperature was recorded by a copper–constantan thermocouple.

For studying corona electrets, samples with a diameter of 40 mm were used, being thoroughly degreased before the experiment. Their polarization from the side of the nonmetallized surface was realized by a negative corona at a voltage of 7 kV on the base of a system of metal needles positioned vertically at a distance of 1 cm from the sample surface. The polarization time was 300 s. The electret difference of potentials was determined by the compensation method immediately after polarization and stabilization, in 30 days.

RESULTS AND DISCUSSION

Figure 1 shows the thermoluminescence spectra of natural silk fibroin and HDPE (curves 1 and 2) and of the composites obtained on their basis (curves 3–6) with different volume content of fibroin irradiated under a dose of $1 \times 10^4 \text{ Gy}$. In the temperature range 100–273 K, the RTL curve of initial HDPE containing no dissolved oxygen has two maxima at 150 and 220 K and an inflection in the region of 190 K. The transition observed at 150 K, being a distinctly pronounced low-temperature peak, is related by position and value of the activation energy of 0.13–0.15 eV to the motion of several methylene groups in amorphous regions of polyethylene. A weakly pronounced high-temperature second peak in the region of glass transition at 220 K is due to the mobility of segments in different structural regions, i.e., the amorphous phase, interphase layer, and amorphous sections in rays of spherulites. In the case of pure natural silk fibroin, a broad RTL curve with a maximum at 168 K was observed, the intensity of J luminescence being much less than the HDPE luminescence intensity.

The HDPE modification by introduction of the natural silk fibroin leads to the following changes in the RTL curves. A filler content up to 30 vol % in HDPE significantly increases the luminescence intensity in the low-temperature range, and the luminescence maximum temperature and the observed inflection shift to

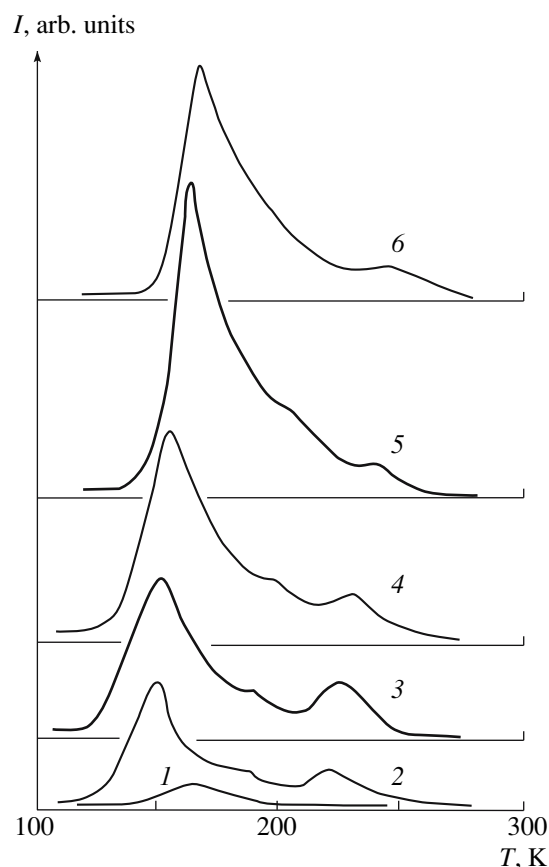


Fig. 1. Radiothermoluminescence of natural silk fibroin, HDPE, and composites on their basis: (1) natural silk fibroin; (2) HDPE; (3) HDPE + 5 vol % fibroin; (4) HDPE + 10 vol % fibroin; (5) HDPE + 30 vol % fibroin; (6) HDPE + 50 vol % fibroin. The absorbed dose is $1 \times 10^4 \text{ Gy}$.

higher temperatures: from 150 to 162 K and from 190 to 203 K, respectively. A content of natural silk fibroin up to 50 vol % results in a decrease in the luminescence intensity, the maximum temperature increases up to 168 K, and the inflection disappears. A filler content of 5 vol % leads to an increase in the glass transition peak at 220 K; a high content of the filler results in suppression and shift of the glass transition peaks up to 241 K; at 50 vol %, this peak almost completely disappears.

Introduction of a filler into polyolefins leads to chemical and physical changes in the polymer molecular structure. In particular, macromolecules in filled polyolefins may possess a certain quantity of overstressed bonds. The character of change in particular properties in the composite depends mainly on the fraction of the polymer found in boundary layers, on the degree of intermolecular interaction in this system, and on the flexibility of the polymer chains.

Figure 2 shows the dependence of the peak intensity on fibroin content in the polymer $J = f(C)$ for a low-temperature maximum of luminescence. It is seen that, after introduction of 30 vol % fibroin in the polymer, the luminescence intensity of the latter increases and

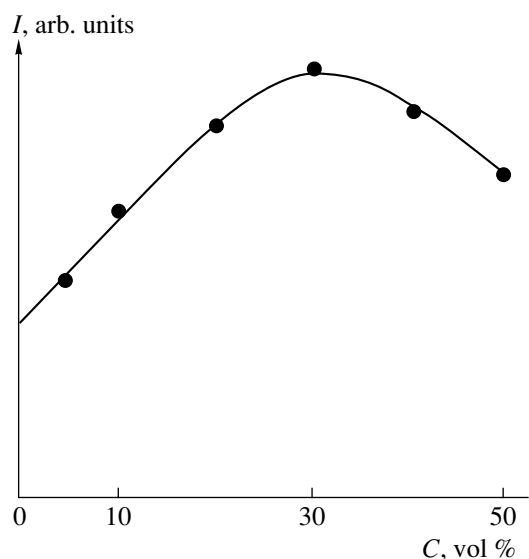


Fig. 2. Dependence of the low-temperature RTL peak intensity on the volume content of natural silk fibroin.

then decreases. Such a complex dependence of the luminescence intensity on filler content is explained as follows: the light intensity at a given temperature is proportional to the electron recombination rate

$$J \sim \Phi \frac{dn}{dt}$$

Here Φ is the fraction of electrons causing the light emission. The majority of electrons causing luminescence of an irradiated composite are released when trap cavities are broken. It appears that, at a filler content up to 30 vol %, the number of traps for electrons increases, and then breaking of the electron traps occurs and, therefore, the number of electrons captured on the traps becomes less, this leading to decreasing luminescence intensity.

As the filler volume content and, hence, the polymer fraction found in boundary layers increase, the molecular mobility of polymer chains and their kinetic units responsible for RTL formation decreases. This is the reason for the low-temperature luminescence shift.

The shift of the glass transition peaks towards higher temperatures at a high content of the filler is due to a sharp increase in the number of overstressed chemical bonds and to intensification of the decrease in segmental mobility of macromolecules near the filler solid surface. This causes a decrease in the electron recombination rate and, as a result, at fibroin content $C = 50$ vol %, the glass transition peak disappears.

Investigations of the electret properties of the composite HDPE + natural silk fibroin have shown that introduction of the filler monotonically decreases the initial potential difference U_0 and the stabilized potential difference U is of extreme character. That is, at first U increases and achieves its maximum at a concentra-

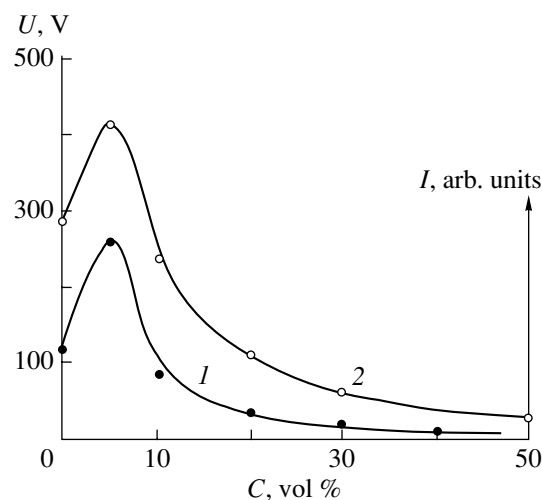


Fig. 3. Dependences of intensities of the glass transition peak (curve 1) and stabilized difference of potential (curve 2) of corona electrets of the composite HDPE + fibroin. The absorbed dose is 1×10^4 Gy; the polarization mode is $U_n = 7$ kV; $t_n = 300$ s.

tion of 5 vol % and then decreases and becomes even less than U of the electret of the initial HDPE matrix (Fig. 3, curve 1). It may be supposed that the electret potential difference being a superposition of the field of injected charges and field-oriented fibroin dipoles increases at first, achieves its maximum, and then decreases owing to the increase in concentration of oriented fibroin dipoles in the composite. It is clear that, at a high content of fibroin, the dipole-oriented polarization may completely compensate the field of injected charges, i.e., homocharges, this being observed experimentally. It should also be noted that, as the polymer fraction in the composite decreases, the concentration of localized charges, in the field of which the fibroin dipole orientation occurs, decreases as well.

The time dependence of the electret potential difference U has shown that the electret of the composite HDPE + 5 vol % fibroin is sufficiently stable and may be of interest for practical application.

The dependence of the luminescence intensity in the glass transition region of the composite HDPE + fibroin also has an extreme character (Fig. 3, curve 2) with a maximum at 5 vol % fibroin content. This shows that, at volume content of fibroin $C = 5$ vol %, the structural changes taking place in the polymer phase upon its filling, which determine the spectrum of localized levels in the polymer quasi band gap, are optimal from the viewpoint of charge stabilization, because sufficiently deep centers of charge capture with relatively high activation energy are formed. This explains the more stable electret properties of the composite HDPE + 5 vol % fibroin.

CONCLUSIONS

Thus, it is found that changes in molecular structure of the HDPE caused by introduction of natural silk fibroin into it and by radiation modification manifest themselves in changes in the RTL spectra. Comprehensive investigation of the RTL and electret properties of HDPE + fibroin composites has shown that, by studying RTL spectra of the composites, one may predict formation of a high electret state in them.

REFERENCES

1. Kuleshov, I.V. and Nikol'skii, V.G., *Radiotermoluminescensiya polimerov* (Radiothermoluminescence of Polymers), Moscow, 1991.
2. Kazakov, V.P., Korobeinikova, V.M., and Rykova, V.V., Radiothermoluminescence of Alkylsulfoxides, *Khim. Vys. Energ.*, 1998, vol. 32, no. 1, pp. 26–30.
3. Aulov, V.A., Kuchkina, I.O., Makarov, S.V., Pantyukhin, A.A., Ozerin, A.M., and Bakeev, N.F., Peculiarities of Radiothermoluminescence of Reaction Products of Ultrahighmolecular Polyethylene, *Vysokomol. Soedin. A*, 2003, vol. 45, no. 4, pp. 588–596.
4. Magerramov, A.M., *Strukturnoe i radiatsionnoe modifitsirovanie elektretnykh, p'ezoelektricheskikh svoistv polimernykh kompozitov* (Structural and Radiation Modification of Electret, Piezoelectric Properties of Polymer Composites), Baku: Elm, 2001.
5. Bagirov, M.A., Ismailova, R.S., Kuliev, M.M., and Nuriev, M.A., Influence of Natural Silk Fibroin Additions on Polyethylene Charge State, *Znanie, Ser. Fiz., Matem., Nauki o Zemle*, 2004, no. 2, pp. 42–45.
6. Abasov, T.F., Orudzhev, A.O., Khalafov, F.R., Kuliev, M.M., and Rashidov, S.F., Magnetic Field Influence on Change of Electrophysical Properties of High Pressure Polyethylene and Composites on its Basis, *Vysokomol. Soedin. B*, 2000, vol. 42, no. 6, pp. 1060–1064.
7. Joo, Y.L., Han, O.H., Lee, H.K., and Song, J.K., *Polymer*, 2000, vol. 41, no. 4, p. 1355.
8. Cook, J.T.E., Klein, P.G., Ward, I.M., Brain, A.A., Farrar, D.F., and Rose, J., *Polymer*, 2000, vol. 41, no. 24, p. 8615.

ELECTRICAL PROCESSES
IN ENGINEERING AND CHEMISTRY

Magnetic Field as a Moisture Transport Intensification Factor in Macrocappillaries

N. V. Polishchuk

Rovno State Humanitarian University, ul. Bandery 12, Rovno, 33028 Ukraine

Received January 16, 2007

Abstract—It is confirmed that nonuniform magnetic field influences the water transport rate in capillaries. An increase in the moisture motion rate is not provoked by the influence of the magnetic field's power on a water column in a macrocapillary, but it is caused by the reduction of moisture hardness. A possible mechanism of changing hardness is proposed.

DOI: 10.3103/S1068375507030118

The majority of natural bodies and those used in industry are moist solid disperse systems having a ramiform network of cracks, pores, and capillaries of various forms and dimensions. If special measures are not assumed, in these systems there is always water in the liquid or vapor–air phase. Liquid water is an active solvent; therefore, in pores and capillaries there are always solutions of electrolytes and nonelectrolytes; that is, moist solid disperse systems are multiphase and multi-component systems. Therefore, external force fields must cause motion of unfixed phases. In the case of inhomogeneous electric fields, this has been clearly proved theoretically and experimentally in the works of A.V. Lykov, N.V. Churaev, M.K. Bologa, M.S. Panchenko, and others.

The most essential component of volume density of ponderomotive forces [1] influencing liquid from the standpoint of external electric field is the term $f_e = \rho_e \vec{E}$, where ρ_e is the density of electric charges (ions and other charged particles) in the liquid and \vec{E} is the field intensity in the given point of liquid or vapor volume. Aquated ions acquiring an additional rate component drift chiefly in one direction, entraining water outside hydration walls and thus increasing the inner moist transport in capillaries and pores. This component acts in both homogeneous and inhomogeneous field.

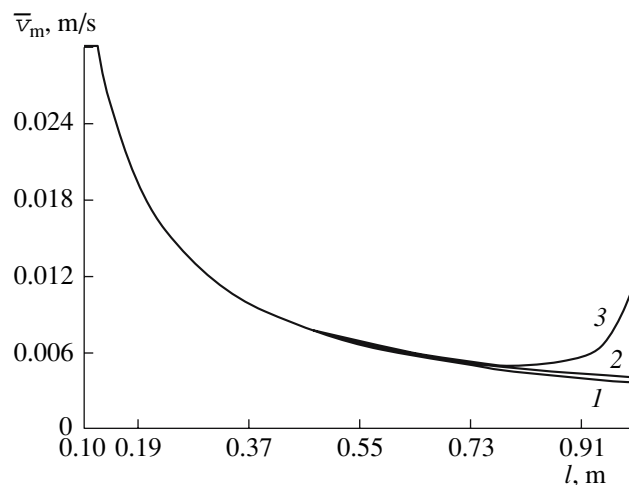
Magnetic charges (Dirac monopoles) do not exhibit themselves in nature, and there is no direct analog for the force $\rho_e \vec{E}$ influencing moisture as in the case of constant homogeneous electric field. Therefore, probable force influence on water, such as diamagnetic force, may be exerted by inhomogeneous magnetic field alone. This was noted by Lykov in monograph [2], where an expression for the water flow density j_m in

capillary–porous colloidal bodies in constant inhomogeneous magnetic field is given:

$$\vec{j}_m = -a_m^m \rho_0 \pi_m \vec{\nabla} B, \quad (1)$$

where a_m^m is the moisture magnetic diffusion coefficient, ρ_0 is the density of the porous solid phase, π_m is the sample magnetic polarization, and B is the magnetic field induction.

The figure in [2, p. 431] shows that the presence of constant inhomogeneous magnetic field significantly accelerates the capillary absorption by both elementary capillary and porous bodies. It is also noted in [2] that at ∇B of about 1250, distilled water viscosity decreases by a factor of 1.5; unfortunately, the unit of measurement is not given. However, the height of the capillary



Dependence of the average rate \bar{v}_m of meniscus motion in a capillary tube of radius 0.2×10^{-3} m on water column length, l : (1) in the absence of field; (2) in homogeneous magnetic field; (3) in inhomogeneous magnetic field.

rise determined by the Jurin formula does not depend on the presence of magnetic field. Therefore, the magnetic field only influences the capillary absorption kinetics.

The given experimental data do not allow us to draw an unambiguous conclusion as to which of the factors, force or viscous, play the decisive role. It is shown in [3] that inhomogeneous magnetic field influences the process of water molecule diffusion in silica gel KCM-5, potato starch, and cellulose. This influence is shown by a certain increase in the moisture diffusion coefficient in the mentioned microporous bodies. It is assumed that the reason determining the character of these changes is the force influence of the field on separate molecules of water. In [4] it has been noted that coefficients of molecular gas transport, heat conductivity in particular, change in constant magnetic or electric field; that is, the Senftleben effect takes place. The basis of this effect is the dependence of cross-section of interaction of non-spherical molecules on their orientation; that is, on angle between the direction of the relative rate of colliding molecules and their moments of rotation. The external magnetic or electric field causes precession of magnetic or dipole moments of molecules, whence an effective increasing of the interaction cross section occurs and, therefore, the transport coefficients change. As hygroscopic moisture content increases, i.e., the amount of vapor molecules decreases when they are adsorbed, when a polymolecular film is formed and free space for their motion is reduced, this influence decreases and it practically disappears when the maximal hygroscopic moisture content is achieved. In this state the microcapillaries are filled with liquid water, i.e., the capillary condensation moisture. Under the influence of the magnetic force field on a moist powder-like body, water could flow to macrocapillaries, increasing the moisture content of the porous sample at a relative humidity of the vapor-air medium equal to unity. However, this does not occur. Hence, water motion in the macrocapillaries and especially in the capillary tubes, where the water transport rate is considerably influenced by the gravitational field, the influence of inhomogeneous magnetic field must be insignificant.

On the other hand, it is noted in [5] that N.A. Umov, studying free drop outflow of diamagnetic and paramagnetic liquids in magnetic field, has observed deformation of drops depending on the value of the intensity and gradient of the field. A change in drop formation rate approximately satisfies the equation $\tau_0 P \approx \tau P_0$, where τ_0 and τ are the time of outflow of an equal quantity of drops in the absence and presence of field, and P_0 and P are their masses, respectively. In the same work there is a reference to the works of S.G. Romanovskii, E.A. Raskin, and A.P. Zambran, where it is noted that capillary impregnation of quartz powder with 10% NaCl solution has shown an increase in the impregnation rate in inhomogeneous field and an influence on kinetics of mercury capillary rise. The authors of [5]

also give results of their own experimental investigations of the phenomenon of liquid drop deformation during outflow from the capillary in inhomogeneous magnetic field. In [6] results of investigation and wide practical use of magnetic treatment of water systems are generalized and analyzed. An increase in surface tension in water systems after magnetic treatment within the range of 1–3 mN/m is mentioned. However, these changes are interpreted differently by the authors. It is noted in [7] that water is an open system actively exchanging both energy and matter with the external medium. For example, interaction of water and gases in the form of their evolution or dissolution is inevitable, since preliminary removal of gases from water by pumping or boiling may substantially change the water under study. Ions are always present in water, including in distilled water. Thus, changeability of properties and various experiments with water are specific attributes of it. One may suppose that there are a number of reasons for the difficulty in laboratory estimation of the change in water properties after magnetic treatment.

It follows from the above that magnetic treatment exerts the strongest influence on the properties of heterogeneous systems; this is probably a result of a peculiar “multiplying” action of the interphase developed surface; naturally, it is preserved for a long time, and in some cases it is irreversible [6].

The simplest model of a real moist capillary-porous body is a cylinder capillary, wherein liquid moves, e.g., during water absorption. Since, among other compounds, the largest and most diverse group in the earth and the crust consists of compounds of silicon and oxygen (which actively interact with water by the physical adsorption mechanism, partially dissolving in it), a quartz capillary tube with a diameter of 0.2 mm was chosen as the subject of investigation. The experiments were carried out with distilled water in equilibrium with atmospheric gases, with a specific electric conductivity of water of $85 \mu\text{S}/\text{m}^{-1}$. The tube length was 1 m. This length was chosen because in the end, the absorption rate is very small and the influence of the force of magnetic field on this process can be found. In order to avoid the influence of the gravitational field on liquid motion, the capillary tube was positioned horizontally. The influence of the hydrostatic pressure of liquid in the vessel on its motion in the capillary tube was avoided by maintaining the liquid surface at the upper edge of the vessel. The tube entry hole was placed at the same level. The horizontal positioning of the tube was due to its placement on the coordinate table with a micrometer screw and control by a microcathetometer KM-6. The position of the moving meniscus was determined by an automatic system based on computer analysis of a picture of the liquid meniscus formed by the optical system of television camera. This made it possible to obtain the graphic dependences $l(\tau)$ and $dl/d\tau$ (τ) on the monitor and in the recording. The length of the liquid column l was fixed with an accuracy of ± 1 mm and 0.1 s in the time of liquid motion. The capillary tube was

cleaned by keeping it in a chromium mixture for two days, washing with distilled water, and drying with compressed air. In the course of capillary rise of water in a quartz tube cleaned in such a way, $\cos\theta \approx 0.98$. The diameter and taper of the capillary tube was controlled by a KM-6 long-focus microscope. The diameter was measured with an accuracy of $\pm 3 \mu\text{m}$. The taper of the tube did not exceed 10^{-5} – 10^{-6} .

For the magnetic field obtaining a constant magnet was used with diameters of poles of 11×10^{-2} m and a distance between them of 7×10^{-3} m. Between them along the diameter, the end part of the capillary tube was placed. Its edge was in the midpoint between the poles. The intensity of the homogeneous field H along the axis between them was 2.16×10^5 A/m. For obtaining a sharply inhomogeneous field, the sliding poles were drawn apart by 6×10^{-2} m and one of the poles was superimposed with a taper tip with a base equal to the pole area and a height of 3×10^{-2} m. The tube came from the outside of the magnet, perpendicular to its axis, and its edge was in the immediate neighborhood of the top of the taper's tip. Space distribution of the magnetic field intensity was determined by the IMI-1 and Shch-30 devices; by numerical differentiation, the field gradient ∇H was found for the specific distance at which the moving meniscus was placed. The field gradient varied from zero outside the magnet to 2×10^8 A/m².

As it is known, a body with a magnetic moment p_m in an inhomogeneous magnetic field is influenced by the force, its component along the axis α ($\alpha = x, y, z$) being equal to

$$F_\alpha = p_m \frac{dH}{d\alpha}. \quad (2)$$

Since the magnetic moment is determined by the formula

$$p_m = m\chi H, \quad (3)$$

where m is the sample mass and χ is the magnetic susceptibility per sample mass unit, relation (2) at $\alpha = x$ may be written in the form ($H \equiv H_x$)

$$F_x = m\chi H \frac{dH}{dx}. \quad (4)$$

Hence, the mass of the water column in inhomogeneous magnetic field must be influenced by force (4). Since water is diamagnetic, this force is directed against the field gradient and must hinder the absorption process. Then the Porkhaev equation [8] for the cross section average rate \bar{v}_m of the meniscus motion in inhomogeneous magnetic field will be written in the form

$$\bar{v}_m = \frac{dl}{d\tau} = \frac{r_0^2 \rho}{8\eta} \left(\frac{2\sigma \cos\theta}{r_0 \rho l} - \frac{f_m}{\rho} \right), \quad (5)$$

where r_0 is the capillary radius; η is the viscosity; ρ is the water density; σ is the surface tension; θ is the wet-

ting angle; and f_m is the force acting from the field side per substance volume unit:

$$f_m = \rho\chi H \frac{dH}{dx}. \quad (6)$$

Thus, according to (5), taking into account (6), water in the final stage of absorption must move with decreasing rate in comparison to the one in the absence of field.

As follows from the figure, the rate does not decrease; on the contrary, it increases as the meniscus enters the region of inhomogeneous magnetic field (curve 3). The closer the meniscus comes to the maximal value of the field gradient, the more significant its rate increase. In the case of homogeneous magnetic field absorption curve (2) is insignificant; however, it coincides with the curve (1), the absence of field. This is explained by the fact that near the space between the poles, there always exists a field gradient, although it is considerably less than the artificially created one. This testifies to the special role of the field gradient in the liquid motion rate, increasing at the final stage of absorption. When the direction of inhomogeneous field is changed by putting the taper tip on the other pole, the absorption rate does not change. If the pole with the taper tip is moved aside the capillary tube, the field gradient and the absorption rate decrease, approximating the value in the absence of field (curve 1).

Thus, the force factor does not exert a decisive influence on the water absorption rate. It is obvious that, primarily, a decrease in water viscosity is such a factor, since the values of other parameters (ρ , σ , θ) for hypothetically absolutely pure water are determined by forces of interaction between water molecules themselves or between molecules of water and solid phase. The magnetic field energy is insufficient for changing the intermolecular interaction forces. Since viscosity, or internal friction, is caused by pulse transfer by thermal motion of molecules in liquid with an inhomogeneous distribution of rates of its spheres, the magnetic field cannot appreciably change the molecule thermal rates either. However, the influence of impurities should be taken into account. Water always contains dissolved and microheterogeneous impurities. Even extremely pure water that is carefully maintained, can quickly acquire impurities, dissolving container walls that are seemingly insoluble. Distilled water is also contaminated, to say nothing about natural or delivered water. For example, 1 m³ distillate contains, in addition to ions, approximately 1×10^{10} particles with dimensions of 10^{-8} – 10^{-7} m [6]. These impurities strongly and differently influence the structure and, therefore, physicochemical properties of water. In addition, all these particles and bubbles carry electric charges [9]. They also take part in thermal motion; a considerable amount of them always move perpendicular or at an angle to the magnetic field lines. They are influenced by the Lorentz force, which imparts additional motion in the plane per-

pendicular to vector \vec{B} to hydrated ions and charged disperse particles; therefore, at the transition from one moving sphere of liquid into another the motion pulse changes as well. In the magnetic field there change hydration number of ions and particles and their diffusion kinetics; that is, rate of recombination of intrinsic and impurity ions and coagulation of particles [6, 7, 9]. These processes lead to reconstruction of supermolecular structures of water [10] and, as a result, the number of free translation molecules increases, also decreasing viscosity.

This also stems from the fact that during motion in the capillary, water is in a stretched state under the influence of the capillary pressure gradient. It is apparent that water with impurities under superimposed magnetic field should be considered as a set of local strongly nonequilibrium subsystems. Hence, one has to abandon the approach to such a system as a continuous medium [11] and to state that the magnetic properties of components, especially colloidal ferromagnetic impurities, play an important role in the changes of kinetic processes.

Let us note that problems of heat exchange in MHD flows, in channels with moving magnetic liquid, are the most thoroughly studied, whereas problems of moisture transport in macrocapillaries of solid disperse systems have been investigated insufficiently, which gave impetus for this work.

REFERENCES

1. Polishchuk, N.V., Intensification of Heat–Mass–Transport in Macroporous Bodies in the Processes of Moistening and Drying under the Influence of Strong Electric Fields, *Extended Abstract of Cand. Sci. (Eng.) Dissertation*, Kiev, 2006.
2. Lykov, A.V., *Teoriya sushki* (Theory of Drying), Moscow: Energiya, 1968.
3. Mosievich, A.S., Study of Influence of Electric and Magnetic Fields on Internal Mass Transport in Solid Disperse Systems of Various Physical–Chemical Nature, *Cand. Sci. (Phys.–Math.) Dissertation*, Kiev, 1982.
4. Borman, V.D., Nikolaev, B.I., Ryabov, V.A., and Troyan, V.I., Parametric Resonance of Heat Conductivity Coefficient of Molecular Gases in Magnetic and Electric Field, *Inzh. Fiz. Zh.*, 1977, vol. 3, no. 2, pp. 263–270.
5. Aleinikov, N.A. and Vasil'ev, A.N., Deformation Effect and Kinetics of Liquid Dispersion in Magnetic Field, *Inzh. Fiz. Zh.*, 1970, vol. 19, no. 6, pp. 1118–1121.
6. Klassen, V.I., *Omagnichivanie vodnykh sistem* (Magnetic Treatment of Aqueous Systems), Moscow: Khimiya, 1982.
7. Klassen, V.I., *Voda i magnit* (Water and Magnet), Moscow: Nauka, 1973.
8. Porkhaev, A.P., Kinetics of Absorption of Liquids with Elementary Capillaries, *Kolloidn. Zh.*, 1949, vol. 11, no. 5, pp. 346–353.
9. Gamayunov, N.I., Coagulation of Suspensions after Magnetic Treatment, *Zh. Prikl. Khim.*, 1983, no. 5, pp. 1038–1047.
10. Kirgintsev, A.N., On Mechanism of Magnetic Treatment of Liquids, *Zh. Fiz. Khimii*, 1971, vol. 45, no. 4, pp. 857–859.
11. Blum, E. Ya., Mikhailov, Yu.A., and Ozols, R. Ya., *Teplo–i massoobmen v magnitnom pole* (Heat and Mass Exchange in Magnetic Field), Riga: Zinatne, 1980.

ELECTRICAL TREATMENT OF BIOLOGICAL OBJECTS AND FOODSTUFFS

Kinetics of Drying Sugar Beet Parenchyma Tissues Desugarized by the Electric Treatment

M. P. Kupchik^a, V. A. Mikhailik^b, V. M. Fales^a, and N. A. Sheiko^a

^a National University of Food Technologies, ul. Vladimirska 68, Kiev, 01013, Ukraine

^b Institute of Technical Thermophysics, Ukrainian NAS, ul. Bulakhovskogo 2, Kiev, 03164, Ukraine

Received November 17, 2006

Abstract—The kinetics of drying sugar beet parenchyma tissues treated in a pulse electric field are studied in this work. During the drying process the following dependences were obtained: the material specific humidity vs. time, the drying rate vs. material specific humidity, the material temperature vs. material specific humidity. The influence of preliminary treatment of the parenchyma tissues of sugar beet roots before the extraction in a pulse electric field on the drying process was investigated. It is shown that the electrical treatment exerts a positive action on the internal mass transfer, which defines the kinetics of drying. If the regime and the process of the electric treatment are efficient, the drying duration can be significantly reduced.

DOI: 10.3103/S106837550703012X

INTRODUCTION

The results of research devoted to the interaction of electrical fields with the cellular structures of beet tissue and their components in an aqueous medium is of great interest both in the scientific and practical aspects related to their possible industrial application [1].

Electroporation is used in various food technologies dealing with the extraction of valuable and useful components of vegetal stock, which include the plasmolysis of cellular structures as an important stage of the process. In the sugar industry, for example, the saccharose extraction efficiency from sugar beet tissues depends on the degree of the destruction of these structures. The same refers to the completeness of the juice yield from vegetables and fruit in the food-canning industry [2]. Intensive work is underway, devoted to the electric pretreatment of vegetal raw materials with the aim of reducing time and energy expenditure during the drying process [3].

In the sugar industry, an urgent problem arises related to the utilization of damp pulp. Since damp pulp reduces consumption and the pulp loses its quality in open storages, a significant share of it remains unused. This aggravates the ecological situation in the areas where sugar refineries are located, and utilization of pulp is required, leading to the additional costs. The manufacturing of dry pulp has not become widespread in Ukraine because of the large energy expenditures required for the process. In this connection the study of the drying kinetics of the pulp produced after treatment of the beet strips in electric field is of great interest.

In the present work results are presented related to the study of drying the desugarized parenchyma tissues of sugar beet subjected to a pulse electric current.

EXPERIMENTAL METHOD

The samples of parenchyma tissues of sugar beet roots with cylindrical shape (height and diameter of 20 mm) were subjected to electric treatment. A generator of sinusoidal voltage with a peak pulse was used as a voltage source (Fig. 1).

The treatment of tissues was performed in a pulse electric field with a strength of 500 V/cm for 2 and 6 s; the sample was placed in a cylindrical polypropylene cell with a diameter of 20 mm. Stainless steel electrodes were connected to the end walls of the sample

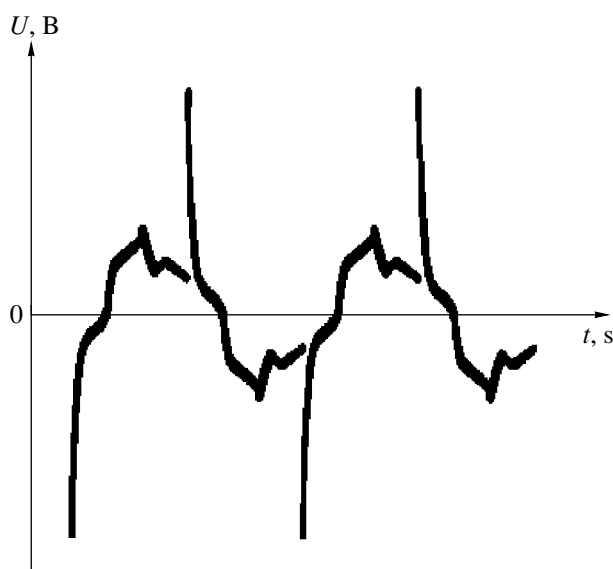


Fig. 1. Voltage oscillogram.

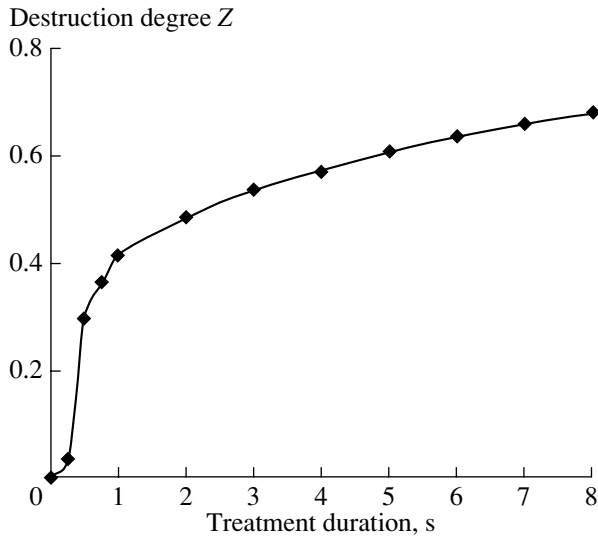


Fig. 2. Dependence of the degree of destruction of the cellular structure of parenchyma tissues of sugar beet roots vs. the duration of sinusoidal field action using a field strength of 500 V/cm with a peak pulse.

wetted with fresh sugar beet juice using a special compression unit.

A needle probe with a thermoelement was inserted in the center of the sample through the hole in the cell wall to control the temperature.

In the process of electric treatment, we measured the voltage across the electrodes, the current, the duration of treatment, and the sample temperature.

The sample conductivity was determined at 25°C before and after treatment at a frequency of 1000 Hz.

The destruction of cellular structures of the vegetal tissue due to the action of electric field was evaluated

according to the factor of the degree of destruction Z , which was calculated using the measured sample conductivity before and after treatment [4]:

$$Z = \frac{\sigma - \sigma_i}{\sigma_f - \sigma_i}, \quad (1)$$

where σ_i is the conductivity of the native tissues; σ is the conductivity of the tissues after the action of electric field; σ_f is the conductivity of tissues after unfreezing of a sample that had been cooled and stored in a freezing chamber at -20°C for 12 h. It was assumed that the greatest destruction of the cellular structure ($Z = 1$) is achieved at freezing.

Figure 2 shows the typical curve of the dependence of the degree of destruction of the parenchyma tissues under the action of modulated sinusoidal field with a strength of 500 V/cm with the peak pulse vs. the time of treatment.

After electric treatment, the sample was cut into five round slices with a thickness of 5 mm. Each slice in turn was divided into fragments 5 mm wide. For desugarization, the fragments of tissues were submerged for 60 min in a glass of 100 g of distilled water placed in a thermostat at 55°C . Saccharose extraction was performed with continuous controllable stirring. The desugarized fragments prepared in this way were dried after extract separation.

The efficiency of the electric treatment on the drying kinetics was evaluated by comparison with the drying kinetics of samples that had not been subjected to electric field. For this, the tissue fragments identical with the treated ones were desugarized in equivalent hydrodynamic conditions for 60 min at 75°C .

The process of convective drying was investigated using a test bench; a schematic diagram is shown in Fig. 3.

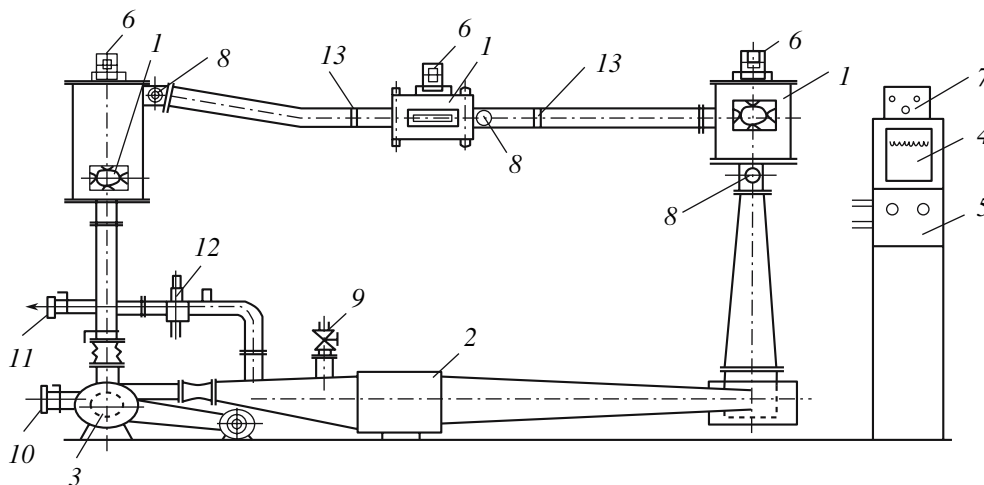


Fig. 3. Schematic diagram of the test bench: 1—drying chambers; 2—calorifier; 3—fan; 4—potentiometer; 5—control panel; 6, 7—modules of the automated system of temperature control; 8—resistance thermometers; 9, 10, 11—sleeve valves; 12—psychrometer; 13—special grates.

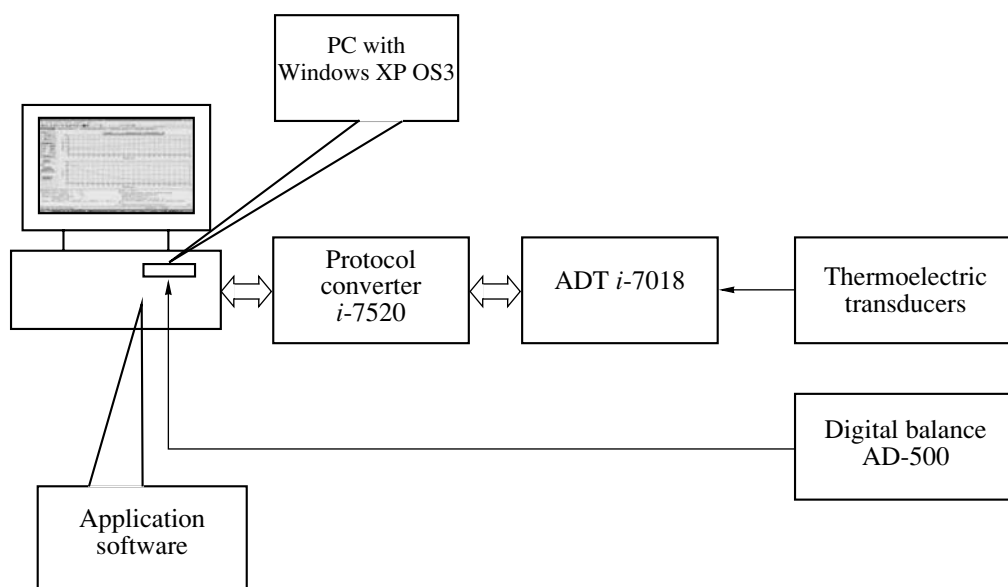


Fig. 4. Schematic diagram of the automated system for the acquisition and processing of data from the drying test bench.

The test bench includes a system of isolated air ducts with units for heating and circulation of the heat carrier, drying chambers, and circuits and instruments to control the process parameters and to measure magnitudes that characterize the drying process of the material under investigation.

The drying chamber (1) is a rectangular metal box with a hatch to insert the samples. The hatch and the opposite chamber wall are supplied with transparent glass windows that allow one to watch the material state during drying.

The zone of preparation of the heat carrier comprises a three-section electric calorifer with the power of 45 kW. An automated system for controlling the heat carrier temperature is based on an ERT-4 electrical regulator (7) and TSM-50 resistance thermometers (8).

The circulation of the heat carrier is produced using a centrifugal fan (3) of medium pressure. The rate is changed by the adjustment of the speed of rotation of the fan actuator. The ratio between the exhaust air and the fresh air may be controlled by sleeve valves (9, 10, 11).

The test bench is equipped with an automated data acquisition and processing system (Fig. 4), which is comprised of a personal computer with Windows XP, special application software, a channel for temperature measurement that consists of an analog-to-digital transducer (ADT) based on an i-7018 unit, an i-7520 interface (protocol converter), as well as an AD-500 automated digital balance.

The temperature of the drying agent and the studied sample was measured during the drying process using thermoelectric transducers (type L) inserted in needle-like probes. The voltage from the transducers is transformed into digital format using the ADT and is sent to the computer via the interface.

The application software allows continuous acquisition of data on the drying process, performance of the necessary computations, and drawing of plots.

Before the measurements, the test bench was brought to the specified temperature regime and then the investigated material was put on the balance plate placed in the drying chamber. The needle probe with the temperature sensor was inserted into the central part of the fragment to be studied.

The drying process was considered ended when the mass of the studied material remained constant. The same temperature (80°C) and the rate of the drying agent (2 m/s) were used in the experiments. To determine the content of dry substances, sample dewatering was continued at 104–105°C.

EXPERIMENTAL RESULTS

The character of the drying process is most completely described by the drying curves using the water content–time coordinates (Fig. 5), as well as by the dependences of the drying rate and the temperature of the material on the water content in it (Fig. 6) [5, 6].

For comparison of the kinetic curves for samples with different initial water contents, the current water content is usually presented in dimensionless form (Figs. 7 and 8).

Analysis of the curves of the drying rate (Fig. 7) shows that electric treatment leads to an increase in the rate at all drying stages (curves 2 and 3). The sample subjected to the action of the pulse electric field for 6 s (curve 3) displays greater values of the drying rate in comparison with the sample treated for 2 s (curve 2). This difference is observed mainly due to a somewhat greater initial water content, as seen in Fig. 5. However,

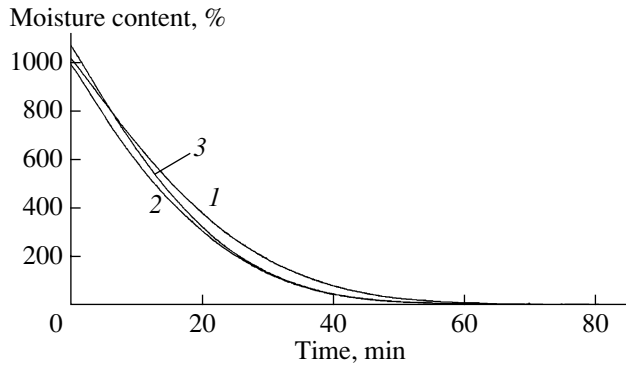


Fig. 5. Drying curves of the samples of desugarized parenchyma tissues of sugar beet roots after electric treatment for 2 (2) and 6 s (3); (1) without electric treatment.

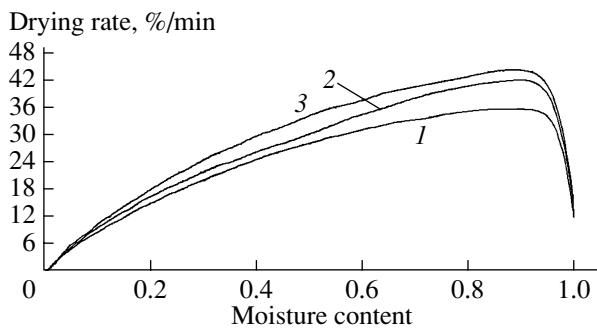


Fig. 7. Curves of the drying rate of the samples of desugarized parenchyma tissues of sugar beet roots after electric treatment in a pulse electric field for 2 (2) and 6 s (3); (1) without electric treatment.

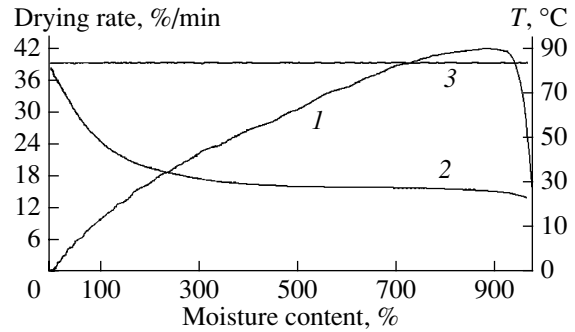


Fig. 6. Curves of the variation of the drying rate (1) and the temperature (2) in the central part of the sample of desugarized parenchyma tissues of sugar beet roots during the drying process after electric treatment in a pulse electric field for 2 s; (3) drying agent temperature.

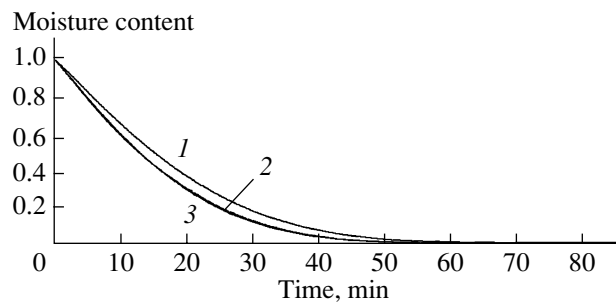


Fig. 8. Curves of the variation of the dimensionless moisture content in the drying process of the samples of desugarized parenchyma tissues of sugar beet roots after electric treatment for 2 s (2) and 6 s (3); (1) without electric treatment.

the drying duration of these samples to the equilibrium water content was practically the same (Fig. 8).

The drying of pulp is usually performed to a moisture content of 8–10%, which corresponds to the equilibrium water content in storage conditions. Measurements of the drying duration of the samples to a moisture content of 10% have shown that the drying time depends hardly at all on the duration of electric treatment. Thus, at a sample treatment for 2 s, the drying duration is 32.5 min. With an increase in duration of the electric action to 6 s, the drying time decreases by only 0.4 min. At the same time, the drying duration of the sample that was not treated by the electric field is 37.0 min. It is clear that the electric treatment for 2 s decreases the drying time by 4.5 min, which amounts 12.2% of the drying time of the untreated sample.

The dependence of the drying duration on the destruction degree of the cellular structure of desugarized parenchyma tissues of sugar beet roots under the action of sinusoidal field with the peak pulse was not

observed. This may be due to the action exerted by the extraction process on the tissue structure.

CONCLUSIONS

The investigations of the action of the pulse treatment at an electric field strength of 500 V/cm, which precedes the extraction of the parenchyma tissues of sugar beet roots, on the drying kinetics of desugarized tissues have shown that it exerts a positive influence on the internal mass transfer, which defines the drying kinetics.

With a proper choice of the regime and realization of electric treatment, the drying duration may be significantly reduced. The results have shown that the drying duration may be reduced by 11–12% when the relative degree of destruction of the cellular structure of vegetal tissue reaches 0.5–0.6; at the same time, the extraction temperature decreases by 20°C.

REFERENCES

1. Kupchik, M.P., Development of the Beet Sugar Technology Using a Low-Frequency Electric Field, *Doct. Sci. (Eng.) Dissertation*, Kiev, 1991.
2. Bazhal, M.I., Lebovka, N.I., and Vorobiev, E., Pulsed Electric Field Treatment of Apple Tissue During Compression for Juice Extraction, *J. Food Eng.*, 2001, no. 50, pp. 129–139.
3. Lebovka, N. I., Shynkaryk, M. V., and Vorobiev, E., Drying of Potato Tissue Pretreated by Ohmic Heating, *Drying Tech.*, 2006, no. 24, pp. 601–608.
4. Lebovka, N.I., Bazhal, M.I., and Vorobiev, E., Estimation of Characteristic Damage Time of Food Materials in Pulsed Electric Fields, *J. Food Eng.*, 2002, no. 54, pp. 337–346.
5. Lykov, A.V., *Teoriya sushki* (Theory of Drying), Moscow: Energiya, 1968.
6. Ginzburg, A.S., *Osnovy teorii i tekhniki sushki pishchevykh produktov* (Basics of the Theory and Technology of the Drying of Foodstuffs), Moscow: Pishchevaya Promyshlennost', 1973.

EQUIPMENT
AND INSTRUMENTS

Increasing the Energy Output of High-Voltage Pulse Capacitors for Downhole Devices

I. Yu. Grebennikov, V. I. Gun'ko, A. Ya. Dmitrishin, and L. I. Onishchenko

*Institute of Impulse Processes and Technologies, National Academy of Sciences of Ukraine,
pr. Oktyabr'skii 43-A, Nikolaev, 54018 Ukraine*

Received January 10, 2007

Abstract—Problems of increasing the specific energy output of high-voltage pulse capacitors for downhole electrical hydropulse devices are reviewed.

DOI: 10.3103/S1068375507030131

Creation of downhole electrical hydropulse complexes to restore the output of oil wells is one of the lines of activity of the Institute of Impulse Processes and Technologies of the National Academy of Sciences of Ukraine. In the course of processing, the submersible device moves in the well along its perforated region, generating electric discharges with the prescribed frequency. The removal of paraffinic, bituminous, and solid deposits from the surfaces of the well takes place and its porosity in the area of the oil-bearing stratum is reestablished.

The heavy demands imposed on the submersible device are explained by the peculiar conditions of its operation, such as small diameter sizes and possible axial curvature of the well shaft, as well as high values of the external hydrostatic head (up to 50 mPa) and ambient temperatures (up to 373 K) at depths to 5000 m. Improvement of borehole electrical hydropulse device equipment lies in the reduction of mass–clearance indices and enhancement of the operating characteristics of all its components.

In this connection, the purpose of this work is to carry out an analysis of the level achieved in the area of creation of high-voltage pulse capacitors of submers-

ible electric discharge devices and to evaluate the prospects for increasing the specific energy content of the capacitors used in order to upgrade the operating characteristics of submersible devices.

With the aim of reducing the clearance and mass of the submersible part, the borehole device has a block structure; the largest portion of its length and mass is accounted for by a capacitive accumulator of electric power. Creation of small-sized borehole devices is possible at the expense of an increase in the specific energy content of the high-voltage pulse capacitors used.

At present, the capacitive accumulator of electric power is a block containing three parallel connected high-voltage pulse capacitors for a working voltage of 30 kV and with a rated capacity of 0.8 μF each. The specifications of the existing high-voltage pulse capacitors for downhole devices are presented in Table 1.

A combined paper–film dielectric impregnated with castor oil is utilized in the capacitor structures.

Comparing the performance of the IKP-30-0.8 SF 4M.05.000 and IKP-30-0.8 SF 100.05.000 capacitors, we notice that the improvement of the capacitor structure, using the SF 100.05.000 as an example, permitted the capacitor specific accumulated power to be

Specifications of high-voltage pulse capacitors for downhole devices

Capacitor type	W_{sp} , J/dm ³	Operating conditions				Mass, kg	Maximum temperature, K	Overall dimensions, mm
		T , μs	Δ	f , Hz	I_m , kA			
IKP-30-0.8 SF 4M.05.000	24.5	8	10	0.2	5	45	353	$\varnothing 114$ $H_c = 1440$
IKP-30-0.8 SF 9.05.000	31.2	8	10	0.4	5	35	373	$\varnothing 114$ $H_c = 1432$
IKP-30-0.8 SF 100.05.000	39.1	8	10	0.25	10	28	373	$\varnothing 102$ $H_c = 1128$

increased from 24.5 to 39.1 J/dm³, i.e., approximately by 60%, the mass and clearance being decreased. Moreover, the operation temperature range is widened from 353 up to 373 K. The capacitor case structure ensures the needed strength under the influence of an external hydrostatic head of 50 mPa.

Solution of the problem of creating a small-sized accumulator was attempted before [1,2] by the location in one cylindrical case of several separate capacitors [1]. Circular capacitors with concentric winding, encapsulated with epoxide resin, are connected in series in the cylindrical case, flooded by a liquid dielectric. With an increase in temperature inside the case, the liquid dielectric is discharged into the environment through the compensating device valve. The complexity of this block of accumulators and its low operational reliability are the shortcomings of this construction.

In [2], with the aim of simplifying the accumulator block structure, separate capacitors, manufactured in rectangular cases, are placed in the cylindrical casing. The temperature change in the liquid dielectric volume is compensated with the help of an additional thin-walled case having a rectangular cross section. Irrational use of the power accumulator block case volume, not permitting high quantities of specific stored power to be ensured, is the drawback of this construction.

The further improvement of high-voltage pulse capacitors for downhole devices was carried out with the aim of ensuring capacitor electric reliability, structure tightness under the conditions of the external hydrostatic pressure, and compensation of the temperature change in the volume of the impregnating dielectric, leading to an insignificant growth in the specific accumulated power in comparison with the existing capacitor constructions for borehole devices.

Important results in the area of increasing the specific stored power of high-voltage pulse capacitors for borehole devices were obtained due to the transition from a paper-film dielectric impregnated with castor oil to a working dielectric based on polymeric films impregnated with a low-viscosity dielectric fluid [3].

Thus, TOO Geokart (Sarov, Russia) in collaboration with AO Elkond (St. Petersburg, Russia) created pre-production models of a high-voltage pulse capacitor for borehole devices for a rated voltage of 35 kV and with a rated capacity of 1.3 μ F. The capacitor comprises a metal pipe 1200 mm in length and 102 mm in outer diameter, in which cylindrical sections wound of a three-layer film dielectric impregnated with polybutene oil are located in series. The shortcoming of this capacitor is that its range of operating temperatures is from 233 to 313 K; that is, it cannot be utilized in the treatment of oil wells.

Work on creation of high-voltage pulse capacitors on the basis of a film dielectric for downhole devices operating at an environment temperature from 373 K with possible growth up to 398 K is being conducted at the Institute of Impulse Processes and Technologies of the National Academy of Sciences of Ukraine. The creation of such capacitors necessitated a complex of theoretical and experimental studies on the estimation of the prospects for increasing the specific power characteristics and resource of capacitors based on film dielectrics, on the search for and selection of dielectric systems reliably ensuring the operation of capacitors in accordance with the resource and operating conditions, and on the effect of construction materials and electrically stable gases on the electrophysical characteristics of liquid dielectrics operating under the conditions of strong electric fields. As a result, the admissible values of the working electric intensity in the dielectric of capacitor sections in accordance with the resource and operating conditions have been determined, the technological peculiarities of production of capacitors with film dielectrics have been identified, and regimes of thermal vacuum drying and impregnation have been selected [4–7].

As a result of the research conducted, a test specimen of a high-voltage pulse capacitor for a rated voltage of 30 kV and with a rated capacity of 1.2 μ F for a capacitor case length of 1158 mm, a diameter of 102 mm, and a resource of 4×10^5 charges–discharges intended for operation at an environment temperature up to 373 K and an external hydrostatic head up to 50 mPa has been created. The use of this capacitor in the block of capacitive energy accumulators of the existing Skif downhole electrical hydropulse installation will allow the number of capacitors to be decreased from three to two.

In addition, construction variants of capacitors with a similar function for a rated voltage of 30 kV with rated capacities of 2.4 and 2.7 μ F and an expected resource of from 10^5 to 3×10^5 charges–discharges depending on the type of dielectric used have been worked out. A film dielectric (a polypropylene–polyethylene terephthalate or polyethylene terephthalate dielectric) impregnated with polymethylsiloxane fluid is used in the capacitor constructions.

REFERENCES

1. USSR Inventor's Certificate no. 127736, *Byull. Izobret.*, 1960, no. 8.
2. Knyzhevskii, Yu.M., Guetskii, V.A. and Kireev, A.P., Submersible unit of capacitors, USSR Inventor's Certificate no. 875490, *Byull. Izobret.*, 1981, no. 39.
3. Grebennikov, I.Yu., Gun'ko, V.I., Onishchenko, L.I. and Shvets, I.S., Advent of energy capacitive accumulators for downhole electrical hydropulse devices, *Materialy XII*

- Mezhdunar. nauch. shkoly-seminara "Fizika impul'snykh razryadov v kondensirovannykh sredakh"* (Proc. XII Int. Sci. School-Seminar "Physics of Pulse Discharges in Condensed Media"), Nikolaev, 2005, pp. 159–160.
4. Onishchenko, L.I., Gun'ko, V.I. and Grebennikov, I.Yu., Advent of Energy Capacitive Accumulators for Down-hole Electrical Hydropulse Devices, *Trudy III Mezhdunar. konf. "Elektricheskaya izolyatsiya-2002"* (Proc. III Intern. Conf. "Electric Isolation-2002"), Nestor, 2002, p. 201.
 5. Gun'ko, V.I., Grebennikov, I.Yu., and Schupak, I.V., Investigation of Characteristics of Capacitor Working Dielectric under the Influence of Environmental Temperature up to 110°C, *Elektrotehnika*, 2002, no. 8, pp. 45–48.
 6. Onishchenko, L.I., Gun'ko, V.I., Grebennikov, I.Yu., et al., On Increase of Specific Power Characteristics and High-voltage Pulse Capacitors, *Elektron. Obrab. Mater.*, 2004, no. 5, pp. 66–69.
 7. Grebennikov, I.Yu., Prediction of the Expected Average Resource of High-voltage Pulse Capacitors with Film Dielectric Depending on Operational Conditions, Grebennikov, I.Yu., Gun'ko, V.I., Dmitrishin, A.Ya., et al., Eds., *Materialy XII Mezhdunar. nauch. shkoly-seminara "Fizika impul'snykh razryadov v kondensirovannykh sredakh"* (Proc. XII Int. Sci. School-Seminar "Physics of Pulse Discharges in Condensed Media"), Nikolaev, 2005, pp. 125–127.

OPERATING
EXPERIENCE

Gettering of Gold by Samarium and Gadolinium in Silicon

D. E. Nazayrov

Mirzo Ulugbek Uzbekistan National University, Vuzgorodok, Tashkent, 700174 Republic of Uzbekistan

Received December 22, 2006

Abstract—For the first time, by the methods of tracer atoms, autoradiography, isothermal relaxation of capacity and current, and measurement of conductivity and Hall effect, an effective gettering of gold in silicon was found at combined or sequential diffusion of the rare-earth elements samarium or gadolinium in silicon, in its near-surface layers, where there is a region of high concentration of the IIIA group element, samarium or gadolinium, as well as in the bulk silicon.

DOI: 10.3103/S1068375507030143

It is known that in preparation of semiconductor devices, for semiconducting silicon purification from quick-diffusing impurities both dissolved in bulk and penetrating from the surface in the process of diffusion annealing, the gettering technique is widely applied, that is, use of region of high concentration of elements of the III and V groups, mainly phosphorus and boron, as well as other elements in the near-surface regions of initial silicon plates. This leads to a significant decrease in the content of uncontrollable quick-diffusing impurities in silicon plates and, as a consequence, to an increase in the lifetime of minority charge carriers and to improvement in the diode characteristics of p - n transitions [1–3].

It was found in [4] that rare-earth elements (REE) deposited on a silicon surface in the diffusion annealing process serve as a getter of quick-diffusing impurities both available in the bulk and penetrating from the surface.

In the present work, we study the possibility of gettering of quick-diffusing gold impurity in silicon by virtue of the REEs samarium and gadolinium. The choice of samarium and gadolinium is determined by their low coefficients of diffusion in silicon ($D \sim 10^{-13} \text{ cm}^2 \text{ s}^{-1}$ at $T = 1200^\circ\text{C}$) [5–7], providing shallow penetration of samarium and gadolinium in the silicon plate bulk for the diffusion annealing time that satisfies the requirements on the choice of impurity, that is, the material being used in practice as a getter.

Two series of experiments were performed. In the first series, which included experiments on gettering of gold dissolved in the bulk, the samples were preliminarily uniformly doped with quick-diffusing gold impurity [8], then a metal layer of samarium or gadolinium was sputtered on one of large surfaces and subjected to annealing.

In the second series of experiments on gettering of gold penetrating the bulk during heat treatment, one of the large impurity-free silicon surfaces was sputtered

with gold first and then with samarium or gadolinium. Control samples without gold, samarium, or gadolinium, as well as samples with the surface sputtered only with gold, were available.

Doping was carried out by diffusion in air for 2 h at a temperature of $T = 200^\circ\text{C}$. Silicon samples of KEF-15 brand with orientation $\langle 100 \rangle$ and typical dimensions of $20 \times 10 \times 1 \text{ mm}$ were used for investigation. Before sputtering of impurities of both gold and samarium, as well as gadolinium, for removal of uncontrollable impurities from the silicon surface, the samples were successively washed in toluene, acetone, aqua regia, and $\text{H}_2\text{O}_2 : \text{HCl}$ mixture, and distilled water. The control samples were annealed under the same conditions.

After gold diffusion in silicon, which was carried out in air at 1200°C for 2 h, the samples were washed in HF, $\text{H}_2\text{O}_2 : \text{HCl}$, and H_2O ; such a washing usually allows nearly complete removal of the diffusion source remaining on the sample surfaces; thereupon a layer up to $150 \mu\text{m}$ thick was removed from the samples by chemical etching. Then samarium or gadolinium was sputtered on one of these surfaces, and diffusion annealing in air was carried out at 1200°C for 2 h. Then the samples again were washed in HF, $\text{H}_2\text{O}_2 : \text{HCl}$, aqua regia, and H_2O in order to remove an oxide layer and nondiffusing diffusant.

The profile of charge carrier concentration was determined by the method of etch removal of thin layers in a solution of $1\text{HF} : 40\text{HNO}_3$ and by measurement of the conductivity and the Hall effect. Complete ionization of impurities in silicon was assumed; that is, it was considered that concentration of impurities of gold, samarium, and gadolinium $c(x)$ is equal to the charge carrier concentration $n(x)$ or $p(x)$: $c(x) = n(x)$ or $p(x)$.

The thickness of the removed layers was determined by weighing the sample on a VLR-20 balance and was varied in the range of 0.1 – $10 \mu\text{m}$. Electric measurements carried out at several points of the surface

showed a uniform distribution of the impurity in the sample section and absence of second phase inclusions.

The charge carrier concentration $n(x)$ and $p(x)$ was determined by the formula

$$n(x) \text{ or } p(x) = \frac{1}{e} \frac{\left(\frac{d\sigma_s}{dx}\right)^2}{\frac{d}{dx}(R_s \sigma_s^2)}. \quad (1)$$

Here R_s is the measurable (effective) Hall coefficient, σ_s is the surface conductivity, and e is the electron charge. Let us note that the formula is given in work [9] in a more general form, taking into account difference of the Hall and drift mobilities.

Series of investigations based on tracer atoms of gold ^{198}Au , ^{153}Sm , and ^{159}Gd were carried out too. Activation of atoms of gold, samarium, and gadolinium was realized at the Konstantinov Institute of Nuclear Physics, St. Petersburg, Russian Academy of Sciences. Isotopes of ^{198}Au , ^{153}Sm , and ^{159}Gd were sputtered on the sample surface. After diffusion and subsequent washings, during layer removal, radiography was performed to control doping uniformity. The sample activity was measured on against a low background on an UMF-1500M with an SBT-11 β -counter and on a BDBSZ-IeM with an NaI(Tl) scintillation counter. The γ -spectra of ^{198}Au , ^{153}Sm , and ^{159}Gd were identified on an AI-1024 pulse analyzer.

The electric measurements have shown that the silicon samples doped only with gold (Fig. 1 (curve 1)) become highly ohmic under the above-mentioned conditions. As is known [8], gold belongs to the group of impurity elements characterized by high values of the diffusion coefficient and low solubility in silicon. Gold in n -type silicon has two deep energy levels (DL) in the bandgap: $E_c - 0.54$ eV and $E_v + 0.35$ eV [10]; the level $E_c - 0.54$ eV is an acceptor compensating the initial material at high concentrations.

For finding the reasons why the resistivity of the n -Si(Au) sample increases, on the plates, the Schottky barrier was created by gold sputtering in vacuum at the substrate temperatures $<100^\circ\text{C}$ and the technique of isothermal relaxation of current for compensated samples was applied [11].

It was found that for n -Si(Au) samples, dependence $\tau(T)$ coincides with that for the deep acceptor level $E_c - 0.54$ eV in the presence of gold [12] (Fig. 2). This shows that the decrease in the charge carrier concentration in the n -Si(Au) samples is caused by the presence of gold in bulk silicon.

Dependence of the resistivity and charge carrier concentration on the profile of gold introduced into the n -Si(Au) samples is in good agreement with the data of [8, 13, 14], again showing the compensating role of the gold acceptor level (Fig. 1 (curve 1)).

Figure 1 (curve 1) shows the typical distribution of the charge carrier concentration in thickness $n(x)$ of one

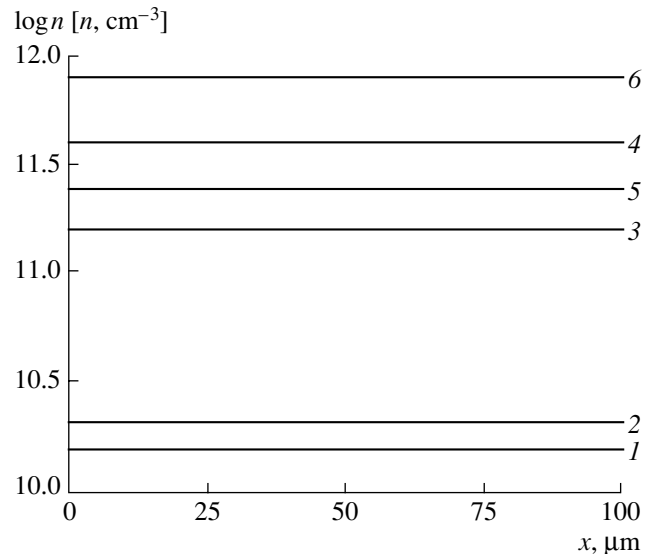


Fig. 1. Charge carrier concentration distribution $n(x)$ in the sample thickness after removal of the ~ 150 μm layer: (1) in the Si(Au) samples; (2) in the control Si(Au) samples without a layer of Sm or Gd after removal of the ~ 150 μm layer and repeated annealing at $T = 1200^\circ\text{C}$, $t = 2$ h; (3) in the Si(Sm + Au) samples after repeated annealing at $T = 1200^\circ\text{C}$, $t = 2$ h, with samarium layer, sequential diffusion with preliminary removal of the ~ 150 μm layer after gold diffusion; (4) in the Si(Gd + Au) samples after repeated annealing at $T = 1200^\circ\text{C}$, $t = 2$ h with gadolinium layer, sequential diffusion with preliminary removal of the ~ 150 μm layer after gold diffusion; (5) in the Si(Sm + Au) samples under combined diffusion; (6) in the Si(Gd + Au) samples at combined diffusion.

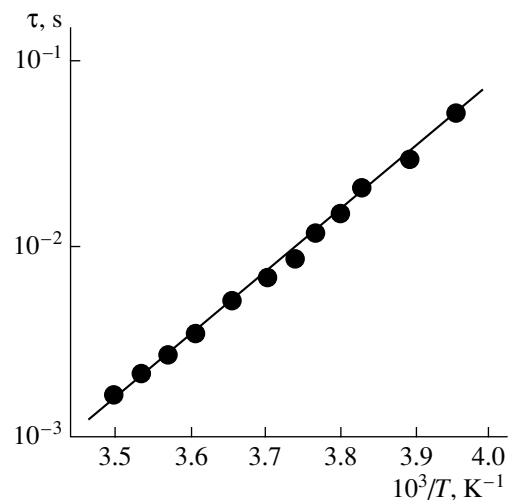


Fig. 2. The dependence $\tau(T)$ for a typical Si(Au) sample. The points denote experiment. The solid curve shows the dependence for DL $E_c - 0.54$ eV caused by gold in silicon [12].

of the Si(Au) samples obtained by sequential removal of layers. Figure 1 (curves 3, 4) corresponds to $n(x)$ distributions of the Si(Au) samples with layers of samarium and gadolinium sputtered on the surface after pre-

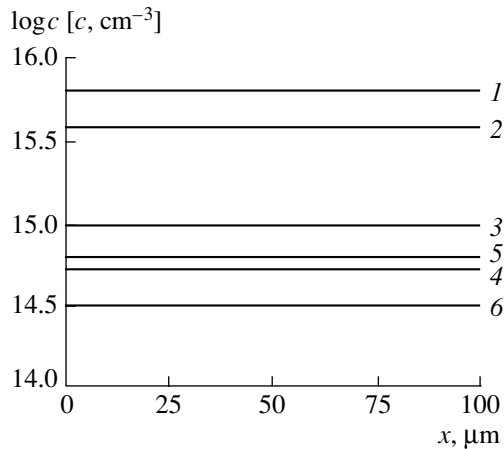


Fig. 3. Concentration distribution of gold $c(x)$ in silicon (after removal of the $\sim 150 \mu\text{m}$ layer): (1) in silicon at $T = 1200^\circ\text{C}$, $t = 2 \text{ h}$; (2) in the control Si(Au) samples without layers of Sm and Gd after removal of the $\sim 150 \mu\text{m}$ layer and repeated annealing at $T = 1200^\circ\text{C}$, $t = 2 \text{ h}$; (3) in the Si(^{198}Au) samples after repeated annealing at $T = 1200^\circ\text{C}$, $t = 2 \text{ h}$ with the samarium layer, with preliminary removal of the $\sim 150 \mu\text{m}$ layer after gold diffusion; (4) in the Si(^{198}Au) samples after repeated annealing at $T = 1200^\circ\text{C}$, $t = 2 \text{ h}$ with gadolinium layer, with preliminary removal of the $\sim 150 \mu\text{m}$ layer after gold diffusion; (5) in the Si($^{198}\text{Au} + \text{Sm}$) samples at combined diffusion at $T = 1200^\circ\text{C}$, $t = 2 \text{ h}$; (6) in the Si($^{198}\text{Au} + \text{Gd}$) samples at combined diffusion at $T = 1200^\circ\text{C}$, $t = 2 \text{ h}$

liminary removal of layers from all sides up to $150 \mu\text{m}$ followed by thermal annealing at 1200°C for 2 h. Analysis of the $n(x)$ distribution in control silicon samples subjected to annealing at $T = 1200^\circ\text{C}$ for 2 h, taking into account the influence of heat treatment on the electric properties of silicon, has shown that after the first and repeated annealing, the resistivity and charge carrier concentration in the control samples changed insignificantly and the type of their conductivity remained unchanged.

It is seen from the given dependences that the charge carrier concentration in the Si(Au + Sm) and Si(Au + Gd) samples considerably exceeds the one in the Si(Au) samples. This $n(x)$ distribution may be due to the profile of the Au compensating impurity in the Si(Au + Sm) and Si(Au + Gd) samples.

Figure 3 (curve 1) shows the concentration distribution of gold in the Si(Au) samples obtained by the method of tracer atoms and sequential removal of layers. Figure 3 (curve 2) corresponds to the gold distribution in the control samples, without layers of samarium or gadolinium, after removal of the $\sim 150 \mu\text{m}$ layer and repeated annealing at $T = 1200^\circ\text{C}$ for 2 h. The charge carrier mobility and conductivity type in the bulk of the Si(Au) and Si(Au + Sm) samples, as well as of the Si(Au + Gd) ones, after removal of the $\sim 150 \mu\text{m}$ layer remain unchanged as in the initial samples, in a satisfactory agreement with the data of [13].

From comparison of the given dependences $c(x)$, it is seen that repeated heat treatment leads to a decrease in the overall gold concentration in the bulk silicon and to an increase of this concentration by a factor of 1.5–2, apparently due to gold exodiffusion and gettering, that is, extraction of gold atoms by the surface. Fig. 3 (curve 3) corresponds to the gold distribution in the Si(Sm + Au) samples and Fig. 3 (curve 4), to the gold distribution in the Si(Gd + Au) samples.

One can see that in the presence of samarium and gadolinium the gold concentration in the silicon bulk decreases significantly. When gold diffusion is realized in combination with samarium or gadolinium, when one of the large impurity-free silicon surfaces is sputtered first with gold and then with samarium or gadolinium, a limited penetration of gold in the sample depth is observed; that is, there “purification” takes place, gettering of the silicon bulk from gold (Fig. 1 (curves 5, 6); Fig. 3 (curves 5, 6)).

As is seen from Figs. 1 (curves 3–6) and 3 (curves 3–6), gadolinium getters gold in silicon more efficiently than samarium. On the basis of isotopes of ^{153}Sm and ^{159}Gd , we have found that at $T = 1200^\circ\text{C}$, samarium and gadolinium in silicon have diffusion coefficients of $\sim 10^{-12} \text{ cm}^2 \text{ s}^{-1}$ and $\sim 3 \times 10^{-13} \text{ cm}^2 \text{ s}^{-1}$ and surface concentrations of $C_0 \sim 3 \times 10^{18} \text{ cm}^{-3}$ and $C_0 \sim 10^{19} \text{ cm}^{-3}$, respectively, coinciding with the conclusions of works [6, 7]; the penetration depth for samarium and gadolinium in our samples is about $5 \mu\text{m}$; samarium and gadolinium in silicon exhibit a shallow acceptor nature. The charge carrier mobility in diffusion layers Si(Sm) and Si(Gd) is $\sim 140\text{--}250 \text{ cm}^2/(\text{V s})$ and decreases with increasing concentration of samarium and gadolinium in silicon. We have not found any deep levels characteristic of samarium and gadolinium in silicon by the methods of isothermal relaxation of capacity and current. The concentration of the deep level bound with gold strongly correlates with the presence or absence of profiles of samarium or gadolinium in the near-surface regions of silicon; that is, the presence of these impurities in the near-surface region efficiently decreases the concentration of the $E_c - 0.54 \text{ eV}$ deep acceptor level caused by gold [12].

It is shown in work [15] that critical concentrations for the appearance of the second phase inclusions in the silicon single crystal doped with REE samarium and gadolinium during growth are $\sim 3.9 \times 10^{18} \text{ cm}^{-3}$ and $\sim 2.4 \times 10^{18} \text{ cm}^{-3}$, respectively, and limits of their doping are equal to $\sim 7.1 \times 10^{18} \text{ cm}^{-3}$ and $\sim 1.4 \times 10^{19} \text{ cm}^{-3}$, respectively. Using the analysis of the data of [6, 7, 15], one may suppose that at the given temperature, gadolinium impurities that in silicon have solubility values higher by a factor of 3–4 than in samarium and a probability of the second phase inclusions in the near-surface layers higher by a factor of 3, getter gold atoms more efficiently than samarium.

Thus, our results show effective gold gettering in silicon under combined or sequential diffusion of samar-

ium or gadolinium in silicon, in its near-surface layers, where there is a region of high concentration of IIIA group elements, samarium or gadolinium, as well as in bulk silicon. Using the radiographic method, a local gettering was also found; that is, gold extraction from the bulk by virtue of a layer of samarium or gadolinium locally sputtered on a silicon surface. Layer-by-layer radiography [16, 17] has shown that during annealing, gold is removed from the local region under the layer of samarium or gadolinium. Applying the method of frequency dependence of the rectified current in the samples under study, it was found that under samarium diffusion in silicon doped with gold, the lifetime values for minority carriers in the bulk increase by a factor of 5–10, from the initial ones of 0.1–0.5 μs up to 1–5 μs after gettering.

The results are explained by the gettering effect (extraction) generated by a layer of rare-earth elements, samarium and gadolinium, on the silicon surface, and by the near-surface layer, where second phase inclusions may be formed, that is, various silicide formations [18, 19], where the solubility of gold may have higher values than in silicon, as well as by elastic tensions appearing in the near-surface layers and silicides, which may be sources of the motive force of gold diffusion.

ACKNOWLEDGMENTS

The author would like to thank G.S. Kulikov, R.Sh. Malkovich, and V.A. Didik for consultations and helpful remarks concerning the experiments, and S.I. Vlasov for fruitful discussion of the experimental results.

REFERENCES

1. Reivi, K., *Defekty i primesi v poluprovodnikovom kremnii* (Defects and Impurities in Semiconducting Silicon), Moscow: Mir, 1984.
2. Malkovich, R.Sh. and Pokoeva, V.A., Diffusion and Solvability of Gold in Strongly Alloyed Silicon, in *Fizika struktury i svoistva tverdykh tel* (Structure Physics and Properties of Solid Bodies), Kuibyshev: Kuibyshev. Gos. Univ., 1984, pp. 3–17.
3. Abdurakhmanov, K.P., Daliev, Kh.S., Kulikov, G.S., Lebedev, A.A., Nazirov, D.E., and Utamuradova, Sh.B., Investigation of Iron Interaction with Other Elements in Silicon, *Fiz. Tekh. Poluprovodn. (S.-Peterburg)*, 1986, vol. 20, issue 1, pp. 185–186.
4. Malkovich, R.Sh. and Nazyrov, D.E., Gettering of Quick-diffusing Impurities in Silicon by Rare-earth Elements, *Pis'ma Zh. Tekh. Fiz.*, 1988, vol. 15, issue 4, pp. 38–40.
5. Nazyrov, D.E., Regel', A.R., and Kulikov, G.S., Silicon Doped with Rare-Earth Elements, *Preprint of Ioffe Physical-Technical Inst., Russ. Acad. Sci.*, Leningrad, 1987, no. 1122, p. 56.
6. Zainabidinov, S., Nazyrov, D.E., and Bazarbaev, M.I., Diffusion, Solubility, and Electric Properties of Samarium and Ytterbium in Silicon, *Elektron. Obrab. Mater.*, 2006, no. 4, pp. 90–92.
7. Nazyrov, D.E., Study of Diffusion, Solubility, and Electric Properties of Gadolinium in Silicon, *Elektron. Obrab. Mater.*, 2006, no. 6, pp. 76–79.
8. Boltaks, B.I., Bakhadyrkhanov, M.R., Gorodetskii, S.M., and Kulikov, G.S., *Kompensirovannyy kremnii* (Compensated Silicon), Leningrad: Nauka, 1972.
9. Baron, R., Shifrin, G.A., Marsh, O.J., and Mayer, J.W., Electrical Behavior of Group III and V Implanted Dopants in Silicon, *J. Appl. Phys.*, 1969, vol. 40, no. 9, pp. 3702–3719.
10. Berman, L.S. and Lebedev, A.A., *Emkostnaya spektroskopiya glubokikh tseftrov v poluprovodnikakh* (Capacity Spectroscopy of Deep Centers in Semiconductors), Leningrad: Nauka, 1981.
11. Berman, L.S. and Vlasov, S.I., Determination of Energy of Activation of Deep Centers in Diodes of Overcompensated Semiconductor by Capacity Method, *Fiz. Tekh. Poluprovodn. (S.-Peterburg)*, 1978, vol. 12, issue 3, pp. 559–561.
12. Berman, L.S., Vlasov, S.I., and Morozov, V.F. Identification of Residual Deep Impurities in Semiconductors and Semiconductor Devices by Method of Capacity Spectroscopy, *Izv. Akad. Nauk SSSR, Ser. Fizika*, 1978, vol. 42, issue 6, pp. 1175–1178.
13. Boltaks, B.I., Kulikov, G.S., and Malkovich, R.Sh., Gold Influence on Electric Properties of Silicon, *Fiz. Tverd. Tela*, 1960, vol. 2, issue 1, pp. 181–191.
14. Badalov, A.Z. and Shuman, V.B., Influence of Complex Formation on Dissociation of Au–Si Solid Solution, *Fiz. Tverd. Tela*, 1970, vol. 12, issue 7, pp. 2116–2122.
15. Mil'vidskii, M.G., Karpov, Yu.A., Turovskii, B.M., Voronkov, V.V., and Kovaleva, T.A., Single Crystalline Silicon Doped with Rare and Transition Elements, in: *Legirovannyye poluprovodnikovyye materialy* (Doped Semiconductor Materials), Moscow: Nauka, 1985, pp. 97–102.
16. Boltaks, B.I., *Diffuziya v poluprovodnikakh* (Diffusion in Semiconductors), Moscow: GIFML, 1961.
17. Shishiyanu, F.S., *Diffuziya i degradatsiya v poluprovodnikovyykh materialakh priborov* (Diffusion and Degradation in Semiconductor Materials of Devices), Chisinau: Stiinta, 1978.
18. Koleshko, V.M., Belitskii, V.F., and Khodin, A.A., Thin Films of Silicides of Rare-Earth Metals, *Poverkhnost'. Fiz., Khim., Mekh.*, 1986, vol. 10, issue 1, pp. 93–96.
19. Murarka, S.P., *Silicides for VLSIC Applications*, New York: Academic, 1983.

**OPERATING
EXPERIENCE**

Determining the Force and Pressure at the Extrusion of Union Nuts from Cylindrical Semiproducts¹

C. Bejinariu^a, M. Susan^a, P. G. Dumitras^b, and S. L. Toma^a

^a Asachi Technical University, Iasi, Romania, 59 Blv. D. Manjeron, Iasi, Romania

^b Institute of Applied Physics, Academy of Sciences of Moldova, 5 Academiei Str., Chisinau, MD-2028 Republic of Moldova

Received November 8, 2006

Abstract—The paper aims to determine by experiment the total force and pressure of deformation as a function of the punch stroke and the deformation degree at the indirect extrusion of steel union nuts from cylindrical semiproducts.

DOI: 10.3103/S1068375507030155

1. GENERAL CONSIDERATIONS

The extrusion force is the most complex and important parameter of the extrusion technological process determining the applicability of this procedure. The value of the extrusion force is used especially for the development of equipment and designing tools.

The extrusion force depends on a number of parameters. Among them, the following ones are the most important: the deformation degree and rate, the flow curve of the processed steel, friction between the tool and material, sizes of the extended profile, the shape and sizes of the semiproduct, the temperature variation during the process, and physicomechanical properties and structural inhomogeneity of the semiproduct material.

Though there are many analytical and experimentally determined relationships that allow the extrusion force to be calculated, none of them can take into account all the influences. So, the values of the extrusion force obtained using these relationships are only approximative. That is why researchers prefer to determine them by experiment.

The paper aims to determine by experiment the total force and pressure of deformation as a function of the punch stroke and the deformation degree at the indirect extrusion of steel union nuts from cylindrical semiproducts.

2. EXPERIMENTAL CONDITIONS

We used cylindrical samples of OLC 15 prepared using chemical phosphating and lubrication with molybdenum disulfide (Table 1).

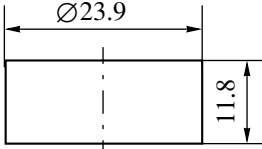
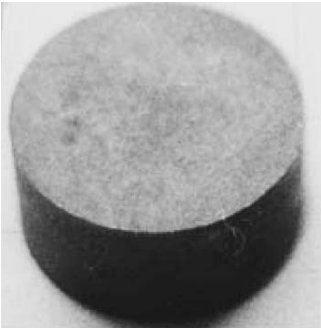
Extrusion was performed on a hydraulic press PH 200 using the extrusion device designed and patented by the authors (Fig. 1).

For force measurements, a load cell of 1000 kN was used, and for the punch stroke an inductive transducer was used.

Equipment for data acquisition and processing included

- 2100 SYSTEM tensometric amplifier;

Table 1

Semiproduct	Shape and sizes	Phosphated semiproducts
cylindrical		

¹ The text was submitted by the authors in English.

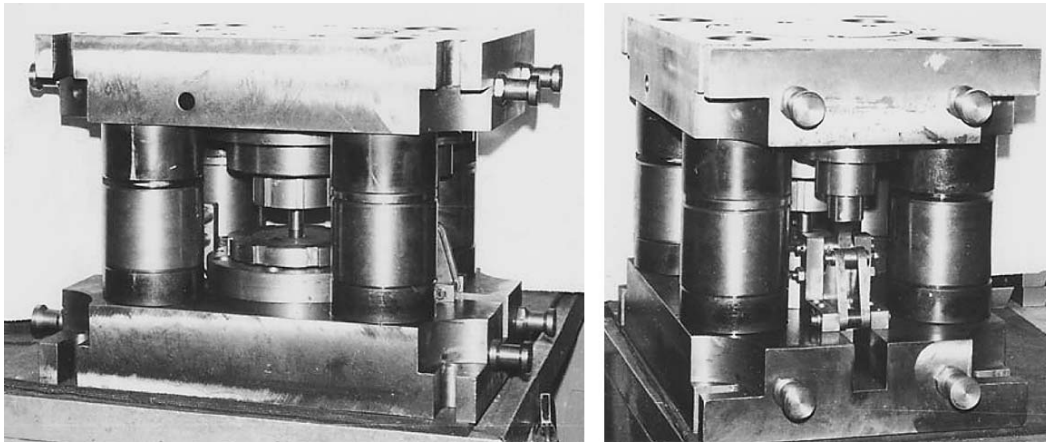


Fig. 1. Extrusion device.

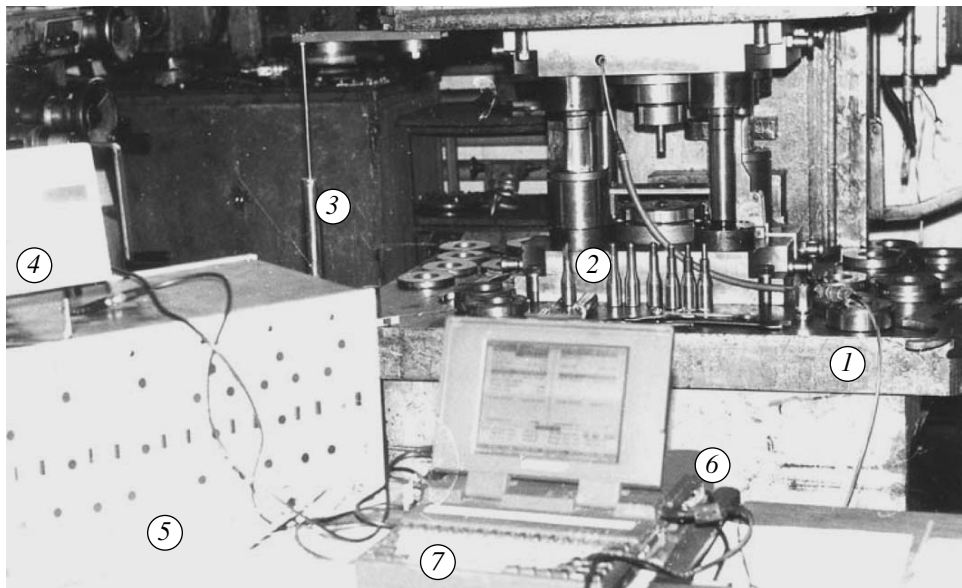


Fig. 2. General view of the installation for determining the extrusion force.

(1) Hydraulic press; (2) extrusion device; (3) displacement transducer; (4) tensometric amplifier; (5) electronic tensometer; (6) acquisition module; (7) laptop.

- movable 16-channel AT-2016 P/S data acquisition module;
- laptop;
- ESAM (Electronic Signal Acquisition Module) software with frequency up to 200000 acquisitions per second.

The equipment enables one to perform both the calibration of the transducers used and data acquisition.

For determining the extrusion force as a function of the punch stroke, the load cell was mounted inside the extrusion device. The displacement transducer was mounted between the fixed table and the moving table of the press (Fig. 2).

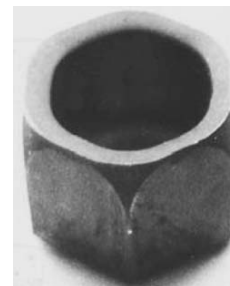


Fig. 3. A union nut piece.

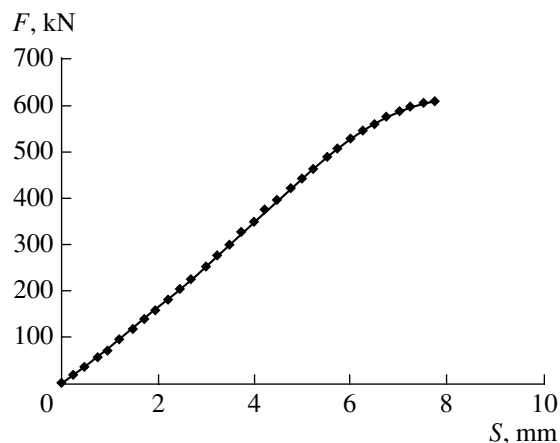


Fig. 4. Variation of the extrusion force vs. the punch course.

In the ESAM program, tests for measuring force–displacement dependences were developed using calibration factors determined previously. During the punch, the active stroke force–displacement dependences were measured with a frequency of 100 acquisitions/s.

3. EXPERIMENTAL RESULTS

After extrusion of semiproducts, union nut pieces were obtained (Fig. 3).

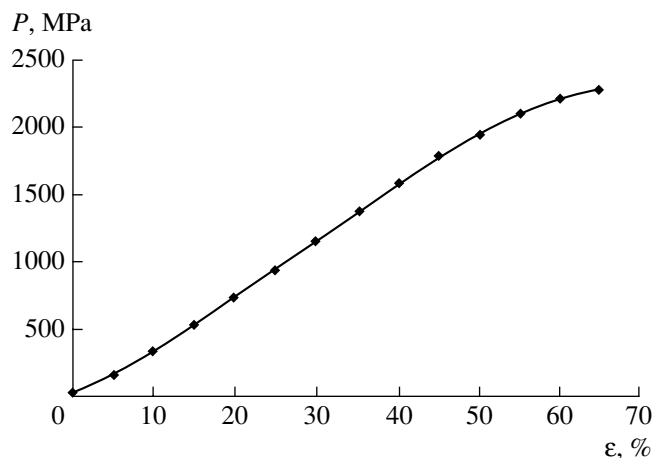


Fig. 5. Variation of the extrusion pressure vs. the conventional deformation degree.

Experimental data processing was performed using Microsoft Excel; the results are presented in Tables 2 and 3, where

s is the extrusion punch stroke measured during deformation;

ϵ is the conventional deformation degree calculated as $\epsilon = \frac{h_0 - h}{h_0} \times 100$ [%];

F is the extrusion force measured during the process;

Table 2

No.	Punch stroke s , mm	Force F , kN	No.	Punch stroke s , mm	Force F , kN
1	0.00	1.0	17	4.00	349.4
2	0.25	18.0	18	4.25	373.5
3	0.50	35.9	19	4.50	397.3
4	0.75	54.5	20	4.75	420.7
5	1.00	74.0	21	5.00	443.4
6	1.25	94.2	22	5.25	465.5
7	1.50	115.1	23	5.50	486.6
8	1.75	136.6	24	5.75	506.8
9	2.00	158.8	25	6.00	525.7
10	2.25	181.5	26	6.25	543.2
11	2.50	204.7	27	6.50	559.2
12	2.75	228.3	28	6.75	573.5
13	3.00	252.3	29	7.00	585.8
14	3.25	276.5	30	7.25	595.9
15	3.50	300.8	31	7.50	603.7
16	3.75	325.1	32	7.75	609.0

Table 3

No.	Deformation degree ϵ , %	Extrusion pressure P , MPa	No.	Deformation degree ϵ , %	Extrusion pressure P , MPa
1	0	23	8	35	1371
2	5	158	9	40	1580
3	10	323	10	45	1774
4	15	512	11	50	1946
5	20	717	12	55	2090
6	25	933	13	60	2199
7	30	1153	14	65	2268

p is the total extrusion pressure determined as the measured extrusion force divided by the area of the frontal punch surface.

The variation of the extrusion force vs. the punch stroke is shown in Fig. 4, and the variation of the extrusion pressure vs. the conventional deformation degree is presented in Fig. 5.

4. CONCLUSIONS

(1) In the case of indirect cold extrusion of union nuts, the diagram of the force variation vs. the punch stroke differs only slightly for different pieces.

(2) Deformation during the entire extrusion period occurs practically at the same pressure for a given deformation degree.

INFORMATION

Laser-Aided Manufacturing in Ukraine¹

V. S. Kovalenko

Laser Technology Research Institute, National Technical University of Ukraine, pr. Peremohy 37, Kiev, 03056 Ukraine

Received January 28, 2007

Abstract—Started in the early 1960s, R&D development in laser technology in Ukraine is still in progress in spite of some decline in 1990–1993 caused by drastic political and economic changes in the country. There are, indeed, some interesting and original results in all known industrial applications. Some of them are presented in this report. The international ties with colleagues and joint projects with copartners from different countries are becoming common practice. The significant intellectual potential and gained research and industrial experience serve as a basis for more than 40 years of academic activity in laser technology in the country. Graduates of the Laser Technology and Materials Science Department of the Kiev Polytechnic Institute (engineers, masters, PhD holders) are quite successful in their career both in Ukraine and in different countries of the world. Collaboration within the framework of the European Union as well as with different institutions in North America and Asian countries is increasing quite rapidly.

DOI: 10.3103/S1068375507030167

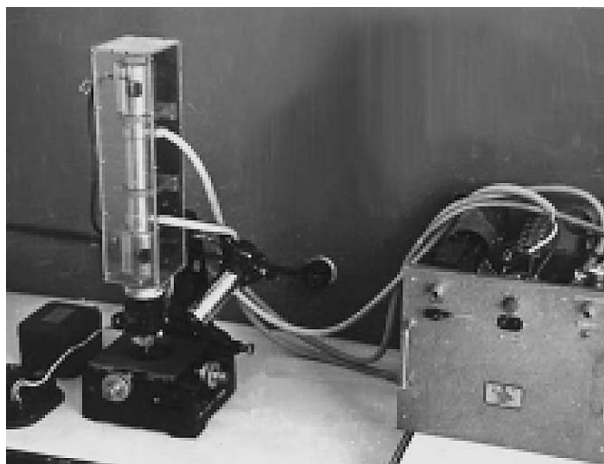
INTRODUCTION

Global economic developments present new challenges for human activity. The advent of information technologies, aerospace developments, new success in health care, new results in biotechnology, and other science and technology achievements are possible owing to, among others, fundamental changes in manufacturing science and possibilities to use new approaches in product development. Laser technology born in the middle of the last century continues to bring new challenges but also opens new horizons for scientists and manufacturers. It is impossible to imagine now globalization without laser technology, as it is impossible to imagine modern laser technology without globalization.

The first research activities in laser-aided manufacturing in Ukraine dated back to 1964 and were initiated at the Kiev Polytechnic Institute (now The National Technical University of Ukraine KPI), at the Paton Welding Institute, and at other institutions. There was a splash of interest in this advanced technology in the last two decades. The interesting feature of this process is the appearance of a number of small private organizations, different job shops, and the development of new R&D activity at a number of universities and research institutes (total around 50). Along with traditional industrial laser applications (cutting, surface treatment, welding, cladding, marking, cleaning, etc.), some new fields are emerging such as rapid prototyping, micro- and nanoprocessing, and development of new types of lasers.

R&D ACTIVITIES

The first industrial laser system based on the ruby laser was developed at KPI in 1964. It was installed on the universal tool microscope of the Karl Zeiss Co. and had an energy of only 2J per pulse (Fig. 1). Later, a series of different pieces of equipment were developed at the Laser Technology Laboratory of KPI based both on more powerful ruby laser and on Nd-glass, YAG, CO₂ and other lasers. The main research was conducted in the development of technologies of precise micro-hole piercing, spot welding, studying hardening effects, surface alloying possibilities, and micro cutting and marking.



First Ukrainian industrial laser system based on ruby laser for precise hole piercing, developed at LTL (KPI) in 1964.

¹ The text was submitted by the author in English.

At other institutions, some pieces of industrial laser systems manufactured in the former Soviet Union eventually appeared together with self-made experimental setups.

Laser hole piercing. The main problem in laser hole piercing was to get high quality and precision of the hole, which was dependent mainly on the amount of molten phase in the erosion products. To lessen this effect or to avoid the molten phase entirely, shorter pulses were used. Over the last two decades, the evolution was drastic—from milliseconds to microseconds, then to nanoseconds and picoseconds, and finally to femtoseconds.

Laser welding. This research is done to a large extent at the Paton Welding Institute, using mostly powerful CO₂ lasers. At LTRI, we are involved in studying joining of very delicate components like electronic device parts and different parts of medical instrumentation, which have gained wide popularity in recent years.

Promising results were achieved in joining parts made from plastic, ceramic, and composite materials. A good example of high efficiency of such joining is laser welding of diamond composite cutting segments to the steel body of disk saw for cutting stones without water cooling. Besides the latter advantage, the implementation of such joining process produces a significant savings of silver, used for traditional brazing of segments.

Laser hardening. For improvement of laser hole piercing, the great problem was to control the heat-affected zone (HAZ) and to make it minimal. The study of this zone demonstrated the ability to vary the parameters and dimensions of the zone in a wide range. The studied phase transformation phenomena and other different metallurgical effects in this zone brought to life the new applications of laser technology: welding, surface hardening, surface alloying, cladding, shock hardening, glazing (amorphization), etc.

The development of different hardening technologies created new possibilities to form regions with unique properties locally in the component and thus to improve the quality of the whole product. Thanks to laser processing, the wear resistance of cutting tools, moulds, dies, and different machine components increased by a factor of 3–6.

Cutting and material shearing. The first cutting applications were mainly connected with manufacturing small slots in different parts, with sharing brittle materials (like diamond crystals) using the scribing mechanism, with shearing silicon plates for solar elements using high-frequency pulse lasers, etc. The fundamental research of the cutting process with supporting gas helped to better understand the mechanism of material removal and of high-quality edge formation.

3D object forming. Thanks to information technology integration into laser processing, it became possible to develop the new technology of forming 3D

objects based on the principle of biological growth taken from nature. Known as rapid prototyping, this technology dispenses with moulds, dies, and other traditional expensive tools to manufacture components with complicated shape at very high productivity. Having started first from manufacturing components from polymer materials using stereo lithography, this technology now came to a new stage—the possibility to create components from metal, ceramic, or different composite materials.

The research was carried out by studying the influence of different working conditions on sintering quality, on crack formation, etc. Two schemes of process realization were developed and corresponding laser industrial systems were manufactured.

On the basis of research results in laser sintering, the technology of manufacturing thin diamond cutting tools has been proposed and is currently under more detailed investigation.

Micro- and nanomachining. Thanks to information technology integration into laser processing, it became possible to develop the new technology of forming 3D objects based on the principle of biological growth taken from nature. Known as rapid prototyping, this technology dispenses with moulds, dies, and other traditional expensive tools to manufacture components with complicated shape at very high productivity. Having started first from manufacturing components from polymer materials using stereo lithography, this technology now came to a new stage—the possibility to create components from metal, ceramic, or different composite materials.

Marking and engraving. This technology became widespread for many fields of industry thanks to very high productivity and quality of the process. A unique application is marking inside a material transparent to a laser beam using 3D laser scanning.

Sheet material deformation. The possibility to control the heating process and thus the resulting thermal deformation of sheet material by using laser irradiation enabled the development of the new technology for forming components of complicated shape from sheet metal, plastic, or other materials. It became possible to deform the material according to the given program without any traditional mechanical deforming technique using only a scanning laser beam.

In addition to these research activities, the possibilities to use laser heat treatment to increase the rigidity of thin sheet components is also being studied.

Combined or hybrid processing. Taking into account that the laser itself is a very low efficiency energy transformer, different ways of additional energy supply into the working zone were proposed. The most efficient was the direct electric energy addition to the concentrated laser energy. Depending on the method of this additional energy supply, different techniques were developed:

- Electrolaser hole piercing;
- Arc-augmented laser welding;
- Laser cladding with electromagnetic agitation;
- Laser alloying in electromagnetic field;
- Laser-electrochemical processing;
- Plasma-laser processing.

Additional mechanical energy is applied to stimulate plastic deformations to control the thermal stressed material state:

- Laser ultrasonic hardening;
- Laser plastic deformation hardening, etc.

Process simulation. This stage of laser technology is quite well represented. Different models were successfully developed based mainly on heat conduction theory and presenting the “heat history” of the irradiated materials. Different limitations are considered making these models quite adequate for the simple cases of laser processing. For complicated cases when processing is connected with evaporation, explosion, plasma formation, ablation mechanism, etc., such physical models do not “work” properly and cannot be used at the industrial level.

Mathematical statistical models based on experimental results were developed for industrial use, but they are usually adequate only for some specific factor space and may not always be extrapolated to more complicated working conditions.

LASERS IN INDUSTRY

The developed technology and equipment are quite widely used at different plants—Arsenal, Bolshevik, AVIANT (Kyiv), Malysheva Plant, Tractor Plant (Kharkiv), AvtoKraz (Kremenchug), and many others. At these plants, the Soviet made CO₂ lasers and Nd:YAG lasers are mainly used for component welding, hardening, cladding, material cutting, etc. Recently, more than 60 new industrial laser systems have been bought by companies from foreign manufacturers—Trumpf, Bistronic, Rofin Sinar, etc. A number of small private organizations and different job shops have appeared in the market in the last few years which specialize in sheet material shearing, welding, component restoration by cladding, marking and engraving, etc.

Different types of industrial laser systems are widely used in industry to manufacture precise holes in the range of a few microns up to 1–2 mm in diameter with very high productivity.

Among nontraditional applications, one should be mentioned connected with treatment of highly radioactive materials—the study of opportunities to use a robotic laser system to disintegrate the Object Shelter of the Chernobyl Atomic Station.

ACADEMIC PROGRAM

From the very beginning of the laser era, activities on the development of academic programs in laser technology were initiated at KPI. Thus, at KPI, the first graduates of this course received their engineering diploma in 1966–1967 from the Mechanical Engineering Department. This course has the official status of the new specialty named “Technology and Equipment for Laser Processing” and created in 1984. The corresponding academic program started first in the FSU and in Ukraine at KPI in Kyiv and at the Bauman Institute in Moscow.

In recent years, the academic program has been adapted to the Bologna Agreement concept, the main goal of which is the integration of the national education systems into the European and global one.

From that time up to now, more than 1000 engineers and masters (from both Ukraine and 32 other countries) in laser technology have graduated from KPI. In the last decades, 27 PhD theses and 6 Dr. Sci. theses from researchers from different countries have been successfully defended at KPI as well.

INTERNATIONAL COLLABORATION AND INTEGRATION INITIATIVES

The international collaboration in the field of laser technology has improved significantly over the last decade. Different mechanisms are involved in stimulating such moves. Besides bilateral agreements on scientific collaboration between Ukraine and different countries, there are a number of direct ties between universities and laser centers (for example, the LTRI has such agreements with Okayama University, Japan; Ohio State University, USA; Zhezhiang University, China; etc.). A number of projects are financed by NATO, by different institutions of the EU (INTAS, EUREKA, etc.), and by the Scientific and Technological Center of Ukraine (STCU). By the way, the STCU is sponsoring projects financed either from three combined sources—United States, Canada, and EU—or from separate sources. LTRI developed the STCU project no. 2379 “Laser 3D Prototypes Forming from Powder Metal and Ceramic Materials,” financed by the United States, Canada, and EU in 2005 (copartners from United States, Canada, Netherlands, Italy). The technology and laser industrial system was recommended for commercialization in 2005. In 2006, another STCU project (no. 3350) was approved with financing from the EU: “Development of New Design Medical Stents and Their Manufacturing Using Laser Radiation” (copartners from United States, Canada, Netherlands, Belgium, and Portugal).

It is obvious that globalization goes parallel with the integration process. We witness such integration in every field of human activity, in different regions, in America, in Europe, and in Asia. Ukraine as a country located in the very geographical center of Europe is try-

ing to be integrated in the European community and supports different integration initiatives.

Prof. V. Kovalenko (NTUU) and Prof. A. Grabchenko (KhNTU) was invited by EU officials as coordinators from Ukraine to develop the National ManuFuture Technological Platform. On the basis of results achieved and experience gained in advanced technology R&D activity, such ManuFuture Technological Platform of Ukraine was developed recently and proposed for integration in the EU ManuFuture Platform. Laser-aided manufacturing is considered as a key technology of this concept.

In spite of chronic financial problems, experts in laser technology from Ukraine are beginning to participate quite regularly in different international professional institutions, such as LIA, CIRP, IEEE, LEOS, LAS, etc., and their events: ICALEO, ISEM, CIRP General Assemblies, etc. I would like to stress that the ICALEO event is usually considered to be a real global congress in laser technology.

Ukrainian experts are quite active as referees in the LIA's *Journal of Industrial Laser Applications* and as contributors to the *LIA Handbook of Laser Materials Processing*.

A few international laser conferences have been organized in recent years in Ukraine. One of them is becoming traditional—International Conference on Laser Technology in Welding and Material Processing (LTWMP), organized by the Paton Welding Institute and by the LTRI. They were held in Katcively, Crimea, in May 2003 and 2005 and attracted experts from more than 16 different countries. The 3rd LTWMP will be held in 2007.

One of the initiatives directed to the further development of integration processes is the concept proposed by LTRI on the development of the virtual enterprise to increase the efficiency of use of industrial laser systems. Such an e-enterprise may improve the competitiveness of different small and medium plants using unique and expensive industrial laser systems.

PROBLEMS

Permanent efforts are directed to the achievement of the highest quality and productivity of processing at the lowest possible cost.

This may be achieved by

- better understanding of laser beam interaction with processed material;
- full control of all parameters involved in the process;
- adequate process simulation and optimization of all working conditions;
- development of process monitoring devices and fully adaptive systems for processing;

- reducing the maintenance costs of laser industrial systems;
- using efficient devices, instrumentation, and methodology for express measurement of the processing results;
- improving the academic programs for the younger generation of specialists studying laser technology and other nontraditional processing;
- wider development of interdisciplinary studies, intensifying the international collaboration.

CONCLUSIONS

(1) Research, industrial, and academic activity in laser technology in Ukraine has the obvious trend to globalization.

(2) Ukraine has significant potential in laser technology for participation in integrated international R&D projects.

(3) The gained academic experience and industrial and scientific potential of the laser community of Ukraine may be used for a wider integration into the global economy.

The paper was presented at the laser technology summit meeting “GARELAM—Global Application, Research, and Education in Laser-Aided Manufacturing,” held in the American Academy of Sciences in Washington, DC, USA, in July 2006.

REFERENCES

1. Kovalenko, V.S., Opportunities to Use Laser Technology in Automotive and Aerospace Industry, *Electron Material Machining*, 2002, no. 36, pp. 9–18.
2. Kovalenko, V., Uno, Y., Okamoto, Y., *et al.*, Laser Cutting of Semiconductor Elements, *Int. J. Electrical Machining*, no. 7, 2000, pp. 9–14.
3. Kovalenko, V., Anyakin, M., and Karpachov, Y., Robotized Laser Technology—Solution for the Problem of Destroyed Reactor Dismantling at Chernobyl Atomic Station, *Proc. the 12th International Symposium for Electromachining (ISEM)*, Aachen, 1998, pp. 613–623.
4. Kovalenko, V.S., Golovko, L.F., Novikov, N.V., *et al.*, Laser Technology Application for Diamond Tool Manufacturing, *Proc. International Conference LTWMP-2003, PWI NASU*, Kiev, 2003, pp. 159–164.
5. Meijer, J., Gillner, A., Kovalenko, V., Hoffman, D., *et al.*, Laser Machining by Short and Ultra Short Pulses: State of the Art, *Proc. CERP General Assembly*, San Sebastian, 2002.
6. Kovalenko, V.S., Mamalis, A., and Kolpakov, V.V., WEB-Technologies Application to Increase the Efficiency of Laser Industrial Systems, *Proc. International Conference LTWMP-2005, PWI NASU*, Kiev, 2005, pp. 64–66.